Optelis - Optics, Electronics, Instrumentation and Systems

TP 13989E

Feasibility of a Modulating Grid Optical Pressure Sensor

Prepared for

Transportation Development Centre
Transport Canada

October 2002

1494 rue du Golf • Cap Rouge, Québec • Canada G1Y 3R2 • Tel (418) 652-8345 • Fax (418) 652-8345 • a.morin@ieee.org

TP 13989E

Feasibility of a Modulating Grid Optical Pressure Sensor

By

André Morin, Optelis
Ngan Lê, École de Technologie Supérieure

October 2002

This report reflects the views of the authors and not necessarily those of the Transportation Development Centre of Transport Canada or the sponsoring organization.

The Transportation Development Centre does not endorse products or manufacturers. Trade or manufacturers' names appear in this report only because they are essential to its objectives.

Project Team

André Morin, Principal Engineer
Ngan Lê, Lead Mechanical Engineer
Henri Champliaud, Finite Element Modeling
Jean-François Chätelain, Finite Element Modeling
Sang Hô, Finite Element Modeling

Un sommaire en français se trouve avant la table des matières.

Transport Canada / Transports Canada

PUBLICATION DATA FORM

1. Transport Canada Publication No.	2. Project No.	3. Recipient's Catalogue No.
TP 13989E	5014	

4. Title and Subtitle	5. Publication Date
Feasibility of a Modulating Grid Optical Pressure Sensor	October 2002
	6. Performing Organization Document No.: OTL-TDC0101-FR

7. Author(s)	8. Transport Canada File No.
André Morin	ZCD2450-C-266

9. Performing Organization Name and Address	10. PWGSC File No.
Optelis-Optics, Electronics, Instrumentation and Systems 1494 rue du Golf Cap Rouge, Quebec Canada G1Y 3R2	MTB-0-02031
	11. PWGSC or Transport Canada Contract No.: T8200-01-0546/001/MTB

12. Sponsoring Agency Name and Address	13. Type of Publication and Period Covered
Transportation Development Centre (TDC) 800 René Lévesque Blvd. West Suite 600 Montreal, Quebec H3B 1X9	Final
	14. Project Officer: C. Gautier

15. Supplementary Notes (Funding programs, titles of related publications, etc.)

Co-sponsored by Fisheries and Oceans Canada

16. Abstract

This study was initiated to evaluate the viability of a new pressure sensor concept originally developed by the Transportation Development Centre of Transport Canada. The sensor will be used as part of an embedded combustion efficiency diagnostic system within a vessel's engines. The environment in which the sensor is meant to operate poses significant technical challenges, most notably with respect to the high operating temperatures and sensor life. These design issues are further exacerbated by the required accuracy and linearity.

Following a design review, improvements were proposed to solve the design problems identified. The new design, attained after several iterations, improves on the differential approach originally proposed and eliminates the thermally, mechanically and aging-induced common-mode errors. It also uses gold-coated optical fibres for increased resistance to temperature. Although the revised design meets the objectives of size, accuracy, longevity and ruggedness, some design and manufacturing aspects that may hinder sensor performance and manufacturing yield are discussed, and suggestions are proposed to reduce their impact. It is further noted that the modulating grid design, while significantly improved, still stands as the most serious issue to be overcome. Manufacturing cost analysis also reveals that the targeted value is exceeded. A thorough mechanical design revision is therefore recommended.

17. Key Words	18. Distribution Statement
Optics, optical fibres, pressure sensor, differential, diesel engine, temperature, combustion, emissions, efficiency	Limited number of copies available from the Transportation Development Centre

19. Security Classification (of this publication)	20. Security Classification (of this page)	21. Declassification (date)	22. No. of Pages	23. Price
Unclassified	Unclassified	—	x, 58, apps	Shipping/ Handling

Transports Canada / Transport Canada

FORMULE DE DONNÉES POUR PUBLICATION

1. N° de la publication de Transports Canada	2. N° de l'étude	3. N° de catalogue du destinataire
TP 13989E	5014	

4. Titre et sous-titre	5. Date de la publication
Feasibility of a Modulating Grid Optical Pressure Sensor	Octobre 2002
	6. N° de document de l'organisme exécutant: OTL-TDC0101-FR

7. Auteur(s)	8. N° de dossier - Transports Canada
André Morin	ZCD2450-C-266

9. Nom et adresse de l'organisme exécutant	10. N° de dossier - TPSGC
Optelis-optique, électronique, instrumentation et systèmes 1494 rue du Golf Cap Rouge, Québec Canada G1Y 3R2	MTB-0-02031
	11. N° de contrat - TPSGC ou Transports Canada: T8200-01-0546/001/MTB

12. Nom et adresse de l'organisme parrain	13. Genre de publication et période visée
Centre de développement des transports (CDT) 800, boul. René-Lévesque Ouest Bureau 600 Montréal (Québec) H3B 1X9	Final
	14. Agent de projet: C. Gautier

15. Remarques additionnelles (programmes de financement, titres de publications connexes, etc.)

Coparrainée par Pêches et Océans Canada

16. Résumé

Cette étude a été entreprise afin d'évaluer la viabilité d'un nouveau concept de capteur de pression développé au départ par le Centre de développement des transports de Transports Canada. Le capteur est destiné à être intégré à un système de mesure en ligne de l'efficacité de combustion des moteurs diesel des navires. L'environnement propre à cette application pose des problèmes techniques significatifs, notamment en raison de la longévité requise du capteur et des hautes températures d'opération rencontrées. Ces contraintes sont exacerbées par la précision et la linéarité de mesure requises.

Suite à l'analyse du concept original, des modifications sont suggérées afin de corriger les lacunes identifiées. Le nouveau concept, atteint par itération, repose sur une approche différentielle et élimine les erreurs en mode commun induites par le vieillissement, thermiquement et mécaniquement. Il utilise en outre des fibres optiques plaquées or pour une résistance accrue aux hautes températures. Ainsi modifié, le concept rencontre les objectifs de dimensions, de précision, de longévité et de robustesse. Néanmoins, certains points demeurent susceptibles d'influencer les performances et le taux de rendement de fabrication, et des suggestions sont apportées de façon à en réduire leurs impacts. En dépit des améliorations apportées, la conception des grilles de modulation demeure néanmoins le problème le plus significatif. L'analyse des coûts de revient révèle en outre un coût trop élevé. À la lumière de ces commentaires, le rapport suggère une révision du concept mécanique du capteur.

17. Mots clés	18. Diffusion
Optique, fibres optiques, capteur de pression, différentiel, moteur diesel, température, combustion, émissions, efficacité	Le Centre de développement des transports dispose d'un nombre limité d'exemplaires.

19. Classification de sécurité (de cette publication)	20. Classification de sécurité (de cette page)	21. Déclassification (date)	22. Nombre de pages	23. Prix
Non classifiée	Non classifiée	—	x, 58, ann.	Port et manutention

EXECUTIVE SUMMARY

This study was initiated to evaluate the viability of a new pressure sensor concept. This sensor, originally developed by the Transportation Development Centre of Transport Canada, is meant to be used as part of an embedded combustion efficiency diagnostic sensor within a vessel's engines. A second objective of this project sought to propose alternatives to certain aspects of the design so as to mitigate some of the shortcomings identified. Based on the findings of the above objectives, a third objective was to propose design completion and manufacturing cost estimates.

The environment in which the sensor is meant to operate and the application for which it was designed both pose significant technical challenges, most notably with respect to the high operating temperatures (450 °C) and sensor life (five years). The design issues related to the operating constraints are further exacerbated by the required accuracy (0.1%) and linearity (0.1%).

The revised sensor concept is based on a differential approach, eliminating the thermally, mechanically and aging-induced common-mode errors. The revised design, attained after several iterations, uses gold-coated optical fibres for increased resistance to temperature. The modifications made to the original design meet the objectives of dimensions and absolute precision while maintaining the number of parts required at an acceptable level and keeping the assembly procedure simple.

The sensor's transient thermal behaviour and the predicted natural frequencies lead us to conclude that the current design should meet the precision and useful lifetime goals originally defined. However, recommendations are made for further increasing the natural resonance frequencies. Improvements seeking to reduce the thermally induced stress fatigue during the motor starting-up phase are also proposed. The analysis of the sensor design revealed some design and manufacturing issues that may affect both sensor performance and manufacturing yield, yet for most of them simple potential solutions and workarounds can be implemented. Suggestions on how to minimize risks associated with these two aspects are made.

The bill of material indicates that the targeted manufacturing cost objective is largely exceeded. This situation is most notable for machined parts. While several cost reduction alternatives are presented. the impact of these suggestions should first be validated through prototyping before implementation. Replacing the differential approach with a single channel scheme would result in a twofold cost reduction of optical and opto-electronics components. This would also drive the machined parts components down. However, this simplification would most likely be accompanied by significant performance degradation.

While the design of the modulating grids was substantially improved over the course of this project, this issue nonetheless stands as the most serious to be overcome to make this sensor a reality and the most susceptible of influencing the feasibility of this sensor. Moreover, the conclusions derived from this study remain theoretical. As such, the fundamental concepts on which the design is based should be verified experimentally in a preliminary validation phase before a large-scale design and production project is undertaken.

SOMMAIRE

Cette étude a été entreprise afin d'évaluer la viabilité d'un nouveau concept de capteur de pression. Ce capteur, développé au départ par le Centre de développement des transports de Transports Canada, est destiné à être inséré dans les moteurs diesel des navires afin d'évaluer leur efficacité de combustion. Un deuxième objectif du projet consistait à proposer des alternatives de façon à pallier certaines lacunes de conception identifiées, le cas échéant, et à suggérer des modifications susceptibles d'améliorer les performances et de simplifier la fabrication. À la lumière des résultats obtenus, une évaluation sommaire des coûts de revient et des coûts de développement devait également être présentée.

L'application à laquelle est destinée le capteur et l'environnement dans lequel celui-ci est appelé à être opéré imposent des contraintes de conception, notamment en regard des très hautes températures d'opération (450 ºC) et de la longévité requise (cinq ans). Les problèmes de conception liés à ces contraintes sont de surcroît exacerbés par le niveau de performance requis par l'application visée, soient une linéarité et une précision de 0,1 %.

Le concept de capteur revu et corrigé est basé sur une approche différentielle permettant d'éliminer les erreurs en mode commun induites par des perturbations thermiques et mécaniques extérieures au système, ainsi que par le vieillissement des composants. Le nouveau concpet, atteint après plusieurs itérations, utilise des fibres optiques plaquées or pour une résistance accrue à la température. Les modifications apportées au concept original permettent également de rencontrer les objectifs de dimensions et de précision absolue, tout en maintenant le nombre de pièces requises à un niveau acceptable et l'assemblage à des opérations simples.

L'analyse du régime thermique transitoire ainsi que l'analyse des fréquences naturelles du système permettent de conclure que le concept du capteur devrait être en mesure de rencontrer les objectifs de précision et de longévité recherchés. Certaines recommandations propres à améliorer la fréquence naturelle de résonance minimale ainsi que la résistance à la fatigue due aux contraintes thermiques lors du démarrage du moteur sont néanmoins formulées. Des suggestions sont apportées sur la façon de minimiser les risques associés à ces deux aspects.

Une analyse préliminaire des coûts révèle d'autre part que les objectifs de prix de revient sont largement excédés, notamment au chapitre des pièces usinées et plusieurs suggestions de nature à réduire les coûts sont présentées. L'impact de ces suggestions devrait d'abord être vérifié à l'aide de prototypes avant de procéder avec la mise en œuvre. En effet, le remplacement de l'approche différentielle par un concept mono-canal permettrait de réduire d'un facteur deux le coût associé aux composantes optiques et optoélectroniques et de simplifier substantiellement le coût de fabrication des pièces usinées. Il est toutefois à noter que cette modification s'accompagnerait vraisemblablement d'une réduction des performances.

Bien que de nombreuses améliorations aient été apportées au concept des grilles modulatrices au cours de ce projet, la fabrication de celles-ci demeure néanmoins l'inquiétude principale et l'élément le plus susceptible d'influencer la mise en production de ce capteur. En outre, les conclusions tirées de ce projet demeurent théoriques et la mise en place d'une phase expérimentale préliminaire, visant à valider les concepts fondamentaux, est suggérée.

TABLE OF CONTENTS

LIST OF FIGURES

LIST OF TABLES

ACRONYMS

ADC	Analog-to-Digital Converter
CCDR	Core-to-Clad Dimension Ratio
CDR	Critical Design Review
CTE	Coefficient of Thermal Expansion
DDR	Detailed Design Review
EFL	Effective Focal Length
FEA	Finite Element Analysis
FOS	Fibre-Optic Sensor
FOPS	Fibre-Optic Pressure Sensor
FS	Full Scale
H/W	Hardware
LSB	Least Significant Bit
N.A. or NA	Numerical Aperture
NEP	Noise Equivalent Power
P/N	Part Number
RE	Reynold's Number
RMS	Root Mean Square
RSS	Root Sum of Squares
S/H	Sample and Hold
SNR	Signal-to-Noise Ratio
S/W	Software
TDC	Transportation Development Centre
TIA	TransImpedance Amplifier
TIR	Total Internal Reflection
TRR	Test Readiness Review

DEFINITIONS

Insertion loss: Optical power losses introduced by an optical component.

Light conduit: A general term referring to an optical fibre, a fibre optic bundle or a light pipe.

Light path: Path followed by a beam of light within an optical system.

UNITS, SYMBOLS AND CONVENTIONS

[a.u.]	Arbitrary Units
dBm	Optical power units; defined as 10 log(P/1000 [μW])
Φ	Radiant Power or Flux in Watts

1 INTRODUCTION

1.1 Scope of Document

This document constitutes the final report detailing the findings of the project entitled *Feasibility study of a modulating grid optical pressure sensor concept.* This study was initiated to evaluate the viability of a sensor concept originally developed by the Transportation Development Centre of Transport Canada. This report is based on and addresses the issues described in the reference documents RD1 and RD2.

1.2 Background Information

It is a fairly well recognized fact that pressure sensing is a mature field. Yet, there are some uncharted areas where most commonly available sensors fall short of the requirements. Continuous measurement of diesel engine combustion pressures constitutes such an example.

The advantages of monitoring the combustion efficiency – namely, fuel economy, environmental benefits and reduced needs for maintenance – all militate in favour of continuous inline pressure monitoring of diesel engines. For the better part though, most of the potential installations would be retrofitted to existing engines. This requirement poses specific challenges that preclude the use of many of the existing technologies. To quote *Industrial Technology* magazine "Permanent on-line monitoring of the cylinder pressure of motors has always been a tricky one. Commonly used systems such as quartz pressure sensors are able to measure the dynamic cylinder pressure with small thermodynamic errors, but these systems are not suited for the high load cycling which accumulates through permanent on-line measurement."[1]

For example, water-cooled pressure sensors cannot be used because of the complexity of retrofitting cooling pipes in a safe, unobtrusive, and easily maintained configuration, both during use and during engine maintenance. Modifying cylinder heads to accommodate special pressure sensors is not acceptable either since tampering with initial engine head design would cause a wealth of problems of its own.

Other techniques such as strain gauges fitting to the cylinder head bolts have been envisaged, but these methods have been found to be too complex to maintain, to be inaccurate over time, and to suffer from bandwidth limitations inherent in cylinder head/holding bolt mechanical systems. Other types of sensors, such as interferometric optical strain gauges, have been investigated but their cost is prohibitive and they suffer from the same temperature limitations as the other methods. Thus, while there is a need for monitoring the cylinder pressure of diesel engines, there exists no readily available solution.

For the better part, cylinder pressure sensors can only be retrofitted on diesel engines through a *T* connection adapter inserted in line with the cylinder indicator valve. The tube leading to the retrofitted pressure sensor can reach several centimetres in length and has an internal diameter of 6 to 8 mm. Under typical operating conditions, the peak pressure can reach 20 MPa at a mean combustion cycle temperature of 450°C. Under anomalous conditions however, such as detonation or overload, cylinder pressures and temperatures can reach even higher values and provision must be made when a sensor is selected to deal with such issues. Finally, the dynamic response of the sensor is also important, as the dynamic behaviour of the cylinder pressure is an integral part of the combustion efficiency and engine health diagnostic process. Thus, the sensors are also required to provide good frequency response. An

[1] http://www.industrialtechnology.co.uk/2000/mar/control.html

appropriate diesel engine pressure sensor must therefore successfully address the retrofit, range, temperature, longevity, reliability, frequency response and size constraints issues described above.

1.3 Project Objective

The first objective of this project was to evaluate a new concept of low cost, high accuracy optical pressure sensor as originally developed by the customer. The other objectives were to develop viable alternatives for the portions of the design where critical design issues have been identified, to provide estimates of manufacturing cost for the selected concept and to provide a preliminary design development schedule.

1.4 Performance Requirements

The basic requirements concern cyclic endurance, resistance to high temperatures (450°C), accuracy, robustness, ease of maintenance and size.

In order to be attractive to plant operators, the pressure sensor should operate continuously without failure or accuracy degradation for extended periods. Consider for example the cost of instrumenting four 16-cylinder engines for a sensor lasting about six months and with a tag price of $1000. In materials alone, that would amount to more than $ 32 000 a year without taking into account inventory and installation costs. Consequently, a life expectancy of five years for a total of one billion cycles/year is targeted.

The sensor must also resist the high operating temperatures without failure or accuracy degradation caused by metal creep, fracture or loss of heat treatment characteristics. The sensor must therefore operate at high temperature despite the potential for accelerated component corrosion inside the device.

A linearity of 0.1% and an accuracy within 0.1% of original calibration are targeted throughout the device life cycle. However, the sensor need not provide absolute pressure values and can be of a *dynamic* type, responding accurately to pressure changes only. In order to transmit accurately the low frequency signals of interest, the time constant should exceed 30 seconds. Finally, the sensor must have a bandwidth of 20 kHz or better.

Robustness is paramount. Despite the sensor's ability to resist operating conditions, the housing and internal components may not be able to sustain external shocks, accidental blows or cable pulls, and aggressive chemicals pressure jets routinely used to clean and degrease the engine. Regular maintenance requires components and cylinder heads to be removed and maintained. The sensor should be designed to accommodate its removal and reinstallation. Features such as quick disconnection are required. The sensor size must be limited to allow retrofitting most engine configurations. A maximum length of 80 mm and a maximum diameter of 24 mm are targeted. The sensor must also be small so that retrofit to most motor models and makes is achievable. Finally, the sensor must accommodate drive electronics located 2 to 3 m away.

1.5 Project Organization

The project was divided into two parts. Université du Québec's *École de technologie supérieure* in Montreal was responsible for both the thermal and mechanical finite element analysis while Optelis was re-

sponsible for the optical and signal processing aspects of the project. The integration into a final document fell under the responsibility of Optelis.

1.6 Design Constraints

The performance and reliability of a design must be evaluated against the environmental factors and constraints (size, etc.) dictated by the operating environment. In addition to the operating environment, there are also operating constraints as well as ancillary constraints that correspond to those factors influencing the design such as cost, manufacturability, etc.

1.6.1 Environmental Constraints

The environment criteria include:

- The operating temperature range, which limits the choice of building materials;
- The rate of temperature change (thermal shock);
- The pressure range;
- The pressure cycle life;
- The vibration spectrum (amplitude and frequency);
- The surroundings in which the sensor is expected to operate and the potential contaminants (e.g., chemicals, gases, and oils);
- The environmental contaminants (e.g., salt water, dirt, and dust);
- The electromagnetic environment;
- The safety requirements (explosive gases, etc.);
- The physical environment in which the sensor must be installed.

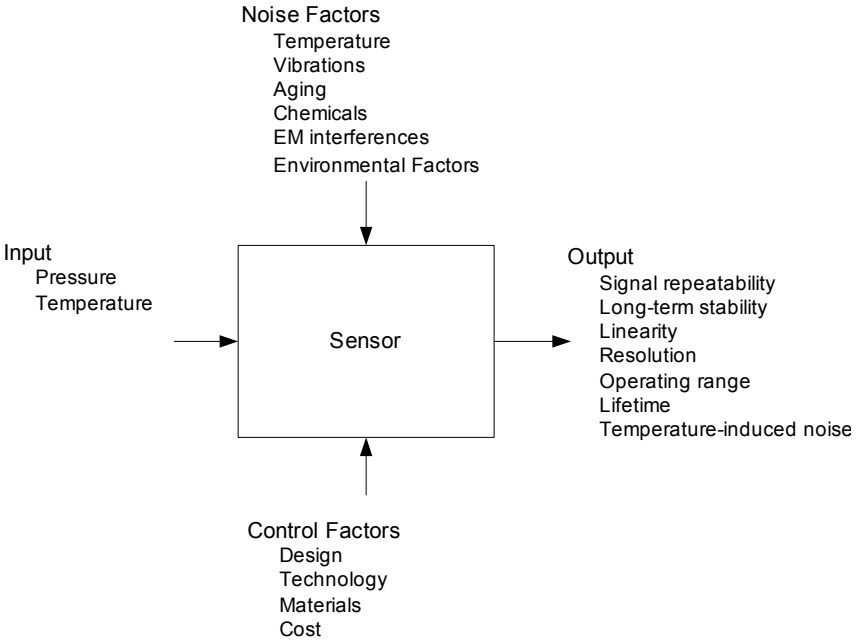

Figure 1: P-Diagram for Sensor Design

1.6.2 Operational Constraints

The operating constraints include:

- The signal requirements (distance of transmission, required signal strength, frequency, etc.);
- The packaging requirements, including size, weight, and resistance to corrosion, explosion, liquids, and fire;
- The electrical interface requirements;
- The mechanical interface requirements, such as mounting connections;
- The required accuracy needed (under all conditions);
- The targeted lifetime.

1.6.3 Miscellaneous Constraints

Miscellaneous constraints are those not listed elsewhere that may affect the design. These criteria include:

- Sensor manufacturing cost;
- Existing patent rights;
- Safety considerations related to material selection (for example, beryllium exhibits excellent thermal properties yet poses serious manufacturing problems owing to its toxicity in powder form).

The above constraints are summarized in the *P*-diagram shown in Figure 1.

2 MODULATING GRID SENSOR ANALYSIS

The first part of this chapter summarizes the most common pressure sensing means. The second part focuses on the original sensor concept submitted to the authors for analysis. Based on this analysis, a variant on the original sensing scheme is presented and analyzed in the last sections of this chapter.

2.1 Pressure Sensing

At the heart of almost every pressure sensor lies a *force-gathering* device used to convert the pressure into either a strain or a displacement. This strain or displacement is eventually read out and converted into a pressure reading. In the automotive/high-pressure/high-temperature industry segment, pressure sensor designs based on membrane deflection are the norm although other, more complex means of force-gathering, are sometimes used.[2]

A simple membrane-based pressure sensor consists of a membrane that flexes in response to a change in pressure, coupled to a method of measuring the deflection. The outer surface of the membrane is exposed to the pressure being measured while the inner surface is held at a constant pressure (say atmospheric). The amount of deflection of the membrane is then a measure of the difference of pressures acting on the two surfaces. Thus, the diaphragm operates as a differential pressure monitor and senses pressure variations rather than absolute pressures. The maximum, reliable pressure that can be measured is determined by the mechanical strength of the deflecting membrane, the amount of travel available, and the known response of the membrane material to stress. The membrane thickness usually increases as the pressure regime to be measured increases. The fabrication of the membrane and the deflection measurement methods are the primary differences between sensor designs.

The conversion of the diaphragm flexing motion into a pressure can be achieved in a variety of ways. The most commonly used ones are based on the piezoresistive effects, on a capacitance effect or on the modulation of the phase or intensity (or both) of a beam of light. Piezoresistivity is the change in resistance of a material under mechanical stress. In silicon, the piezoelectric effect is dependent upon the doping concentration and crystal orientation. Piezoresistive sensors typically use four small strain gauges coupled to form a Wheatstone bridge on a diaphragm. The strain gauges are either bonded on a diaphragm or built on it. Many successful pressure sensor designs are based on this architecture and some do approach the level of performance required by the application.[3,4]

However, to date, there appears to exist no design based on this approach able to survive the targeted sensor environment, as no bonding agents can endure the number of cycles or the high temperatures and temperature variations typical of diesel engine operation. Moreover, most strain gauges are not capable of reliable, sustained operation at temperatures of up to 450°C (850°F).

When a sensor is built so that the diaphragm constitutes one plate of a parallel plate capacitor, a change in the distance to the opposite plate changes the capacitance. This change can be measured with a resonant LC circuit. The sensitivity of this type of sensor is generally good but the pressure range is quite small. Moreover, direct capacitive measurement is difficult because it requires precise alignment of the capacitor parts, which may drift with temperature variations. The associated electronics are generally complex and the required electrical insulation within the sensor calls for insulating materials, bonding

[2] Peter Van Vessem , *Rediscovering the Strain Gauge Pressure Sensor*. Eaton Corp. Aerospace Controls Div.
[3] http://www.optrand.com/MFPT99paper.htm
[4] http://www.industrialtechnology.co.uk/2000/mar/control.html

agents, etc., which further complicate the design. A similar analysis can be made of magnetic detection principles, which are even more subject to temperature variations and fabrication complexities.

2.1.1 Optical Methods

Most optical methods use the reflection of light off the diaphragm membrane surface to derive the position. These techniques can further be divided into interferometric methods and intensity-based methods. The former technique is generally preferable as most intensity-based sensors suffer from signal stability problems. However, in light of the high number of sensors per engine, the cost generally associated with interferometric sensor signal conditioning equipment was deemed too high in the context. Further, the customer felt that a distributed sensor approach coupled to a central processing unit common to all sensors was not practical in the context as a result of the maze of cables that would need to be run in the engine room.

Before this project was initiated, a careful review of commercially available optical sensors was conducted by the customer. A few potentially promising candidates were identified and field-tested. It turned out that most of the interesting sensors were based on optical technology, yet none of those tested proved to be fit for the application despite numerous attempts by the sensors' manufacturers and the customer to improve on the existing design. The failures were sometimes due to a darkening of the reflecting membrane surface. At other times, the high operating temperature simply loosened the bonding agents or induced crack and fatigue into the sensor's inner components.

By the time this series of tests was completed, the experiment had yielded enough knowledge to demonstrate that the optical sensing method offered a strong potential. Owing to its simplicity, this method was considered the most promising approach.

2.2 Original Sensor Principle

2.2.1 Concept

The concept described below was initially developed by TDC following a survey and subsequent testing of optical pressure sensors.

In the most promising sensor investigated, light emitted by an optical fibre is shone on the inner, polished surface of a flexible diaphragm. A second fibre, located beside the first one, collects part of the light reflected off the membrane. Since the distances between the two fibres and between the fibres and the membrane surface are small, the area on the diaphragm subtended by the numerical aperture of both fibres is different. As a result the collecting fibre receives only a portion of the light emitted by the first fibre, which is reflected off the diaphragm. The received fraction is proportional to the spacing between the fibres' tips and the diaphragm.

Albeit elegant and rather simple, this solution was found to be plagued by a number of problems. For example, these sensors did operate well at first, but their performance would start to degrade after some time. This problem was traced back to a darkening of the diaphragm's inner surface.

Based on this experience, it was proposed to adopt a transmission-based intensity modulation scheme that had not been exploited in any of the sensors reviewed. The original concept is schematized

in Figure 3. It was estimated that this approach would somewhat relax the fibres positioning requirements and solve the darkening of the diaphragm surface.

The modulating action can be achieved in a number of ways. For one, the modulator could consist of a simple beam stop (or interrupter), positioned in front of the source, that would block an increasing large or small portion of the light beam. Alternately, the modulator could be implemented as a variable attenuator, whose transmissivity changes along the direction of motion of the attenuator. Lastly, the modulator could consist of a hybrid variant of the former two, offering the uniformity provided by the variable modulator while maintaining the construction and reliability offered by the razor-edge beam interrupter.

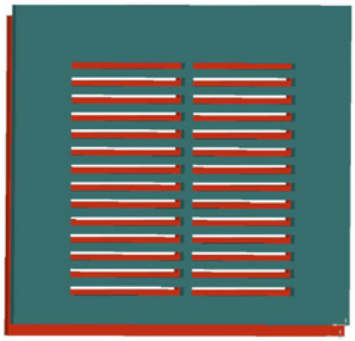

Figure 2: Fixed and Modulating Grids

The proposed technique relies on a pair of thin slotted grids, one of which is fixed to the sensor body while the second is mechanically linked to the diaphragm and is free to move with the diaphragm. The condition of maximum transmissivity is met when the two grids are aligned. When one of the grids is displaced with respect to the other by the width of a slit, light shining through a slit of the primary grid is partly blocked by the other grid, resulting in a diminution of light throughput. In theory, if the slits of the grids are machined so that they match the full travel of the diaphragm at maximum pressure, a 0 to 100% modulation of light is possible.

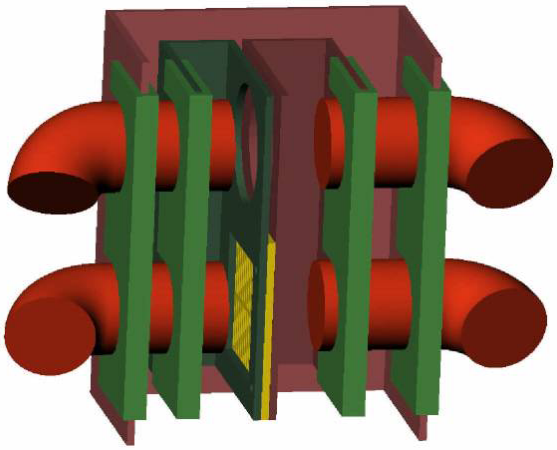

Figure 3: Original Sensor Concept

In the proposed implementation, light is brought up to and from the modulating grids by optical fibres. Moreover, in order to mitigate the effects of light intensity variations in the light path prior to modulation, a second set of optical fibres is used in parallel with the first. The light beam in this second pair of emitter/receiver fibres is not subjected to modulation by the grid and is solely used to compensate for optical losses in the optical path and optical source intensity variations.

Given the pressure levels envisaged, the physical limitation on sensor size, the available materials and their fatigue life, it was found that deflections on the order of 20 to 50 μm could reasonably be expected. This was considered small, and a mechanical movement amplification mechanism was devised. The proposed method made use of a cantilevered beam clamped on one end to the sensor wall. The free end was terminated with the modulating or moving grid described above while the middle of the cantilevered beam was actually resting against a pinion welded to the diaphragm. In this arrangement, the pinion transmitted the diaphragm movement to the cantilevered beam and the moving grid movement was amplified by a factor equal to the grid-to-fixed end/grid-to-pinion distances ratio.

The beam concept is illustrated in Figure 4. The diaphragm pinion is shown in light gray in the background whereas the cantilevered beam is illustrated in dark gray.

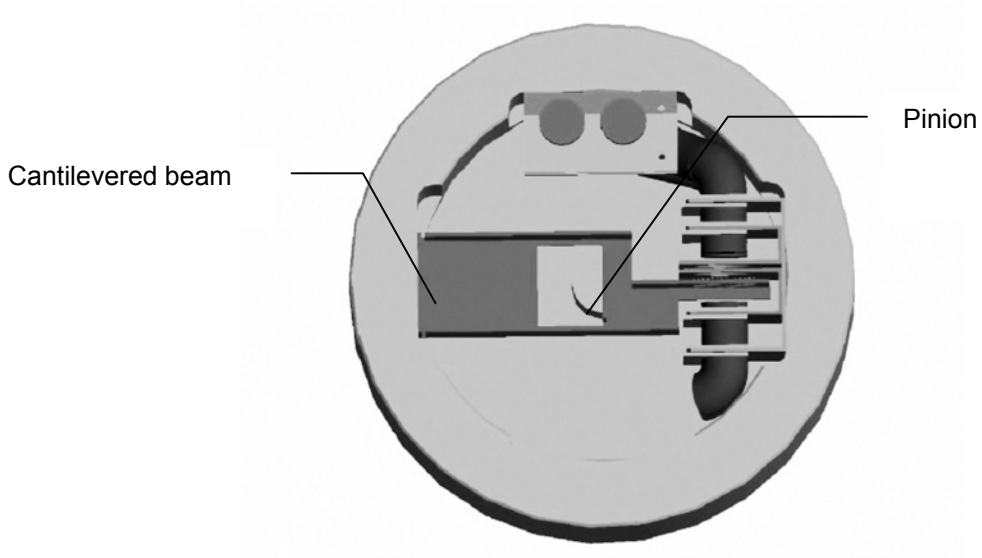

Figure 4: Cantilevered Beam and Diaphragm Pinion

2.2.2 Analysis

The design was analyzed with a focus on manufacturability and performance issues. The mechanical design was found complex in terms of component fabrication, sensor assembly and cost. The cantilevered beam design originally imagined as a folded metal sheet was deemed too difficult to manufacture with tolerances compatible with the precision required by the application. Finite element analysis performed on this component also revealed that there were many resonant modes lower than the minimum 20 kHz frequency.

The tight bends of the optical fibres were also found to be an important limiting factor of the design as the manufacturers' quoted fibres' minimum bend radii exceeded the allowable space. The required heat-

tolerant protective coating further exacerbated this fact. Accommodating the two fibres' bends required that the fibres exit the sensor perpendicular to its main axis. Unfortunately, this solution leads to an unacceptable sensor footprint.

The method envisaged to attach and maintain the optical fibres in place was also scrutinized and found ineffective in view of the long lifetime required. However, the compensation scheme for optical losses, optical source instabilities and drift was deemed useful yet perfectible as second order effects could not be totally eliminated. Lastly, from a global manufacturability point of view, the design is complex, and the assembly would necessitate many steps and very accurate welding in tight spaces.

2.3 Revised Sensor Design

This section builds upon the findings of the analysis of the original sensor concept and presents a number of suggestions to increase the viability of this approach.

The revised sensor design is shown schematically in Figure 5.

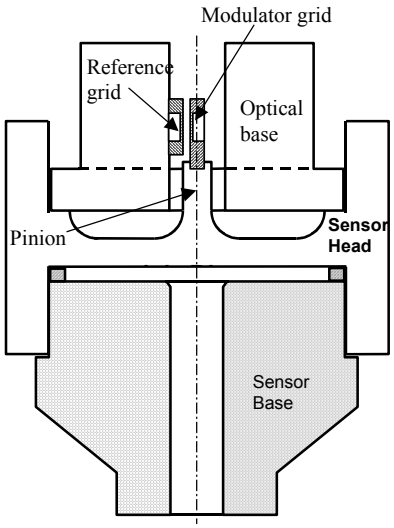

Figure 5: Sensor Schematic Diagram

The revised design is still based on a pair of slotted grids, the fixed grid being called the *reference* grid while the moving grid is referred to as the *modulating* grid. The new design diverges from the original concept by its use of the two pairs of optical fibres. In the original design, one pair of fibres was used to emit and receive a beam of light, which was modulated by the two slotted grids, while the second pair was solely used to establish a sensor optical output reference.

In the revised concept, both pairs of fibres are used for measuring purposes and both pairs are also used for referencing purposes. This dual use of the optical channels maximizes the output swing of the sensor for a given pressure and ensures that intensity variations and optical losses are fully accounted for. The whole concept relies on the use of two complementary (in the mathematical sense) signal channels: when the pressure applied to the diaphragm is such that the intensity transmitted by one channel is

minimum, the transmissivity of the second channel is maximum. In theory, this can be realized by making the modulating grid in two segments, one of which is the mathematical complement of the other. This geometry is illustrated in Figure 6.

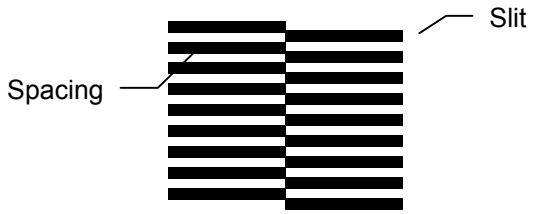

Figure 6: Complementary Grids

Thus, subtracting the intensity values from the two channels actually doubles the sensor's response to a given pressure. On the other hand, adding the signal from both sensors yields a 100% transmissivity baseline that can be used to correct for optical losses and optical source intensity variations. Defining channels A and B and their respective transmissivities T_A and T_B, we find that the pressure P is given by

$$P = m \cdot (T_A - T_B) \tag{2.1}$$

where m is a constant. Noting that

$$T_B = 1 - T_A \tag{2.2}$$

and combining equations (2.1) and (2.2), we obtain

$$\begin{aligned} P &= m \cdot (T_A - (1 - T_A)) = m \cdot (2T_A - 1) \\ I &= T_A + T_B = 1 \end{aligned} \tag{2.3}$$

where I stands for the total nominal transmissivity. Since T_A can take values from 0 to 1, P can take values ranging from m to $-m$. Comparison with equation (2.1), indicates that the differential approach effectively doubles the amplitude of the output swing in response to a given applied pressure.

The differential approach not only provides a larger output swing in response to a stimulus but also has other advantages. For one, equation (2.3) indicates that the summation of the intensities of the two channels is a constant value that is independent of the applied pressure. This summation yields a reference value that can be used to compensate for optical source intensity variations.

Thus the equation

$$P = m \cdot \frac{(T_A - T_B)}{(T_A + T_B)} \tag{2.4}$$

yields a pressure value which, to a first-order approximation, is independent of the intensity of the optical source. However, errors are perfectly compensated solely for source intensity perturbations, which are

common to both channels (i.e., perturbations induced in only one channel cannot be compensated). However, careful sensor design can minimize these effects.

Inspection of equation (2.4) also yields another interesting result. In general, it is desirable to maintain good signal strength in order to preserve system noise immunity since noise becomes increasingly preponderant as the signal strength decreases. With amplitude-based sensors, this is generally difficult to achieve. The situation is different with a differential design since, when one channel intensity is low, the intensity of the second must be high as a result of their complementary nature. The situation is equally good in the middle of the range when the two signals are equal and themselves in the middle of their range; although the result of the subtraction is a low intensity signal, the noise immunity remains good as two equally strong signals are being subtracted.

We have also seen previously that the differential approach effectively doubles the output signal modulation. This is equivalent to saying that half of the stimuli is required to produce a given output variation. This fact is important when we consider the physical movement the diaphragm can generate. Thus, the differential approach can be used to play the same role as the mechanical amplification of the cantilevered beam approach design originally proposed.

2.3.1 Modulation, Gratings and Diffraction

The modulating grid approach described above is conceptually simple to understand. As the reference and modulating grids slide by each other, the apparent width of the resulting composite slits they create varies. In turn, this varying width results in a linear modulation of the light intensity transmitted.

This intuitive concept is, in practice, almost perfectly valid when large slit dimensions are considered. When the slit size becomes small relative to the wavelength of light, diffraction effects can no longer be considered negligible, second-order errors. When a series of slits, whose heights are in the order of the wavelength of light illuminating them, are used, two effects take place. For one, the diffraction tends to disperse the beam. Collectively, the slits also act as diffraction grating. This results in a pattern light, which can no longer be viewed as a dimmed version of the incoming beam but rather produces a series of alternating light and dark fringes. Since the intensity, position and spacing between these fringes are highly dependent upon the slits spacing and height, diffraction must be carefully analyzed.

One must differentiate two diffraction regimes with correspondingly different mathematical treatments. The first mode is known as the *far-field* or *Fraunhofer* diffraction and is characterized by a well-understood set of equations. The second regime is the *Fresnel* diffraction. The two regimes are differentiated by the grid-to-observation plane distance and by the types of beams they consider. The former regime assumes that the beam is well collimated and that the observation to grating distance *z* is such that

$$z_1 \geq d^2 / \lambda , \tag{2.5}$$

where z_1 stands for the observation distance, d for the distance between slits and λ for the wavelength of light. When the condition described by equation (2.5) is met and if the beam is collimated, the Fraunhofer diffraction model is valid. Otherwise, Fresnel diffraction model must be used.[5] Figure 7 illustrates the two diffraction regimes.

[5] See RD3, pp.122ff for an excellent discussion of far-field and Fresnel diffraction discussion.

Unfortunately, given the size of the sensor and the wavelength used (visible or near infrared wavelengths), the above condition is not met and Fresnel diffraction must be used. The mathematical treatment of this model is complex and dedicated software is required to model the behaviour of the beam.

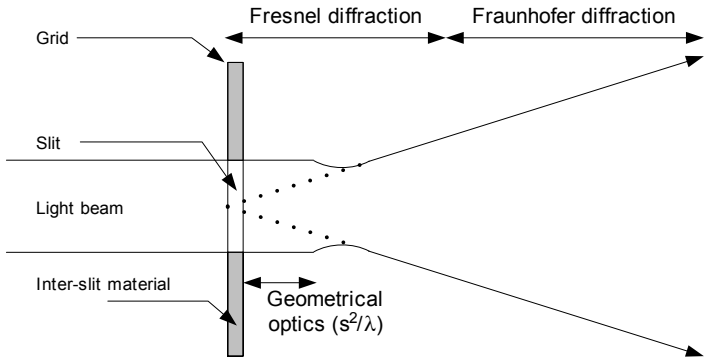

Figure 7: Fresnel and Fraunhofer Diffraction (not to scale)

Towards this end, we used *LightPipes*, an add-on to the popular Matlab™ software package. The system was modeled as two grids of negligible thickness spaced apart by a distance D_{IG}. The input beam was considered collimated and the reception optics were modeled with a circular aperture. The distance between the grids D_{IG}, the distance between the second grid and the reception optics z_1, and the wavelength λ were all varied independently. Reflections at the optical surfaces were neglected.

The LightPipes software models the Fresnel diffraction by representing a beam of light with an array of 'pixels'. Each pixel of the grid represents the wavefront of the light beam at a given spatial position. The pattern is then propagated along the beam axis in small steps. A complete optical system can be modeled in this fashion. A typical example of the code used in provided in Appendix A.

A series of well over 100 simulations was run to determine the effects of broadband wavelength illumination, varying inter-grating distance, collimating optics size and distance from the second grid to the collecting optics. The effects of limited pixel grid resolution were also analyzed. A resolution of 1280 x 1280 pixels was selected as a good compromise between available computational power and time and the systematic errors introduced by a coarser grid. The overall system field of view was set to 2 mm (1,5625 μm pixel element size) and the actual beam was limited to 1.5 mm with 100 μm high slits. A 200-μm centre-to-centre slit spacing was used (the selection of this particular value is discussed later on). The height of the slits results from a trade-off between the number of slits seen by the beam size and the desire to make the slit dimension large with respect to wavelength to reduce the effects of diffraction.

Figure 8 illustrates the evolution of the average error as a function of the inter-grid (D_{IG}) and grid to detection plane (z_1) distances. The average error is defined as the departure of a specific data point from a best-fit regression of the results. The data used to perform the regression was obtained in the following way. For given D_{IG} and z_1 distances, the second grid in the path was moved relatively to the first, fixed grid (in practice, the order of fixed and moving grid is irrelevant but this specific configuration lowers the computational burden). For all slit displacements, the ratio of the total energy available at the exit of the first grid to the energy encircled by the detector was computed. The process was repeated for all slit displacements until the 0% to 100% light modulation span was covered. This provided data for channel A. Channel B data was derived by taking the complement of channel A (e.g., value for 10% modulation in channel B is equivalent to data for 90% modulation in channel A).

The data from these two channels was then processed as described in equation (2.4), with *k* arbitrarily set to 1. This yielded a data set from which a linear regression was computed. The linear regression was computed from the data in the range of obscuration (modulation) ranging from 30 to 70% since it was observed that this range was most representative of the 'true' slope. The residual error, selected as the performance metric, was computed as the difference between the computed and regression values. An example of such a computation is presented in Figure 9. As one could expect, the differential error and differential signals both exhibit anti-symmetry about the 50% modulation ratio. The differential signal also has a signal output rate that is double the slope of the single channel output.

Figure 9 also shows that towards low modulation ratios, the computed values significantly depart from the ideal linear curve. This can be understood by realizing that the two grids actually behave as one. When the slits of the two girds are in phase, both grids behave as a single grid with large slits, a situation that is less prone to exhibit the diffraction effects, while small slits (gratings out of phase) tend to increase the diffraction effect. In other words, when the modulation ratio becomes small, the slits are proportionally smaller and diffraction becomes more significant.

The same phenomenon is also observed when the modulation ratio is high. In this case, the behaviour finds its explanation in the presence of two grids rather than one. First, it must be noted that the energy diffracted does not travel in a straight line; rather it is deviated form its original path (see Figure 10). Since the two grids are relatively far apart (D_{IG} = 200 μm), the energy not masked by the first grid is masked by the second even though the two grids are out of phase (slit of first grid corresponding spacing of second grid). When the two gratings are close to one another, one would expect this effect to vanish and this is what happens (D_{IG} = 1 μm in Figure 9). The remaining error in this case is due to the type of modeling used.

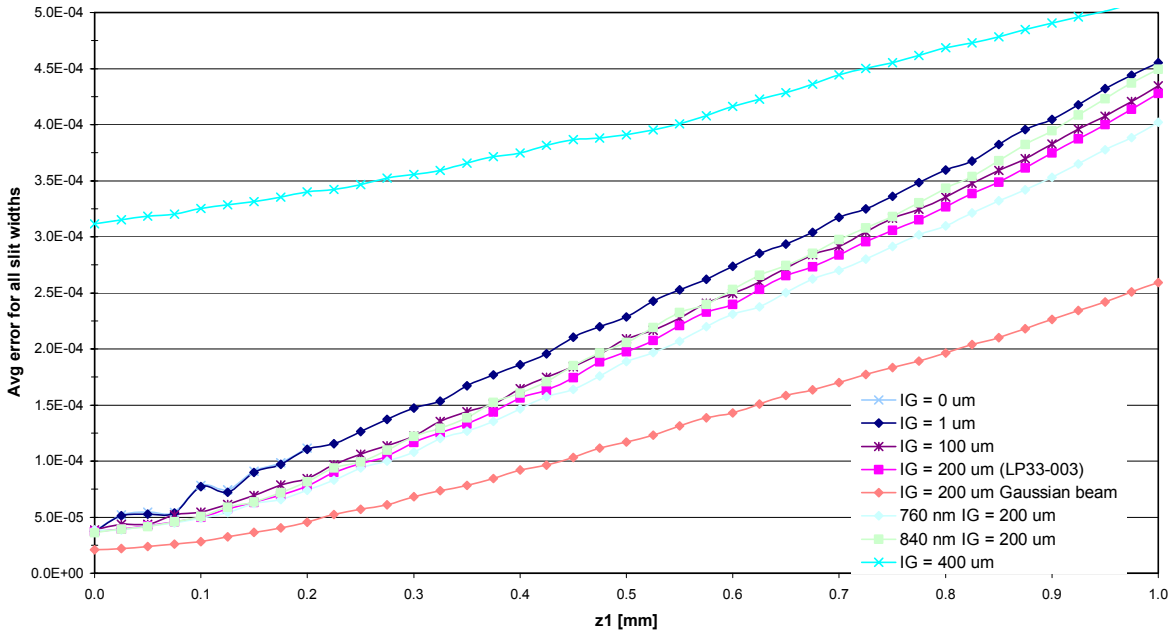

Figure 8: System Response for Short Inter-grating Distance

The above discussion assumes that the detector can collect rays impinging on the detector with a divergent angle. As we shall see later, these diverging rays will not all be collected at the detector, a situation that tends to render the system response more linear. On the other hand, the incoming (input beam) incident on the two grids will not be perfectly collimated either.

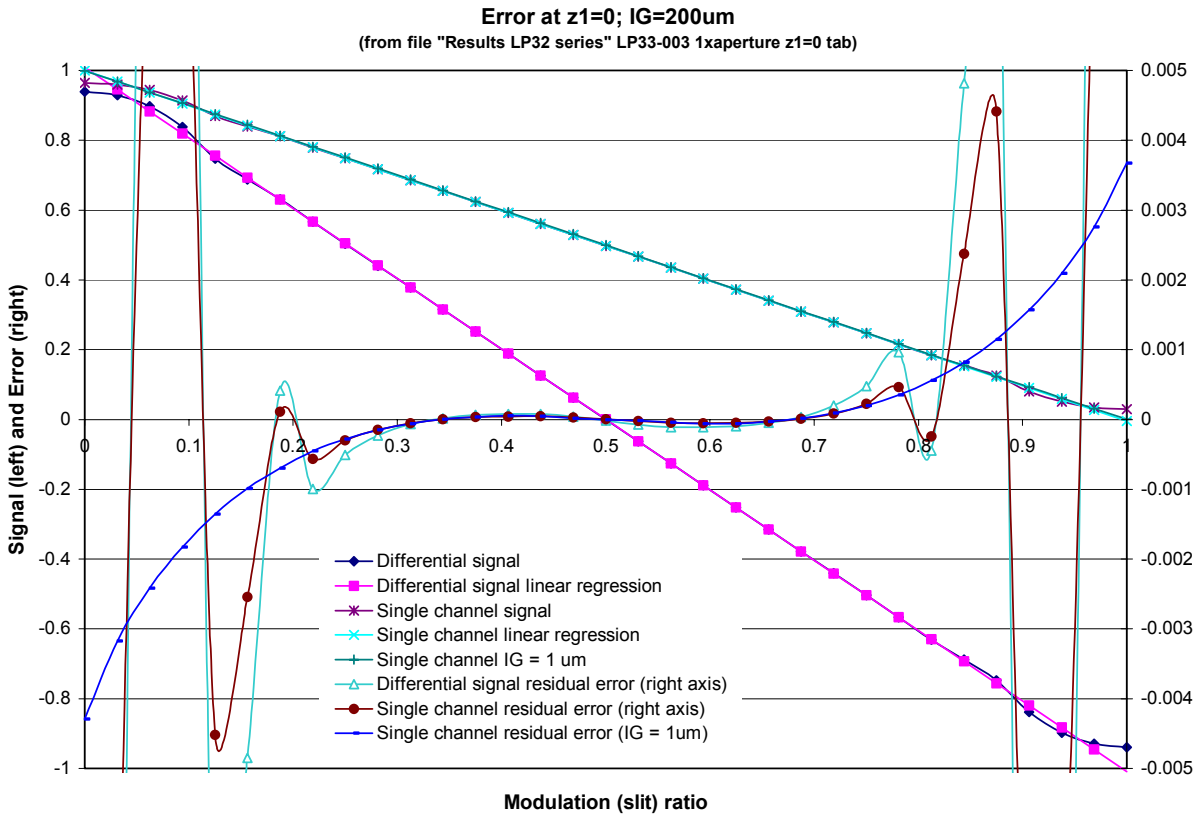

Figure 9: Response and Residual Error for Single and Double Channel Configurations

Figure 11 presents similar data in a different format. In this figure, illustrating the system error for a two channel signal, the inter-grating distance D_{IG} is set to 200 μm. The horizontal axis represents the distance between the moving grid and the detection plane whereas the vertical axis represents the average and maximum errors over the whole slit ratio range.

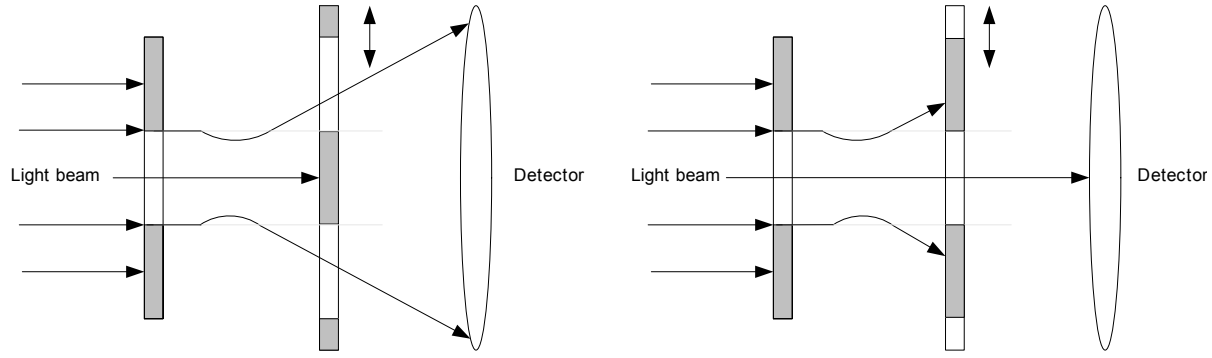

Figure 10: Effects of Diffraction on Transmissivity at Modulation Range Limits

Clearly, the error increases with z_1, a situation resulting from the energy dispersion generated by the grating (energy lost outside of detector area). Whereas the average error varies monotonically, the maximum error exhibit features attributable to the diffraction effect.

Figure 8 and Figure 12 summarize results similar to those obtained in Figure 11 for D_{IG} values ranging from 0 to 400 μm and 400 μm to 1 mm, respectively. All curves display the average error as defined above. In addition, Figure 8 displays the system response when wavelengths of 760 and 840 nm are injected into the system rather than the typical 800 nm wavelength assumed until now. As could be expected, the system's response at 760, 800 and 840 nm is similar. However, the error increases with wavelength since longer wavelengths are more susceptible to diffraction. Comparison of Figure 8 and Figure 12 (notice the vertical scale change) clearly show that the shorter inter-grating distances are preferable. Lastly, the values at $z_1 = 0$ put a lower limit to the software computational precision as a D_{IG} value of 0 μm and a z_1 value of 0 μm should, in theory, produce an infinitesimally small error (perfect case).

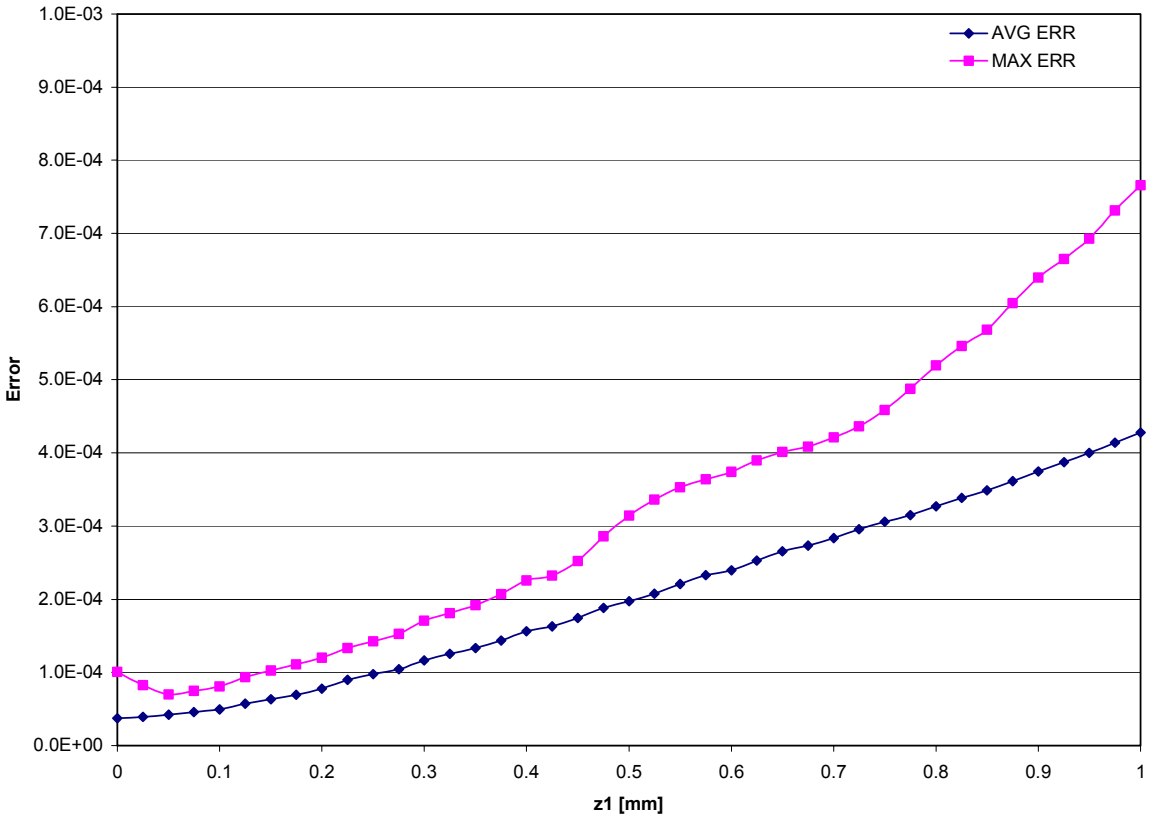

Figure 11: System Average and Maximum Errors

The system answer when the inter-grating distance is set to negligible values (0 and 1 μm respectively) is interesting. As it turns out, these two cases are almost perfectly identifiable to the system answer to only one grating of varying slit height. This fact is most noticeable by the small bumps between z_1 = 0.12 mm and z_1 = 0.175 mm. These bumps are predicted by theory and correspond to the transition zone between Fraunhofer and Fresnel diffraction regimes. Calculation shows that equation (2.5) predicts a transition region around 160 μm for a wavelength of 800 nm and a slit spacing of 100 μm. As the inter-grating distances increase, the two-grating system can no longer be assimilated to a simple grating and the effect is dwarfed by other factors.

Figure 8 also shows that the average error generally increases with distance z_1. It also shows that the error goes through a local minimum between 100 and 400 μm. Further calculations that this optimal operation point is located around D_{IG} = 200 μm but this should be interpreted with caution given the slight differences below 200 μm.

Lastly, Figure 8 shows the system response to an optical input beam with Gaussian intensity distribution rather than the flat top (uniform) distribution envisaged so far. Interestingly, this distribution generates a lower average error. Among the many explanations, we note that a Gaussian beam has stronger centre intensity and a lower intensity on the edges. Since the diffraction tends to make the energy 'flow' out of the detector area, the Gaussian beam behaves better as most of the energy remains concentrated in the centre region. This fact is most interesting, as optical fibres generally tend to have a Gaussian output beam intensity profile.

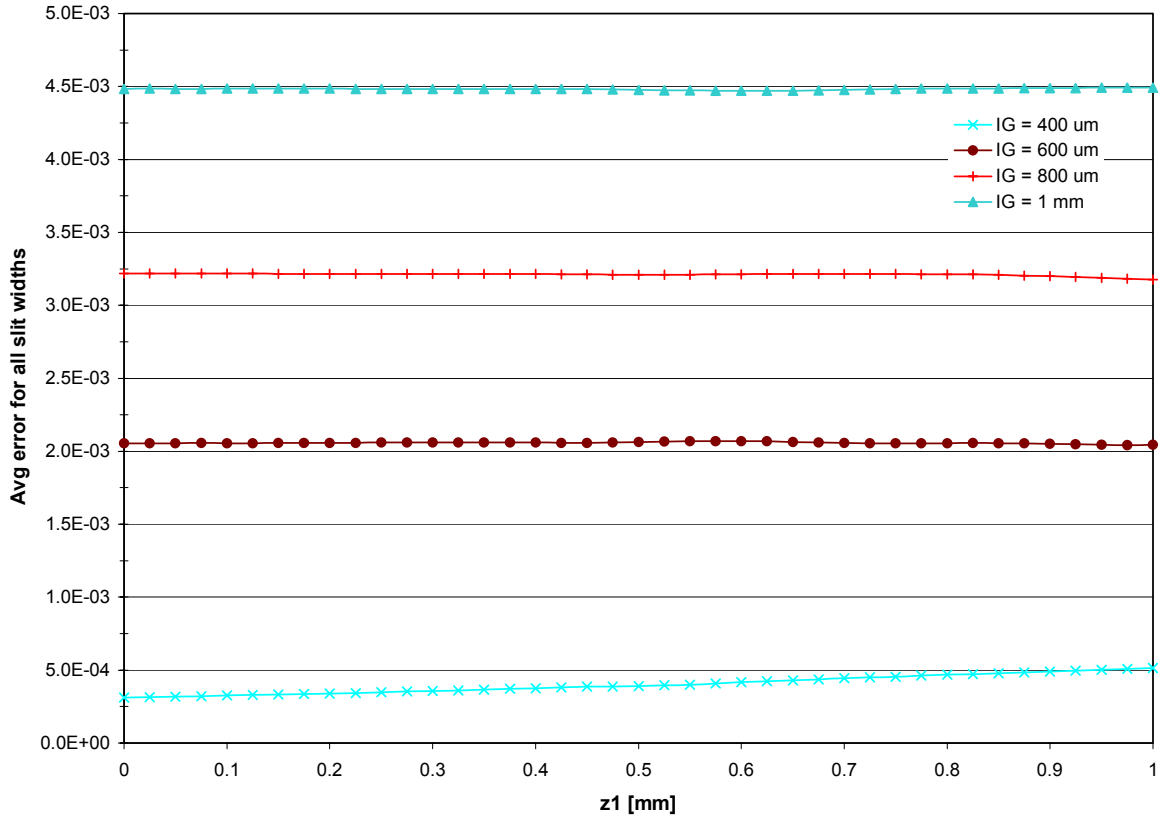

Figure 12: System Response to Long Inter-grating Distances

Figure 13 illustrates the effect of imperfectly spaced gratings. The computations were carried out for two cases, where slits were offset by ± 1.5625 μm from their nominal position. That resulted into relatively uneven slit spacing. The dramatic effects of this modification are illustrated for the 200 and 600 μm inter-grating distances. The results indicate that uneven spacing increases the error by almost an order of magnitude. For comparison purposes, the nominally spaced slit cases at 200 and 400 μm are also displayed. Interestingly, the error appears to remain approximately constant over the whole z_1 range. The results presented in Figure 13 should, however, be interpreted with caution, since the limited pixel grid size may have skewed the results. These results should be verified by experimentation.

The slit height and slit spacing values must be carefully evaluated. For one, long slits tend to reduce the effect of diffraction but this is achieved at the expense of a reduction of the beam modulation in response to a given pressure. Small slits on the other hand tend to even out beam non-uniformities, a desirable feature since this relaxes the requirements on local beam intensity non-uniformities. Clearly, selection of the grating slit height results from a tradeoff among many different parameters.

Analysis of the diaphragm based on materials characteristics, life expectancy (cycles) and physical size constraints indicates that the diaphragm's physical displacement in response to the maximum pressure is about 25 μm. It was also shown previously that the sensor's response is truly linear only in the middle portion of the operating range. Taken together these two factors impose a maximum slit height of about 50 μm unless linearization is used.

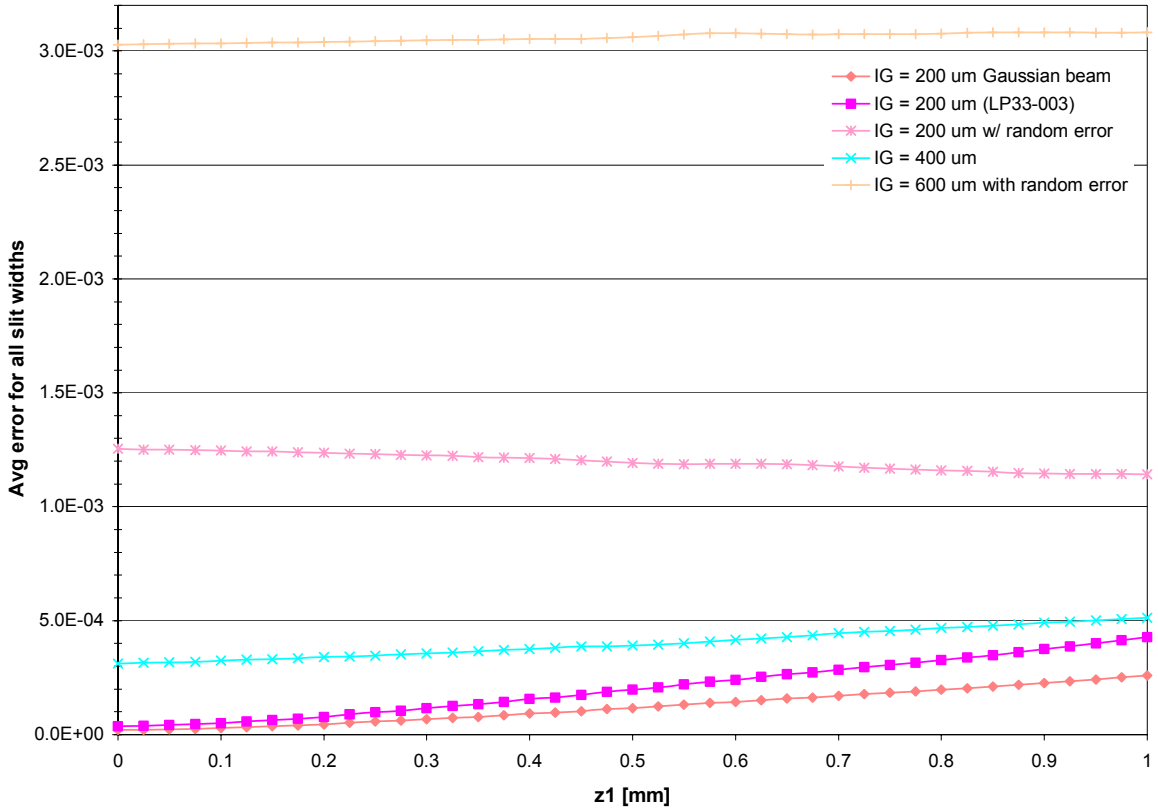

Figure 13: Effect of Gaussian Beam and Irregular Slit Spacing on System Response

Mechanical tolerances must also be accounted for. The rationale for this is that the relative positioning of the moving grid with reference to the reference (fixed) grid dictates the no-input operating set point of the sensor. Allowing a 0.001" (25 μm) tolerance would bring the required slit height to a minimum of 75 μm. If the temperature-induced relative positioning fluctuations between the moving and reference grids are further added, a minimum slit height of 100 μm is required.

Once the slit height has been established, the overall grating size can be determined. A relatively large number of slits is desirable to reduce the optical beam intensity uniformity requirements. On the other hand, the sensor size is a critical design parameter. An iterative design process led to the selection

of a beam size of 1.5 mm. Using a 100 μm slit spacing therefore implies that 7 or 8 slits will be used to cover the optical beam, a number that is considered sufficient to reduce the beam non-uniformity effect. The grating itself must nevertheless be slightly larger than that and an overall width and height of about 2 mm is recommended.

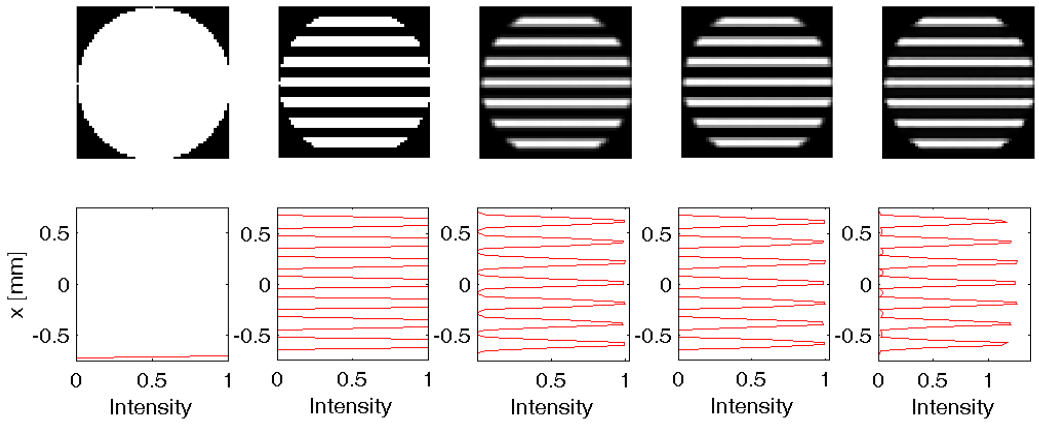

Figure 14: Pattern of Light (top) and Intensity Profile at Various Locations Along the Light Path

Figure 14 presents a graphical representation as well as the intensity distribution of the light beam at various locations along the beam trajectory. The leftmost figure depicts the beam immediately at the exit of the circular aperture from which the beam is emitted. The following figures successively display the energy field immediately after the second grating, before the second grating, after the second grating and at the detector plane. All beam intensity profiles are vertical cross sections through the image centre. The detector was located 1.47 mm away from the second grid, the wavelength was set to 800 nm and the grids were spaced 200 μm apart. The slit height was set to 200 μm. Again, note that that these results are simulations based on an imperfect model and these results should be validated by experimentation. Most notably, lenses and beam divergence were not modeled in Figure 14.

2.3.2 Optical Design

So far, the discussion has addressed the conceptual aspects of system design. This section and the following now explore the physical implementation aspects of the selected design. In the following paragraphs, selection of a light source as well as its injection and collection are investigated. Later sections deal with mechanical and signal processing issues.

For obvious reasons, the light source modulated by the sensor cannot be built into the sensor. The light beam must therefore be injected and collected back with optics. Direct injection is not practical and fibre optics technology (or its derivatives such as fibre bundles, light pipes or light guides) must be used. Collectively, these technologies will be referred to as *light conduits*, not to be confused with the *light path*, which corresponds to the path followed by a light beam, be it guided or propagating in free space.

2.3.2.1 Internal Geometry

The cost of components, their resistance and longevity in the operating environment as well as the available physical space must all be considered when selecting an input/output optics approach. A further restriction to the internal geometry is imposed by the allowable sensor's maximum diameter.

Since the sensor is operated in transmission, the light source and the detector must be positioned on opposite sides of the grids unless a reflective element is used on one side. This latter approach was not retained to avoid the added complexity and the potential degradation of the reflective surface. However, the need for a detector and a source on opposite sides of the grids limits the potential geometries as neither the source nor the detector can be positioned parallel to the diaphragm. If the diaphragm is imagined positioned in an horizontal orientation, then both the source and the detector must lie on a horizontal plane parallel to the diaphragm. Consequently, there must be two light conduits exiting radially from the sensor. Alternatively, the conduits – or the light paths leading to the conduits – can be bent or folded and then grouped together to exit the sensor at a single point.

The former approach is not desirable as it increases the overall system encumbrance, add to the overall sensor cost, and restricts the retrofit capabilities of the sensor to motor makes and models with enough clearance for two cables. Therefore, both light conduits must exit on the same side or through the bottom of the sensor. Having the two conduits exit on one side is slightly better than having them on opposite sides but still adds to the physical encumbrance of the sensor. It also requires either 90° bends on both light paths (or light conduits), or one 180° bend on one side. Clearly, this solution is not desirable either. Therefore, both the input and output must exit from the bottom of the sensor and this imposes 90° bends on both input and output.

The required beam size inside the sensor, derived in a previous section, is also a factor influencing the design of the input/output optics. We recall that the beam must be at least 1.5 mm in diameter.

2.3.2.2 Input/Output Optics

Light Propagation Means

Most optical fibres have core diameters much lower than the required beam diameter.[6] This, coupled to the fact that the beam divergence at the output of an optical fibre is generally large, leads to the conclusion that output optics are required to expand and collimate the beam output if optical fibres are used, since a divergent beam is not desirable. Light guides and fibre bundles also have large divergence angles and consequently also require some collimating optics. Therefore, no matter what solution is retained, some optical components are required in the sensor between the source and the detector. On the other hand, light conduits (either fibre conduits or fibre bundles) have a large diameter that gives them a significant advantage over single fibres when efficient coupling from a wide-area LED source is required. Owing to their large size, alignment tolerances can also be reduced.

By contrast with optical fibres and fibre bundles, which are easily damaged (due to the presence of small scratches or irregularities on the surface) when left without a protective coating, fibre conduits can be used without an external protective coating. These advantages nevertheless come at the expense of a greater cost. Depending on the actual implementation, fibre bundles (and fibre conduits to a lesser extent) may have an effective cross-sectional area much lower than the real area (this parameter is generally quoted as the fill factor or the packing ratio). This leads to a reduction in the amount of light actually being guided by the light conduit.

Fibre conduits may be permanently bent in any orientation by heating and the minimum bend radius is typically four times the rod diameter. Fibre bundles of same diameter have bend radius of 4 to 6 times the radius while individual fibres' long-term minimum bend radius is typically 100 to 600 times the fibre radius. However, while they may be permanently bent, fibre conduits are not flexible and therefore cannot, for obvious reasons, be used to transport light from and to the drive electronics located 2 to 3 m

[6] Plastic optical fibres (POF) are one notable exception but these have disregarded owing to their low fusion point.

away. As such, an interface between a fibre conduit and an optical fibre or bundle would be required. This would add even more complexity and cost to the system and the fibre conduit solution must be rejected.

A fibre bundle 1.5 mm in diameter would have a minimum bend radius of 6 mm. Since two such bends are required, the bundle bending approach would, in this case, require a minimum of 12 mm of clearance, plus the extra space required for the collimating optics. This physical extent would be augmented by the space taken by the grid assembly and the sensor's wall thickness. The same reasoning for individual fibres would lead to roughly the same values.

A similar reasoning can be applied to individual fibres. While the bend radius of individual fibres is slightly lower, the extra length required by the focal length of the lens to increase the beam size to 1.5 mm, would still yield values in the same range. Consequently, given the overall size and encumbrance requirements, bending is not an option, and the optical path must be folded.

Aside from physical considerations, the design of the optical fibre itself (type and material) must also be carefully selected. Typically, a step index optical fibre is made out of a core surrounded by a concentric layer of cladding. The two layers are made of materials whose refractive indices are selected so that total internal reflection occurs at the core/clad interface. In this fashion, the light is guided along the fibre.

To achieve the required refractive indices, the glass core is generally doped so that its refractive index (n_i) is higher than the surrounding cladding material index n_o (usually made out of pure silica). However, at high temperatures, the core dopant may start diffusing in the clad, resulting in a change of the fibre's optical properties.[7] The solution to this problem involves using a pure silica core and a fluorine-doped clad (these fibres are sometimes called silica/silica, pure silica or quartz fibres). Graded index optical fibres fair even worse at high temperatures due to their continuously variable index profile. For that reason, this fibre type will no longer be considered. Pure silica fibres also have better and more uniform attenuation properties throughout the operating range of interest and are generally preferred for sensor and spectrometry applications.

Fibres manufactured for the telecommunications industry are generally manufactured with a germanium-doped core with pure silica cladding due to the extreme expense of the alternative – pure silica core, fluorine-doped silica clad. The reason is that, in telecommunications applications where the fibre core is a small fraction of the overall fibre volume, it is less expensive to dope the core than the cladding. The opposite is true in specialty fibre applications, where the core constitutes the bulk of the volume of the fibre. A general conclusion from the above discussion is that the fibre design selected should seek to maximize the core-to-clad dimension ratio (CCDR) in order to minimize cost. It is also worth noting that fibre bundles, being made of a series of fibres packed together, are bound to follow the same rules.

Sapphire fibres[8] are another option. They can tolerate temperatures up to 2000°C, are almost chemically inert and can withstand severe abrasion. As such, their performance is impressive. The solution was, however, not further considered since these fibres are relatively rigid, come in short lengths, and are expensive. Moreover, sapphire's high refractive index would result in large losses at the air/fibre interface.

The outer protective coating or *buffer* around the fibre's cladding must also be selected with care. In the telecommunications industry, it is customary to use a plastic coating such as nylon or acrylate. However, these materials cannot withstand elevated temperatures and different materials must be envisaged.

[7] Opinions vary on the temperature Ge-doped fibres can endure. In light of the targeted lifespan, the safest approach was retained. See for example www.nasatech.com/Briefs/Sept00/LEW16889.html and www.nasatech.com/Briefs/Oct98/LEW16264.html.

[8] See for example www.saphikon.com.

At high temperatures, polyimide is frequently used but its operating range is limited to temperatures lower than 385 to 400°C unless the fibre is operated in an oxygen-free atmosphere. Additionally, polyimide-buffered fibres are notoriously sensitive to microbend-induced losses. The remaining alternatives are metal-coated fibres. Gold, platinum, aluminum and copper are the materials of choice. Being specialty products, these fibres also command a high price and make the fibre bundle approach not cost-effective.

Thus, individual fibres represent a better alternative. However, even individual metal-coated fibres are costly. A more cost-effective approach consists in splicing a length of metal-coated fibre to another, cheaper fibre. The length of metal-coated fibre is selected so that, at the splicing distance, the ambient temperature has decreased to a point where it falls within the operating range of the cheaper fibre.

Aluminium, copper, gold and platinum are the materials generally used to overcoat fibres for high-vacuum or high-temperature applications. Aluminium is a good choice for temperatures up to 400°C and is not suitable for the current application. Copper is an interesting alternative with a typical heat resistance up to 600°C (750°C if a copper/nickel alloy is used). Further, copper-clad fibres can be brazed to ferrules and connectors, etc. Gold is rated up to 750°C and gold-coated fibres can be welded to connectors and ferrules. Given the wide acceptance and larger availability of gold-coated fibres, this latter material was selected. Further advantages of metal-coated fibres include good stress corrosion immunity[9] and a very high tensile strength, with a corresponding reduction in the strain relief needs.

Optical Fibre Parameters

The design of the optical power delivery and sensing portion of the sensor also requires that the fibres' mode type, size and numerical aperture be determined.

Optical fibres can be divided into two broad categories: single-mode (SM) and multimode (MM) fibres. The two types are differentiated by the optical propagation modes they support. Without going into details, it can be said that single-mode fibres have smaller cores than multimode fibres. Their smaller core implies that less energy can be coupled into the fibre from an extended source. However, this smaller size also facilitates beam collimation since the source then is a better approximation of a point source.

For total internal reflection to occur, the index of refraction of the glass in the core (n_i) must be greater than the index refraction of the glass cladding (n_o). The sine of the half angle θ of the light that will be accepted into the core (or emitted) is defined as the numerical aperture (*NA*) and is given by the formula

$$NA = \sin\theta = \sqrt{n_i - n_o} \tag{2.6}$$

The F-number (F/#) notion is related to the numerical aperture by the relations

$$\begin{aligned} F\# &= 1/(2 \cdot NA) \\ &= f / D \end{aligned} \tag{2.7}$$

where *D* is the lens or system diameter and *f* its focal length. Single-mode fibres with germanium-doped cores clad with pure silica generally have numerical apertures in the vicinity of 0.12 whereas pure silica multimode fibres have numerical apertures around 0.22.

[9] See Fiberguide industries guide at http://www.fiberguide.com/frames/frame_products.htm

Albeit single-mode fibres are easier to collimate, the longer operating distance (lower N.A.), their small core size and the resulting low coupling efficiency and alignment complexity makes them less attractive for this application. Consequently, this option was discarded and multimode fibres were selected.

From the above discussion, it appears that individual gold-coated fibres should be used. To remain cost-effective, splicing of polyimide-coated fibres to short sections of gold-coated fibres should be used.

Specialty fibre preforms are usually commercially available in CCDR ratios of 1:1.05, 1:1.01, 1:1.2 and 1:1.4. Since the cladding is expensive with respect to the core, a higher CCDR should be sought. All these requirements lead to the selection of a fibre with a numerical aperture of 0.22, a core of 100 μm, a cladding of 40 μm and a 30-μm metal coating for a total size of 170 μm. The core-to-clad ratio selected is dictated by the available fibre preforms while the actual size is a result of the tradeoff between a large fibre and the aberrations (collimation) associated with large fibres.

Manufacturers producing and/or selling pure silica fibres and/or metal-coated fibres include Avantes, Artphotonics, Calphotonics, CeramOptec, Fiberguide Industries, Innovative Fibers, Newport (sensor grade fibres) Nufern, Oxford Electronics, Polymicro, Spectran, Silica Physics, Sintec Optronics and Waveoptics. A number of those manufacturers were contacted and Silica Physics provided us samples of silica/silica gold/polyimide-buffered spliced fibres.

Optical Chain Interconnections

Injection of the optical power into the fibres must be thought out with care. Both measurement channels must share the same light source since using two different sources would defeat the very purpose of the differential approach, namely perturbation cancellation. This requirement can be met in two ways. For one, both fibres can be encased into a ferrule and crimped onto the LED source. This method is potentially cost-efficient, provided the crimping and alignment process is not too labour-intensive. The alignment constraint is necessary to prevent the optical power injected in the two fibres from differing too much. While slight variations could be handled without significant sensor performance impact, large variations would result in assembly problems and potentially costly assembly rework.

The other method involves a fibre-optic coupler or a bifurcated fibre. Fibre couplers are available in many configurations. For this application, the preferred configuration is a 1×2 coupler although more readily available 2×2 couplers could also be used. The advantage of couplers is a repetitive and proven coupling method, a performance achieved at higher cost. For prototyping purposes, the coupler is by far preferable since it simplifies assembly. Figure 15 depicts the two approaches. In both cases, the percentage of light being injected into each fibre should, inasmuch as possible, remain constant to avoid temperature-induced measurement fluctuations.

Suitable optical couplers are available from Gould, FIS (F1-93205 1x2 900 um $49 USD; F1-93205-IM-900 1x2 900 um $60 USD), Telogtech, Metrotek and OZ Optics to name a few.

The connections between the source, the transport fibres and the detectors as well as the sensor/fibres and fibres/drive electronics also deserve particular attention in light of the difficult operating environment. As a general principle, the number of connections should be minimized for increase robustness. For the same reason, a rugged outer sheath should surround the launch and reception optical fibres between the sensor head and the electronics module. Given the dusty, wet and oily environment in which the sensor is to operate, the fibres should be terminated within the electronics enclosure and the sheath should be mated to a grommet at the enclosure/cable interface. Interconnections between the sensor and

the cable should obey the same logic: there shall be no connector on the sensor side for ruggedness, assembly and space availability considerations.

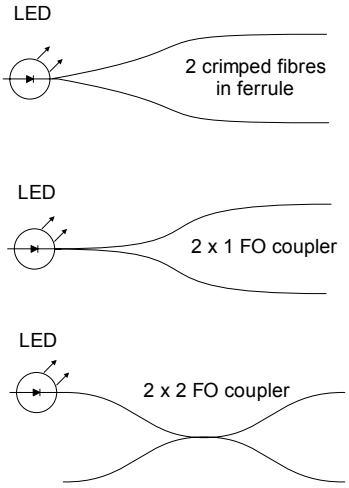

Figure 15: Sensor-to-Signal Conditioning Configuration

On the other hand, assembly considerations dictate that there should be at least one mating/de-mating connection point. With the coupler approach, the connection point is ideally located at the LED/coupler interface while the coupler-to-fibre interface should be achieved through a fibre splice located inside the enclosure. If a ferrule approach is used, the mating connection point can be located at the LED/fibre interface if the ferrule-to-LED mating alignment is repetitive enough to sustain multiple mate/de-mate cycles. Otherwise, it is probably preferable to use individual connectors at the fibre level within the enclosure. Figure 16 summarizes the two optical chain interconnection approaches.

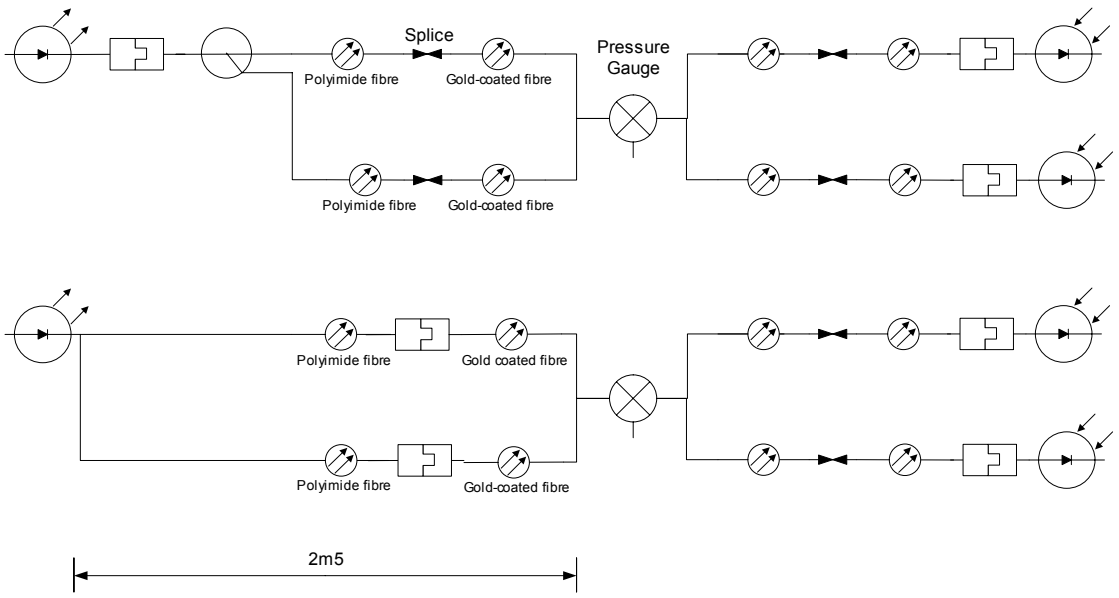

Figure 16: Variants of Optical Chain Interconnections

For the remainder of this technical discussion, it will be assumed that a connectorized coupler is used for prototyping, and the optical budget will be derived accordingly.

2.3.2.3 Collimating/Focussing Optics

We have already established the need for 90° bends in the optical path as well as for collimating optics. Therefore, the objective of the optical system is to collimate the power from a fibre while maintaining divergence and aberrations to a minimum. We have also established that the required path folding could not be achieved with optical fibres. Hence, some refractive or reflective optics must be used. Among the many concepts envisaged, a design combining the path folding and the collimating optics into a single device was finally retained.

The underlying idea behind the optical design is to use a prism in total internal reflection (TIR) as the path folding mechanism and shape the prism face in such a way that it can act as collimating optics as well. The concept is illustrated in Figure 17. The resulting half ball design can be simply and economically realized by grinding a ball lens until the desired shape is obtained. Note that the back face of the lens acting as a mirror does not need to be metallized since total internal reflection is used. However, this face should be kept clean to prevent light from escaping at this interface. Numerous lens designs such as drum and aspheric lenses based on this approach were evaluated and a simple ball lens design was selected because of its widespread use and simple, cost-efficient design. Also note that the same design will be used for both collimation and focusing purposes.

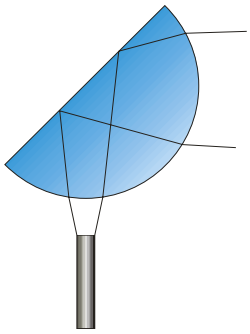

Figure 17: Path Folding and Collimation Principle

Graded refractive index materials would have been interesting in this context but, again, the high operating temperatures precluded their use for fear of gradual performance degradation through dopant diffusion. Total internal reflection also required a high refractive index material, and a low coefficient of thermal expansion was desirable to maintain the optical properties throughout the temperature operating range. Sapphire was selected for its high refractive index and good temperature behaviour (n = 1.77 and α = 8.4×10^{-6} K^{-1}). Zerodur and fused silica (alpha = 0.2 x 10^{-7} and 0.5 x 10^{-6} respectively) have a better temperature coefficient but their refractive index is much lower.

Total internal reflection occurs whenever the incident angle θ_i satisfies the relationship

$$\theta_i \geq \sin^{-1}(n'/n) \tag{2.8}$$

where the incident angle θ_i is measured perpendicular to the normal of the interface at which total internal reflection occurs, *n´* is the refractive index of air and *n* the refractive index of sapphire. It is easy to show that the above condition is satisfied whenever θ_i is greater than 34º.

We must now ensure that the divergence of the beam inside the lens is small enough that extreme rays hit the back face of the lens (where the reflection occurs) at an angle that satisfies the total internal reflection relationship. The rays exit the optical fibres at a maximum angle given by the fibre's numerical aperture. With *NA* = 0.22, the maximum angle is 13º. This angle is further reduced when the rays enter into the sapphire lens. That beam divergence inside the lens can be derived from Snell's law:

$$n_i \sin\theta_i = n_o \sin\theta_o \tag{2.9}$$

With n_i and n_o equal to 1.0 and 1.77 respectively, we obtain θ_o = 7.13 for θ_i = 12.7º. Since the back face of the lens is oriented at a 45º angle with respect to the fibre, the minimum angle between the normal the beam rays is 45 – 7.1 or 37.9. The total internal reflection criterion is therefore always satisfied with a safety margin of 3.9º.

An infinite conjugate ratio system is a system whose image or object is at infinity. Collimating a point source is an example of such infinite conjugate ratio system. For these systems, the best singlet form is a plano-convex lens. Thus, the system illustrated in Figure 17 is not optimal since a biconvex lens is used.

Moving on with the optical design, we find that the entrance pupil size and source numerical aperture (fibre's core size and *NA*), the collimated beam size and the lens material are now all fixed. The remaining free parameters are the lens focal length and diameter. The required focal length can be determined by first computing the numerical aperture required. This will determine the ball lens diameter from which the focal length will be derived. The numerical aperture a ball lens is given by

$$NA_{ball} = 2d(n-1)/nD \tag{2.10}$$

where *d* is the input (output) beam diameter as shown in Figure 18. The validity of the above equation falls off with increasing d/D ratios as a result of inherent spherical aberrations of ball lenses.

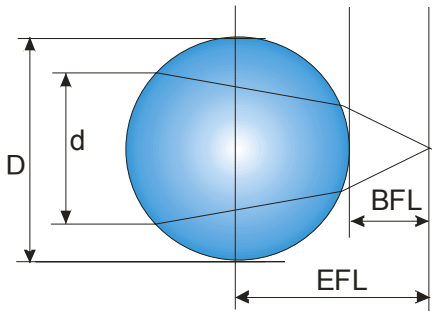

Figure 18: Ball Lens Main Dimensions

From fundamental optics, we also know that the minimum divergence that can be achieved with any lens system used as a collimator is the source size divided by the focal length. The source size being fixed by design (fibre core), one should seek to maximize the focal length but this requirement goes

against the overall sensor size limitation. Furthermore, in order to inject all of the light emitted by the fibre into the lens, the numerical aperture of the lens must be smaller (greater acceptance cone) than the numerical aperture of the fibre. It follows that

$$2d(n-1)/nD \geq 0.22 \tag{2.11}$$

Setting *d* = 1.5 mm and *n* = 1.77 implies that the diameter of the ball lens *D* should be smaller than 5.93 mm. Lenses are available in standard diameters and the closest value meeting the requirements are 5.55 and 6.0 mm. The latter value is slightly too high, but if the collimated beam size is reduced to 1.25 mm, a 6 mm diameter ball lens can be used to benefit from the larger focal length (smaller divergence and less aberrations).

The effective focal length of a ball lens is simply given by

$$EFL = nD/4(n-1) \tag{2.12}$$

where *n* is the refractive index of the lens and *D* its diameter. Note that the reflection inside the ball lens does not modify the effective focal length of the configuration illustrated in Figure 17, as the reflection can be 'unfolded' to fall back on a transmission through a ball lens case.

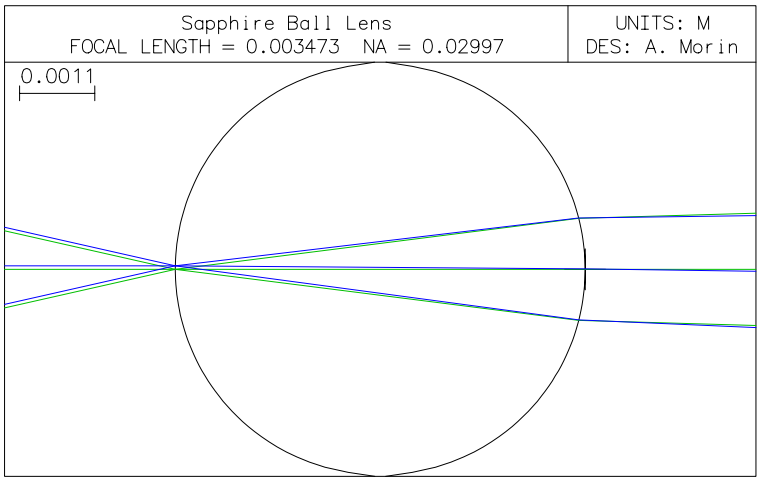

Figure 19: OSLO© Ray Tracing for a 50-µm Core Fibre in Contact with a Sapphire Ball Lens (ray tracing for upper part of object only)

With the parameters already calculated, the effective focal length is found to be *EFL* = 3.448 mm. This value is in good agreement with formal computations carried out with the OSLO™ optical design software, which indicates a 3.473 mm effective focal length (see Figure 19). The effective focal length allows us to calculate the best collimated beam divergence we can expect. The divergence is given by

$$\tan(divergence) = d/BFL \tag{2.13}$$

where *d* is the collimated beam size and *BFL* the back focal length of the ball lens.

In turn the *BFL*, defined in Figure 18, is given by

$$BFL = EFL - D/2 \tag{2.14}$$

so that *BFL* = 0.448 mm. The divergence is then 1.22º. We can check this value against the minimum divergence attainable with any lens system, using

$$\min(divergence) = SourceSize / focalLength \tag{2.15}$$

By comparison, the minimum divergence theoretically attainable with a 1.25 mm beam and a 50-μm core fibre is 0.004 rad or 0.22º.

Figure 20 illustrates the effect of moving the input fibre away from the lens surface. By comparison with Figure 19, we can see that the divergence has diminished at the expense of some convergence. The analysis of the exact effects of positioning on the system is beyond the scope of this project, however, and is best addressed experimentally, most particularly in light of all second-order effects neglected in this analysis. Figure 21, derived from a Matlab simulation,[10] illustrates a series of geometrical fibre/lens combination and illustrates their effects on the divergence at the output.

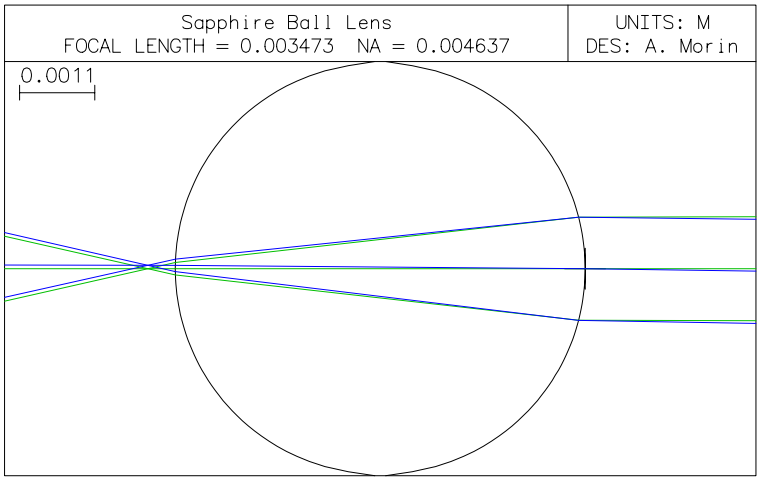

Figure 20: OSLO© Ray Tracing for a 100-μm Fibre 400 μm Away from the Ball Lens Surface (ray tracing for upper part of object only)

Lastly, we must ensure that the system, when used in the focusing mode, is not diffraction limited. The diffraction limit (*D.L.*) is given by

$$D.L. = 2.44 \times \lambda \times f/\# = 4.4\,\mu m \tag{2.16}$$

and indicates a diffraction limit much lower than the fibre core diameter.

[10] Reprinted with permission from Charles Gautier.

2.3.2.4 Light Source Selection

Light source selection criteria include cost, longevity, wavelength range, intensity stability over time, and, most importantly, the availability of adequate detectors at the wavelength selected.

The source selection process can be narrowed down by first identifying the source type. Source types include white lights (incandescent), neon lamps, LEDs and lasers. While other types exist (flash and arc lamps, glow bars), these are more exotic in the context and will no longer be discussed.

Laser sources do not offer any specific advantages over white lights and LEDs. They are generally more expensive than the latter two types. Furthermore, as pointed out earlier, a narrow spectrum is not required. White lights (incandescent) offer a low-cost advantage but their lifetime, while sometimes appreciable, is generally lower than LEDs. In addition, their optical power density is lower than LED intensity and their pattern of emission does not easily lend itself to launching into optical fibres.

Thus, in light of their good lifetime, stability, and low cost, LEDs should be favoured in this application. Having established the source type, there remains to establish the wavelength range before selecting a particular component (or family of components).

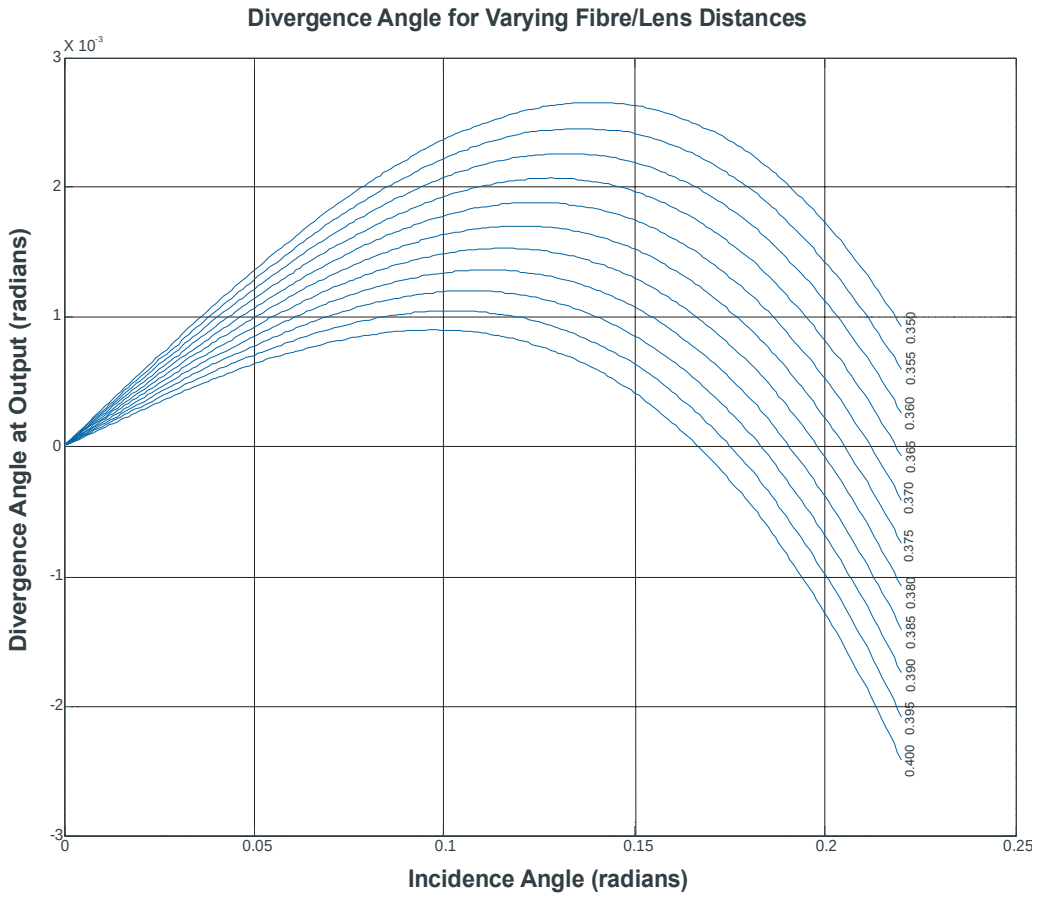

Figure 21: Effect of Lens/Fibre Separation on Output Divergence

LEDs are nowadays available in the 400 nm to 1.5 μm wavelength range. As previously discussed, shorter wavelengths should be preferred over longer wavelength devices in view of the lowered susceptibility of shorter wavelengths to diffraction. This general trend must nevertheless be traded off against cost and lifetime. The optical properties of the source and collection optics must also be considered. The 800 nm range (780-850 nm) was selected owing to its relatively short wavelength, wide availability, and the good sensitivity of low-cost silicon detectors in that wavelength range.

LEDs manufacturers include Stanley, Optel, Optek, Agilent, American Zettler, QT Optoelectronics (now part of Fairchild Semiconductors), NEC, Sharp, Siemens, Industrial Fiber Optics, etc.

Designed for telecommunications, the HFBR-14X2 and 14X4[11] series of emitters from HP, operating at 820 nm, represent an interesting choice. In addition, reliability data is provided thereby providing a way to estimate minimum lifetime. They are available as ST, FC, SC and SMA fibre-connectorized board-mountable receptacles. The OPF342A and OPF322A,[12] emitting at 850 nm, constitute another alternative with similar characteristics. Both can typically inject a minimum of about –16 to –17 dBm (roughly 20 μW) into a 50-μm core fibre @ 100 mA drive current. The injected power nonetheless quickly rises with larger fibre core diameters as shown in Table 1.

While not strictly required, receptacle-mounted (or *housed*) devices are preferable as they ease fibre-to-detector alignment during manufacturing. This advantage should nonetheless be weighed against the higher cost of encased photodiodes.

Table 1: Injected Power for Different LED Devices and Fibre Core Sizes

Device	Core Size (μm)	Typ. Injected Power	Min. Injected Power	Test Conditions
OPF322A	50	19 μW	15 μW	@25°C; NA = 0.2 50 um core; I = 100 mA
	62.5	34 μW	N.A.	@25°C; I = 100 mA
	100	95 μW	N.A.	@25°C; I = 100 mA
OPF342A	50	25 μW	20 μW	@25°C; I = 100 mA
	62.5	45 μW	N.A.	@25°C; I = 100 mA
	100	125 μW	N.A.	@25°C; I = 100 mA
HFBR-14X4	50	-16 dBm	-19 dBm	@25°C; NA = 0.2; I = 100 mA
	62.5	-12 dBm	-15 dBm	@25°C; NA = 0.275; I = 100 mA
	100	-6.5 dBm	-9.6 dBm	@25°C; NA = 0.3 ; I = 100 mA

2.3.2.5 Detector

Detector selection is primarily dictated by the wavelength of light to be detected. At the selected 800 nm wavelength, silicon detectors are a natural choice.[13] The typical spectral responsivity curve shown in Figure 22 indicates that Si photodiodes will exhibit a good responsivity to any source in the 780-910 nm wavelength range.

[11] See datasheets in Appendix F.
[12] See datasheets in Appendix F.
[13] There are also a few GaAlAs specialty detectors with a narrow sensitivity band tuned around 850 nm but these are specialty detectors optimized for use when background light is present.

There is a wide selection of silicon detector types and operating modes optimized for various applications, and additional criteria are required to narrow the options down to a few families. Our main criteria are, again, sensitivity, linearity, and cost. Note that there is no need for very high-speed detectors as is often the case in telecommunications applications.

Based on these criteria, a few families can be ruled out. Avalanche photodiodes for example are neither required (there is no need for their very high speed) nor desirable because of their cost. Photoconductive devices (not to be confused with photodiodes used in the photoconductive mode) can also be ruled out. This leaves common PN and PIN photodiodes and phototransistors. Photodiodes are preferable over phototransistors in terms of linearity, stability, and device-to-device repeatability.[14] On the other hand, phototransistors have inherent gain that make them somewhat more robust and present a slightly better cost-to-performance ratio.

In any case, the device should be operated in the unbiased, photovoltaic mode rather than in the biased, photoconductive mode of operation for optimal linearity and lowest noise level. This stems from the fact that the dark current, the major contributor to noise, is proportional to the amount of bias. When unbiased, photodiodes are extremely linear over many orders of magnitude, the lower limit being the NEP (noise equivalent power) while the upper limit is dictated by the saturation power. Note that this gain is usually achieved at the expense of a slightly reduced sensitivity.

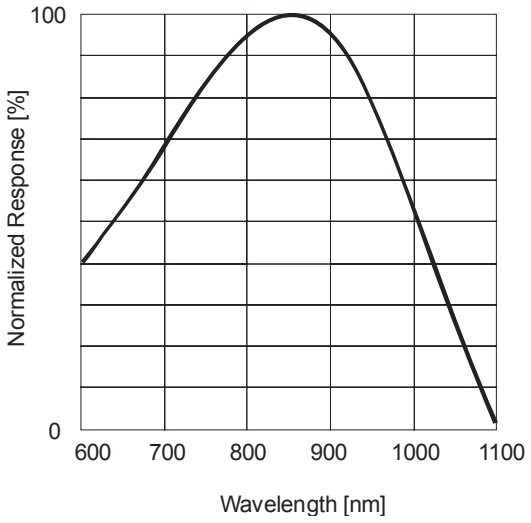

Figure 22: Typical Optek GaAsAl Photodiode Responsivity

Detectors are available in many configurations ranging from bare units to complete modules integrated with amplification electronics, etc. Bare detectors are not much cheaper than detectors encased in FO receptacles and offer less convenience. As a result, the detector should at least be encased in a receptacle to ease the fibre-to-detector interface. Owing to the low signal levels, devices with integrated transimpedance amplifiers should be favoured unless a discrete photodiode/amplifier combination of similar performance level can be produced at a lower cost.

Perkin Elmer (formerly EG&G/RCA), AMP, Hewlett Packard (Agilent), Opto-Diode, Optek, Honeywell, Hamamatsu, Micropac, and Silicon Detector – to name a few – provide a full array of photodiodes. Silicon Sensors and Silonex, based in Montreal, also develop custom solutions.

[14] See Perkin Elmer web site at http://optoelectronics.perkinelmer.com/library/papers/tp4.asp for a complete description of families advantages.

HP's HFBR-24X6 is the companion to the HFBR-14XX series of emitters. Housed in a metallic device, it includes a transimpedance amplifier and has an analog output. It is intended to be used as a communication device, is consequently optimized for AC applications and generates a high DC level at zero optical power level. Unfortunately, there is no way to distinguish this DC offset (which can vary over time and temperature) from the real signal unless sophisticated signal processing is used. One example of a workaround solution involves modulating the source at a frequency much higher than the maximum frequency to be detected (say from 200 to 1000 kHz) and average the signal out after detection. The drawbacks to this approach are a) expensive post-processing and b) a twofold drop in signal strength (assuming a 50% duty modulation of the optical source).

A better solution is Optek's OPF472. Packaged as a metallized receptacle, it is offered with an SMA or ST port but does not offer a built-in transimpedance amplifier. Alternatives are the OPF2404 and OPF540 from the same manufacturer. The OPF540 comes as a photodiode/transimpedance amplifier combination. It is not housed in an FO receptacle but can be snapped without need for alignment onto any 0.228″ dia. bore FO receptacle. However, no information is available on the DC voltage at the output.

2.3.3 Signal Conditioning and Processing

Signal conditioning is, to a large extent, dictated by the optical power levels available. In fact, a strong signal does not be need to be handled with the same level of care than a faint signal. Thus, determination of the signal processing method presupposes computation of an estimate of the power at the receiver.

The optical power budget can be derived from the following equation

$$P_{\mathrm{Re}c} = P_{Source} \times C_{SF} \times A_{FF} \times C_{FL} \times L_{RL} \times L_{TR} \times A_{GG} \times L_{RL} \times L_{TR} \times C_{LF} \times A_{FF} \times C_{FR} \times M_{GG} \quad (2.17)$$

where

P_{Source} =	Power available at the emitter (source);
C_{SF} =	Source-to-fibre coupling;
A_{FF} =	Fibre attenuation (including FO coupler if any);
C_{FL} =	Fibre-to lens coupling;
L_{RL} =	Lens reflection losses;
L_{TR} =	Lens transmissivity;
A_{GG} =	Grating attenuation due to first grid (mask coverage);
C_{LF} =	Lens-to-fibre coupling;
C_{FR} =	Fibre-to receiver coupling;
M_{GG} =	Grating modulation (0 to 100%).

We also note that

$$V_{Rec} = \eta_{Rec} \times P_{Rec} \times R_{FD} \quad (2.18)$$

where V is the voltage at the output of the amplifier, η is the receiver efficiency (in [A/W]) and R_{FD} the feedback resistor value. Whenever a built-in transimpedance amplifier is available, the product $\eta \times R_{FD}$ is given by the manufacturer and expressed in units of [V/W].

The minimum input power available at the end of 1 m of fibre is, for both Optek and HP emitters, about –9.3 dBm or 115 μW. This value accounts for both P_{Source} and C_{SF}. If we add an optical coupler, an additional –3 dB for the coupler (splitting of available power into two fibres) plus another –1 dB for the FO connector interfaces, for a total of –4 dB, must be added.

The attenuation in the fibre itself is typically 3 dB/km or a negligible –0.01 dB for 5 m. This value can be increased to –0.1 dB if we take into account the polyimide/gold–coated fibre splice. The attenuation A_{GG} due to the grid is about 50% since the grid has a 50% duty cycle, or –3 dB. The coupling between the fibre and the lens is almost perfect and, for all practical purposes, we can set this contribution to zero.

The losses at the lens/air interface can be estimated with Fresnel's law. Hence we have

$$R = \left(\frac{1-p}{1+p}\right)^2 \tag{2.19}$$

with $p = n_1/n_2$, the ratio of the refractive indices. For sapphire n = 1.77, R = 0.005. Two interfaces will yield a 10% loss for two interfaces or roughly –0.5 dB.

The transmission losses L_{TR} within the sapphire material are somewhat negligible, the absorption coefficient being 0.3 x 10^{-3} cm^{-1}. For a 6 mm travel, the attenuation is negligible at 1.8 x 10^{-5}. Lastly, we assume that the photodiode is housed in such a way that the optical losses at the fibre-to-receiver (C_{FR}) interface can be neglected. Thus,

$$\begin{aligned} P_{Rec}(dBm) &= -9.3 - 4 - 0.1 - 0.5 - 3 - 0.5 - 0.1 \\ &= -17.5dBm \end{aligned} \tag{2.20}$$

This translates into 18 μW of optical power at full signal strength (aligned grids). For a minimum 5 mV/μW (for both Optek and HP emitters) responsivity, equation (2.18) gives a signal of 90 mV.

Armed with this value, we can now calculate the signal-to-noise ratio or SNR. The voltage SNR is defined as

$$SNR = \frac{V_{Rec}}{V_{Noise}} \tag{2.21}$$

The noise voltage is the RMS summation of many sources such a signal shot noise, dark current shot noise, detector Johnson noise (due to shunt resistance), feedback resistor Johnson noise, amplifier 'excess' noise, etc. Whenever a transimpedance amplifier is integrated with the detector, the quoted noise figure includes all these noise components.

Optek's OPF540 and OPF2404 detectors exhibit a maximum, full-bandwidth RMS output noise of 0.4 mV. From equation (2.21), the full-bandwidth SNR is about 225 or 47 dB. From information theory, we know that the effective RMS quantization noise of an n-bit ADC is given by

$$SNR_{RMS} = (6.02 \cdot n + 1.76)dB \tag{2.22}$$

where n is the number of bits of the ADC. Thus, the 47 dB figure given above is equivalent to the RMS quantization noise of a 7-bit converter.

This worst-case value holds for the full, unfiltered detector's bandwidth. The high bandwidth of these devices comes from the fact that they are optimized for telecommunications. Thus, the noise level can be lowered by reducing the unnecessarily high bandwidth. As indicated previously, the required signal bandwidth is 20 kHz. A 1 MHz system bandwidth is therefore more than adequate. Assuming a flat noise distribution[15] and a 50 MHz bandwidth (OPF is 20 ns rise time), we find that the detector bandwidth is at least 50 MHz. Since the noise is proportional to the square root of the bandwidth, filtering out with a 1MHz brickwall-equivalent filter cut-off frequency would theoretically result in a seven-fold noise level reduction. This would bring the SNR up to 7 x 225 or 1600 (50 μV noise). This is equivalent to 64 dB or slightly more than 10 bits.

The achievable SNR is somewhat more difficult to evaluate when there is no integrated transimpedance amplifier. In this case, all of the noise sources must be computed individually. First, the dark current must be evaluated. Since the required bandwidth is low, there is no need to bias the detector.[16] Hence we can consider the dark current noise I_{DN} to be negligible. When the DC component of the signal is of interest, the dark current itself must also be considered a noise source since there is no way to distinguish it from the signal-induced current. The only way out of this is, again, synchronous detection.

The next contributor to noise is the signal or photon shot noise. Since the same equation obtains for both dark current and photon shot noise, they can be treated together. The total photodiode shot noise is then defined as

$$I_{PN} = \sqrt{2 \cdot q \cdot (I_S + I_D) \cdot \Delta f} \tag{2.23}$$

where q is the electronic charge, Δf is the electrical bandwidth considered, I_D is the dark current (set to zero) and I_S is the signal current. Note that the above equation sets a physical lower limit to the system noise. Hence a perfect detection system will always carry a noise level equivalent to I_{PN}. With a responsivity of 0.5 A/W and an optical power of 18 μW, I_S is 9 μA. For a 1 MHz bandwidth, this translates into a 1.7 nA RMS noise.

The next noise contributors are the feedback and photodiode shunt resistance Johnson noise. The current equivalent Johnson noise associated to a resistor is given by

$$I_{RN} = \sqrt{\frac{(4 \cdot K \cdot T \cdot \Delta f)}{R}} \tag{2.24}$$

where K is Boltzman's constant, T the temperature in Kelvin and R the resistance value in ohms. At room temperature and for a typical value of R =100 kΩ, I_{RN} is 0.4 nA. The noise associated with the shunt resistance of the photodiode is neglected since the resistance is much higher than the feedback resistor.

The final contribution to noise is the amplifier noise itself. Operational amplifiers have inherent current and voltage noises as well as input offset currents and voltages, and both types of contributions will be treated separately.

[15] The noise power spectrum is not provided for Optek's products but this assertion is verified for Agilent's HFBR-14x6 series.
[16] This will nonetheless lower the responsivity.

The total current and voltage noise contributions referred as an input current noise are independent and must be rss-summed. The equivalent current input noise, defined below, is a first-order approximation and is valid at low frequencies (neglecting the input capacitance effects).[17]

$$I_{AN} = \sqrt{\left({I_A}^2 + \left(\frac{V_A}{R_F} \right)^2 \right) \cdot \Delta f} \tag{2.25}$$

where I_{AN} is the amplifier noise referred to the input, I_A the amplifier's current noise, and V_A the amplifier's voltage noise.

Analog Device AD549 has an input voltage noise density of 90 nV·Hz$^{-1/2}$ and an input current density of 0.22 fA·Hz$^{-1/2}$. To these, the low frequency (below 1/f cutoff frequency) RMS noise sources must be added. These are 4 μV pk-pk (0.28 μV rms) and 0.5 *f*A RMS. Thus, the total input noise due to the AD549, referred as a current noise at the input, is

$$\begin{aligned} I_{AN_{TOT}} &= \sqrt{(0.5\mathrm{fA})^2 + \left(\frac{0.28\mu\mathrm{V}}{100\mathrm{k}\Omega} \right)^2 + \sqrt{\left(0.22fA^2 + \left(\frac{90\mathrm{nV}}{100\mathrm{k}\Omega} \right)^2 \right) \cdot 1 \times 10^6 \mathrm{Hz}}} \\ &= 0.9\mathrm{nA} \end{aligned} \tag{2.26}$$

Note from the above result that the dominant contributors to noise are the terms under the square root sign. Hence, reducing the bandwidth would help reduce the noise. All noise sources are uncorrelated and must be rss-summed. Hence

$$I_{NTOT} = \sqrt{{I_{AN_{TOT}}}^2 + {I_{RN}}^2 + {I_{PN}}^2} \tag{2.27}$$

The above equation finally yields a current-equivalent noise of 2 nA at the input of the amplifier. This yields an SNR of about 4500. Note that this value is not far away from the value computed for the built-in transimpedance amplifier devices. It is also important to note that the latter value is somewhat optimistic as the computation neglected leakage currents and pick-up noise that inevitably show up in any real implementation. Thus, the values calculated for the transimpedance-equipped detectors form a more realistic approximation of reality.

Strictly speaking, the input offset voltage and bias currents are systematic errors rather than noise sources *per se*. However, unless special processing means are used, their contribution is undistinguishable from the signal and they must be considered as a bandwidth-independent noise source.

For the AD549, the maximum quoted input bias current I_b and offset voltages V_{os} are 1 mV and 250 fA, respectively These contributions must also be summed according to an rss rule. Thus, we can write

$$e_{n_{out}} = \sqrt{\left(I_{NTOT} R_F \right)^2 + (I_b R_F)^2 + {V^2}_{os}} \tag{2.28}$$

Summed together, the two contributions add up to 1.05 mV of noise at the output for a 900 mV signal. The final SNR ratio is then 850 or 9.4 bits.

[17] An excellent discussion of photodiode noise sources can be found in EDN magazine, October 29, 1987 issue, pp. 205-220.

Note that the dominant factors are the input offset voltage and bias currents. Hence, filtering will not help and only a stronger signal can increase the SNR. The dominant term is the input offset voltage, which can be trimmed using offset nulling techniques. This can effectively bring the offset down to 0.25 mV. Even with that value, the input offset voltage still dominates the noise. Another option is to increase the feedback resistance value. Since this value does not affect the input offset voltage, increasing it results in a greater SNR.

For example, a five-fold increase of R_F would make the offset and noise contributions roughly equal. This would result in an optimal SNR of slightly less than 4000 for a signal swing of about 4.5 V, enough to operate at 12 bits or so. There is, however, a limit to increasing the feedback resistor brought up by other amplifier characteristics, the large-signal bandwidth being one of them. Furthermore, a larger resistance brings frequency response issues as a result of the transfer function poles created by the input capacitance, the feedback resistance and the parasitic capacitance in parallel with the feedback resistor.

Another alternative is to look for a different combination of operational amplifier characteristics. For example, one could tolerate a slightly higher noise current in return for a lower input offset voltage. The AD743, AD8510/8512, AD8610/8620 and AD8605/8606/8608 families of amplifiers constitute interesting alternatives whose sets of characteristics are better tailored to the application. Other amplifiers, not surveyed, may also constitute sensible solutions.

Table 2: Error Budget for Various Detector/Feedback Resistor Combinations

Contribution	AD549	AD8605		
Source	100kΩ resistor	100kΩ resistor	250 kΩ resistor	500 kΩ resistor
I_{PN}	1.70 nA	1.70 nA	1.70 nA	1.70 nA
I_{RN}	0.40 nA	0.40 nA	0.25 nA	0.18 nA
I_{AN}	0.90 nA	0.12 nA	0.05 nA	0.03 nA
I_{ANTOT}	0.91 nA	0.125 nA	0.052 nA	0.035 nA
I_{NTOT}	1.96 nA	1.75 nA	1.72 nA	1.71 nA
$I_{NTOT}R_F$	0.196 mV	0.175 mV	0.429 mV	0.855 mV
I_bR_F	0.001 mV	0.005 mV	0.013 mV	0.025 mV
V_{os}	1.000 mV	0.300 mV	0.300 mV	0.300 mV
V_{NOUT}	1.019 mV	0.347 mV	0.524 mV	0.906 mV
Signal	900 mV	900 mV	2.25 V	4.5 V
SNR	883	2594	4290	4967

Table 2 summarizes the results computed for various amplifier/resistor combinations. The AD8605/100 kΩ resistor combination is superior to the OP549 combination, but the offset voltage still dominates. Increasing the feedback resistance value to 500 kΩ makes the photodiode shot noise the dominant noise source. Based on the trend observed in Table 2, larger resistors would yield a proportionally decreasing improvement. The 500 kΩ resistor is probably already larger than the optimal value as a large 4.5 V signal is likely to reduce the amplifier bandwidth. Moreover, the large resistor is more susceptible of creating poles with the input capacitance. It is also important to note that the members of the AD860X family of amplifiers are single supply amplifiers. As a result, they *cannot* produce a voltage lower than the ground level plus +20 or 40 mV. This somewhat limits their usefulness in one end of the range. The AD851X family is a faster family that offers a very similar level of noise performance and carries a higher price tag in a dual supply configuration. It is also worth noting that the error budget presented in

Table 2 accounts for neither the feedback resistance temperature coefficient nor the amplifier characteristics drift with temperature.

In summary, an AD8605 (or its AD8612 counterpart) with a 500 kΩ resistor can produce a 4.5 V signal with an SNR close to 5000. This value neither takes into account thermal drift effects nor resistor temperature coefficient. The achievable SNR is adequate for a 12-bit ADC. In this case, the quantization noise of the ADC itself becomes the dominant noise source.

Having identified a suitable solution for the current-to-voltage amplification stage, we can now focus on the realization of the complete signal processing function. As identified in section 2.3, the function to be realized is

$$P = m \cdot \frac{(T_A - T_B)}{(T_A + T_B)} \tag{2.29}$$

where T_A and T_B stand for the signals of channels A and B, respectively. In practice, the simulations indicate that the equation should rather take the form of

$$y = mx + b \tag{2.30}$$

x being equal to the rightmost term in T_A and T_B of equation (2.29) where the offset term b stems from diffraction effects. Hence, the actual function to be realized is

$$\begin{aligned} P &= \left[m \cdot \frac{(T_A - T_B)}{(T_A + T_B)} \right] + b \quad (\text{form } 1) \\ &\quad or \\ P &= m \cdot \left[\frac{(T_A - T_B)}{(T_A + T_B)} + b' \right] \quad (\text{form } 2) \end{aligned} \tag{2.31}$$

The T_A-T_B term is proportional to the pressure applied on the sensor, while division by T_A+T_B — nominally a constant value — is solely used to correct for source and fibre transmission fluctuations so that the T_A-T_B term always produces the same response to a given stimulus. Note that the noise contributions of T_A and T_B must be considered independent since the noise sources (photon shot noise and amplifier errors) are all independent. Hence, their noise contribution should be added in an rss fashion. The differential approach therefore offers superior noise performance since it effectively doubles the signal span while the noise only increases by $\sqrt{2}$. Another way of seeing this is to realize that there is always at least one ‘strong’ signal: when channel A (B) gives an output close to zero, channel B (A) is near its maximum output and subtraction yields a strong signal. When both channels are in their midrange, two moderately strong signals are subtracted and the SNR remains good although the output is close to zero.

The function of equation (2.29) can be realized in one of two ways. First, the function can be realized integrally. Alternatively, the numerator part of the equation can be realized in a normal fashion, leaving the denominator out. Division by the denominator is then replaced by a feedback loop acting on the intensity of the light source itself.

The first implementation can be realized with an analog multiplier such as the AD734. The AD734 is a general-purpose analog multiplier that can realize the following generalized function:

$$W = A_0\left[\frac{(x_1 - x_2)(y_1 - y_2)}{u_1 - u_2} - (z_1 - z_2)\right] \tag{2.32}$$

The function is achieved by setting $x_1 = u_1 = T_A$; $x_2 = -u_2 = T_B$; $(z_1 - z_2) = b$ and $(y_1 - y_2) = m$. Note that coefficient A_0 remains available for other purposes, such as temperature compensation (A_o could also be set to m, leaving temperature compensation to $y_1 - y_2$). This approach offers a complete solution since all computations can be achieved in an analog fashion, i.e. the output voltage can be scaled to obtain a direct pressure-to-voltage relationship. This technique, however, has a number of drawbacks. For one, setting $x_2 = -u_2$ implies that a very precise inverter is available. The actual division is also relatively imprecise although the denominator always remains a large value. Thirdly, the AD734 is a relatively expensive component.

The alternate solution makes use of a feedback loop to eliminate the term T_A+T_B by effectively making it a constant. This approach relies on either form 1 or 2 of equation (2.31). Form 1, however, is preferred as the offset term b is then independent of the gain m_F. The equation then simplifies to

$$\begin{aligned} P &= \left[\frac{m}{T_A + T_B} \cdot (T_A - T_B)\right] + b \\ &= \left[m_F \cdot (T_A - T_B)\right] + b \end{aligned} \tag{2.33}$$

where the term m_F is used to indicate that the gain is a dynamic frequency-dependent function.

The T_A-T_B part of the function is easily realized with a precision instrumentation amplifier while the remainder of the function is accomplished with a simple operational amplifier. In some cases, such as with the AD620, the offset b can also be added using a dedicated level-shifting input, thereby realizing the complete function with a single IC. By comparison with the first implementation, the latter is cheaper and offers a better SNR in light of the reduced number of analog functions to be implemented. The downside to this approach is that the gain m is now a function of the transfer function of the feedback loop used to stabilize T_A+T_B.

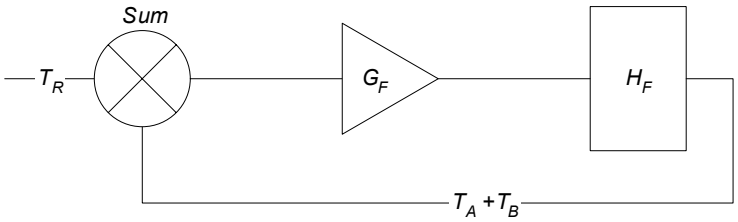

Figure 23: Feedback Loop Model

The feedback loop can de modeled as pictured in yielding the open transfer function

$$T_A + T_B = T_R \cdot \frac{G_F H_F}{G_F H_F + 1} \tag{2.34}$$

where G_F is the feedback loop gain, T_R is the command value that the feedback loop tries to maintain at the output, and H_F is the combined frequency response of the amplifier, LED and detector.

The above result can then be fed back into equation (2.33) to yield

$$\begin{aligned} P &= \left[m \cdot \frac{(G_F H_F + 1)}{T_R G_F H_F} (T_A - T_B) \right] + b \\ &= \left[k \cdot (1 + \frac{1}{G_F H_F})(T_A - T_B) \right] + b \end{aligned} \tag{2.35}$$

Thus, with the feedback approach, the indicated pressure P is a frequency-dependent function of all components present within the feedback loop. Note, however, that the frequency-dependent $G_F H_F$ term of equation (2.35) can be characterized fairly well to compensate for this undesirable behaviour. Moreover, given a large enough value of G_F, equation (2.35) degenerates into

$$\begin{aligned} P &= \lim_{G_F \to \infty} \left[k \cdot (1 + \frac{1}{G_F H_F})(T_A - T_B) \right] + b \\ &= \left[k \cdot (T_A - T_B) \right] + b \end{aligned} \tag{2.36}$$

with

$$k = \frac{m}{T_A + T_B}$$

In the previous section, it was established that a 500 kΩ resistor would give rise to a signal strength ranging from 0 to about 4.5 V. Since both channels are in opposite phase, subtracting these two signals yields a signal range of roughly ±5 V assuming a gain of +1. Moreover, the maximum common mode voltage of 2.5 V is reached when both channels are in the middle of their operating range.

Table 4 presents the error budget of the AD620 instrumentation amplifier. It is readily seen that the gain thermal drift is the dominant contributor for the AD620B. The SNR of the two combined stages is given in Table 3. Also note that the input voltage of the AD620B is limited to 5 V. While the instrumentation amplifier is the limiting factor, the total error always remains with 0.025% of full scale, which corresponds to an SNR of 72.8 dB or 11.8 bits. Consequently, a 12-bit ADC would be adequate under the conditions indicated in Table 4.

Table 3: Total System SNR

Condition	Transimpedance amplifier A	Transimpedance amplifier B	Instrumentation amplifier	Total	Error in % of FS
V_A = 4.5 V; V_B = 0 V	0.906 mV	0.315 mV	2.109 mV	2.317 mV	0.023%
V_A= V_B = 2.5 V	0.678 mV	0.678 mV	0.797 mV	1.247 mV	0.012%

Lastly, Figure 24 presents a preliminary version of the electronics diagram, complete with the feedback loop to maintain the LED output power at a constant level.

Table 4: AD620 Error Source Calculation

	AD620A			AD620B	
Parameter*	Value	V_{in} = 0V	V_{in} = 5V	Value	V_{in}= 5V
Absolute Accuracy at TA = 25°C					
Input Offset Voltage, µV	125 µV	125 µV	125 µV	50 µV	50 µV
Output Offset Voltage, µV	1000 µV	1000 µV	1000 µV	500 µV	500 µV
Input Offset Current, nA (in transim-pedance amplifier output impedance)	2 nA	0 µV	0 µV	1 nA	0 µV
CMR, dB (for 2.5 V CM voltage)	-73 dB	550 µV	550 µV	-80 dB	250 µV
Total Absolute Error (rss)		**1150 µV**	**1150 µV**		**561 µV**
Temperature Drift (from +25°C to + 60°C)					
Gain Drift, ppm/°C	10 ppm/°C	0 mV	1750 µV	10 ppm/°C	1750 µV
Input Offset Drift, µV/°C	1 µV/°C	35 µV	35 µV	0,6 µV/°C	21 µV
Output Offset Drift, µV/°C	15 µV/°C	525 µV	525 µV	7 µV/°C	245 µV
Total Drift Error (rss)		**526 µV**	**1827 µV**		**1767 µV**
Resolution					
Gain Error in ppm at G = 1	1000 ppm	0 µV	5000 µV	200 ppm	1000 µV
0.1–10 Hz Voltage noise, µV p-p	3 µV	3 µV	3 µV	3 µV	3 µV
Voltage noise density (1 MHz BW)	100 nV/$Hz^{-1/2}$	100 µV	100 µV	100 nV/$Hz^{-1/2}$	100 µV
Total Resolution Error (rss)		**100 µV**	**5001 µV**		**1005 µV**
Grand Total Error (rss)		**1269 µV**	**5447 µV**		**2109 µV**
Error in % of Full-scale Value (ppm)		**254**	**1089**		**421**
Equivalent SNR		**3940**	**918**		**2375**

* Worst-case parameter is used (min or max as applicable).

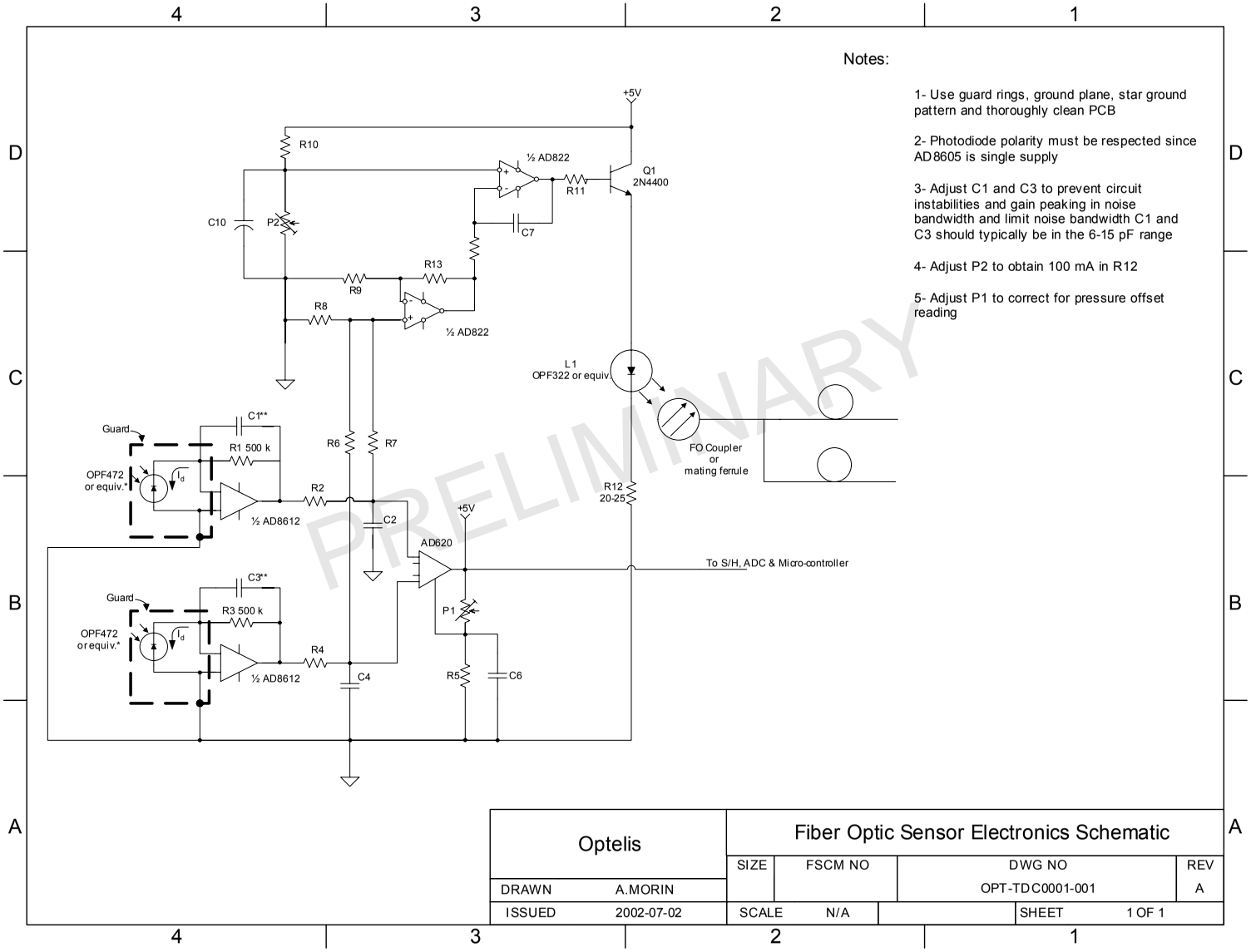

Figure 24: Preliminary Sensor Preliminary Electronics Diagram

3 MECHANICAL DESIGN

The sensor is composed of six major components as indicated in Figure 25. The base of the sensor is machined out of Inconel 718. This material was selected for its high resistance to high temperatures and for its generalized availability. The sensor head is machined out of an Inconel 718 rod and a stainless steel washer is used to make an airtight joint between the base and the head of the sensor.

The so-called optical base is made out of Kovar and is welded to the sensor head. The Kovar material was selected for the similarity of its thermal coefficient of expansion (CTE) to glass CTE. The modulation grids are also made out of Kovar. The reference grid is spot-welded to the optical base while the modulating grid is attached by the same means to the diaphragm's central pinion. Lastly, the lenses are held in place in the optical base through the lens holder. Detailed drawings are provided in Appendix B.

3.1 Finite Element Analysis

This section and the following analyze the thermal transient behaviour of the sensor under normal pressure fluctuations.

3.1.1 Finite Element Model

The finite element model shown in Figure 25 and Figure 26 is used to determine the relative displacement of the modulating and reference grids from a cold start-up situation (20°C) up to normal operating regime (450°C). This modeling also accounts for internal pressure fluctuations of 20 MPa (200 atm). The sensor base, the optical base, the optical head and the washer are modeled as solid 2D axisymetric elements. The modulating grid is modeled as a solid 3D element.

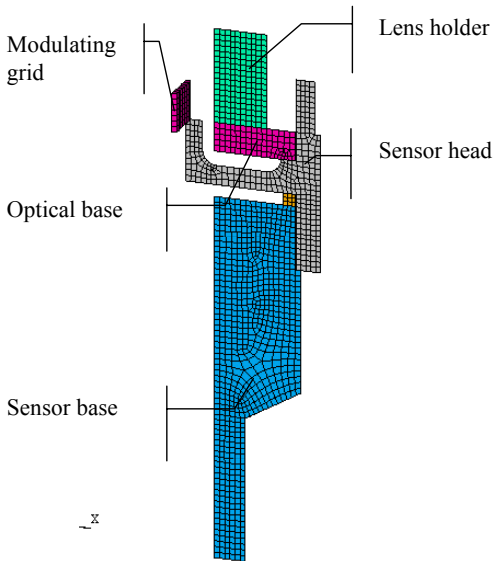

Figure 25: Finite Element Model with Normal (20 MPa) Pressure Fluctuations

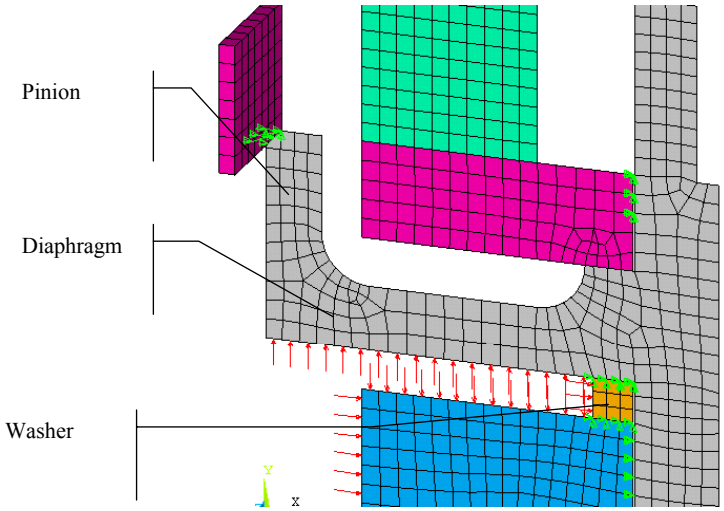

Figure 26: Finite Element Model Detail

3.1.2 Materials Properties

Four different materials are used. Inconel 718 is used for the sensor base and sensor head while Stainless steel 304 is used for the washer. Kovar is used for the lower part of the optical base and the modulating grid. Finally, a combination of 40% Kovar and 60% Pyrex glass is used for the lens holders. The thermal and mechanical properties of these materials are given in Table 5.[18,19] In this table, *E* stands for Young's Modulus, α is the thermal coefficient of expansion, C_p is the specific heat, *K* denotes the thermal coefficient of conduction the temperature, and ρ stands for the density.

Table 5: Materials Properties Used in Finite Element Model

Material	Temperature (°C)	E (Pa)	α (m/m-°C)	ρ (kg/m^3)	K (W/m-°C)	C_p (J/kg·°C)
Inconel 718	20	219×10^9	12.83×10^{-6}	8190	14.50	487.8
(Head & base)	450	192×10^9	14.58×10^{-6}	8190	20.71	570.2
Stainless steel	20	200×10^9	9.43×10^{-6}	7800	22.61	465.7
(Washer)	450	159×10^9	11.50×10^{-6}	7800	29.08	635.8
Kovar	20	207×10^9	5.10×10^{-6}	8360	17.00	460.0
(Optical base)	450	166×10^9	6.20×10^{-6}	8360	23.80	552.0
40% Kovar/	20	125×10^9	4.02×10^{-6}	4680	7.64	694.0
60% Glass	450	100×10^9	4.86×10^{-6}	4680	10.70	832.8

[18] ASME Code Subsection NA
[19] http://www.matweb.com/SpecificMaterial.asp?bassnum=NINC34&group=General

3.1.3 Conditions on the Degrees of Freedom Between Components

The nodes at the interfaces between components, the sensor base, the sensor head and the washer have their temperature and displacement variables coupled. The partial penetration welding between the optical base and the optical head is simulated by coupling the temperature and displacement degrees of freedom of the weld nodes to the nodes of the optical base's upper half.

3.1.4 Model Node Conditions

All nodes of the lower half of the base are locked along the vertical axis. All modulating grid nodes along the symmetry planes $x = 0$ and $z = 0$ have imposed symmetry.

3.1.5 Initial and Loading Conditions

The models are run using the following series of events. The initial internal temperature is first set to 20°C and internal pressure is set to atmospheric pressure. Then, all nodes in contact with the combustion gases are submitted to a 450°C temperature. This generates a quasi-instantaneous forced convection state where h = 285 W/m^2/°C (see Appendix E for calculation details). The same nodes are also exposed to a 20 MPa pressure in order to evaluate the structural effects of pressure on the design.

3.1.6 Results

3.1.6.1 Modulating Grid Displacement with Respect to Reference Grid

Table 6 summarizes the transient response from $t = 0$ up to the steady-state regime ($t = \infty$). The first line provides results for the case when a high temperature but no pressure is applied, while the second column presents the results when both temperature and pressure are applied. The third line isolates the contribution of the pressure-induced displacement. Note that for all practical purposes, the steady-state regime ($t = \infty$) is considered achieved after a 20-minute period.

Table 6: Position of Modulating Grid with Respect to Reference Grid as a Function of Time

	$t = 0$	$t = 1$ s	$t = 10$ s	$t = 100$ s	$t = 1000$ s	$t = \infty$
0 MPa	0 µm	-0.21 µm	1.68 µm	-2.71 µm	-18.22 µm	-20.25 µm
20 MPa	23.55 µm	23.40 µm	25.59 µm	22.12 µm	8.45 µm	6.69 µm
Δ P contribution	23.55 µm	23.61 µm	23.91 µm	24.83 µm	26.67 µm	26.94 µm

Figure 27 illustrates the temperature distribution and the displacements after 100 s. The leftmost figure illustrates the temperature distribution; the middle figure plots displacements for a no-pressure condition; and the rightmost graph presents the same information when a 20 MPA pressure is applied.

3.1.6.2 Fatigue Analysis Due to Internal Pressure Cycling

It is a requirement that the sensor be designed to last for at least five years. This calculation is based on an average twelve hours a day of operation. At seven pressure cycles per second (420 rpm), the total number of pressure cycles endured by the sensor over its lifetime is $N_p = 5.52 \times 10^8$ or roughly half a billion cycles which, for all practical purposes, can be considered infinite.

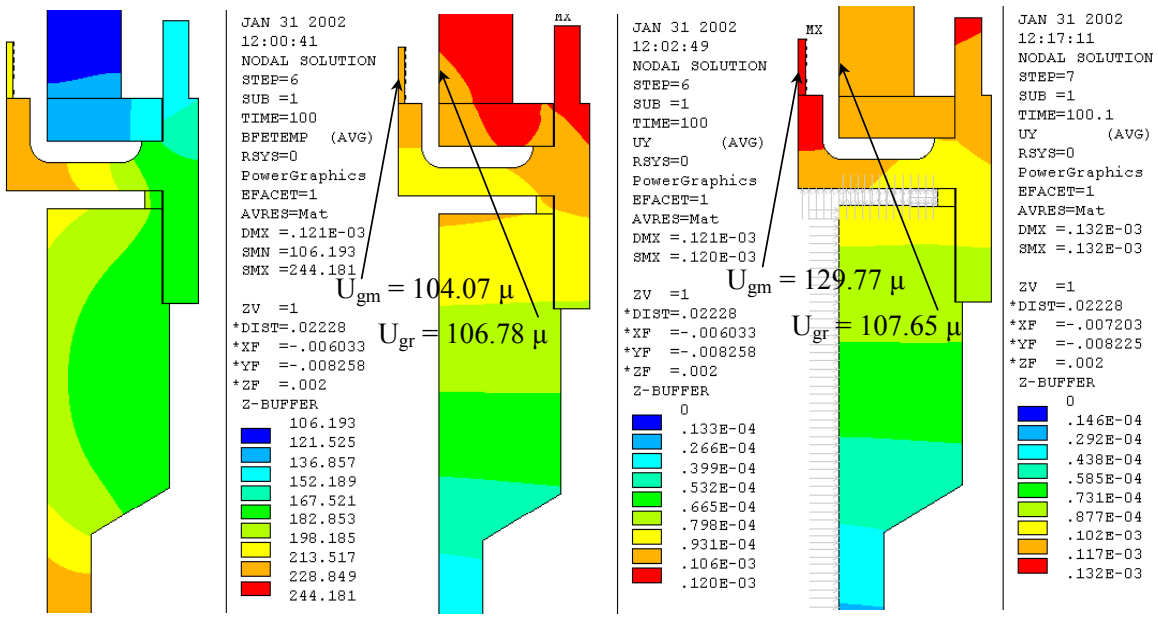

Figure 27: Temperature Distribution and Grid Displacement after 100 Seconds

In such a case, the allowable stress fluctuation is the limit of endurance of the material. According to Mechanical Engineering Design, Shigley, McGraw-Hill, the limit of endurance of a small, machined component is about 0.3 to 0.4 of Su_{min} where Su_{min} is the material's ultimate stress limit. For Inconel, this limit is 1100 MPa at 450°C. The limit of endurance for this material is therefore 330 MPa.

In the design under investigation, the maximum stress fluctuation generated by 20 MPa cycles is 285 MPa. This maximum value occurs at the radius of the pinion's fillet as shown in Figure 28. Since this value is lower than the 330 MPa limit, the diaphragm should have infinite endurance.

3.1.6.3 Thermal Stress

The number of cold starts N_d experienced by the sensor over its lifetime is estimated at once a day, for a total of 1825 over the lifetime. This value can be considered negligible for metals. The maximum thermal stress is then the sum of the allowable tension and compression stress. Thus, the allowable $\Delta\sigma = 2S_y$ where S_y is the flow stress. The flow stress is S_y is 1020 MPa for Inconel and 275 MPa for Kovar. Hence, the allowable thermal stress is 2040 MPa for Inconel and 550 MPa for Kovar. The maximum thermally induced stresses computed that occur near the weld between the head and the optical base are 812 MPA and 600 MPa for Inconel and Kovar, respectively. Therefore, the Inconel part should never experience any plastic deformation whereas the Kovar could experience some plastic deformation.

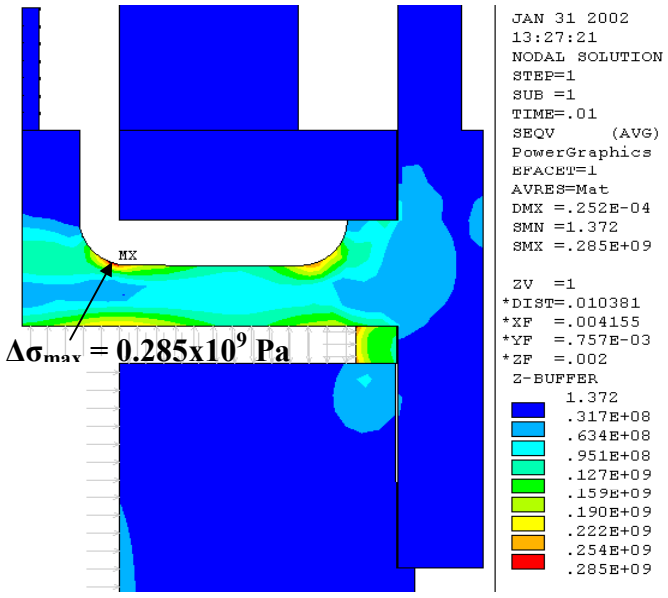

Figure 28: Von-Mises Pressure-Induced Stress

Since this fluctuation occurs only 1800 times over the sensor's lifetime and since the plastic limit is only slightly exceeded, the probability of the Kovar base cracking due to fatigue is slight.

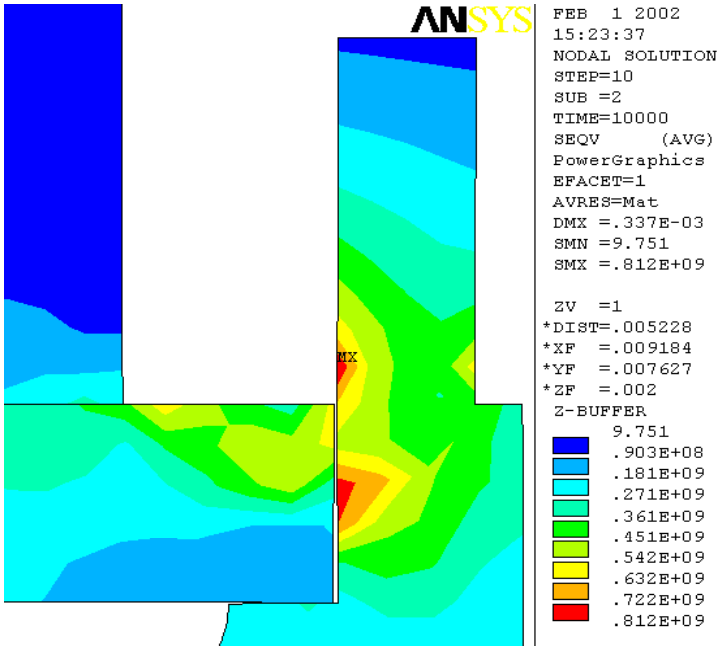

Figure 29: Thermally Induced Stress at the Weld Between the Inconel Head and the Kovar Base

This fatigue problem arises from the large CTE difference between the Kovar and Inconel. To further reduce the risk would require selecting a different combination of materials.

3.2 Natural Frequencies Analysis

3.2.1 Natural Frequency of the Modulating Grid Holder

The left-hand side of Figure 30 shows the model used to determine the natural frequencies of the holder of the modulating grid. All nodes are modeled with a 3-D shell representation with six degrees of freedom. The properties of Kovar at 450ºC are used in the model. All nodes on a 3.5 mm wide length are clamped. The right-hand side of the figure illustrates the lowest-frequency vibration mode. The natural frequency for that mode is 31 544 Hz, which is well above the established lower limit of 20 kHz.

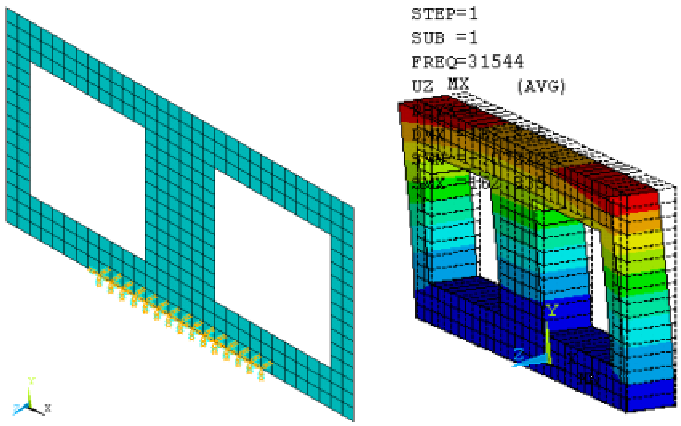

Figure 30: Modal Analysis of the Modulating Grid

3.2.1.1 Natural Vibration Modes of the Modulating Grid

Aside from the grid as a whole, each band of the grid also has vibration modes. One band of the grid was modeled as shown in Figure 31. The model, again based on a 3-D shell representation, corresponds to a Kovar band 2.5 mm long and 30 μm thick. The lowest natural frequency vibrating mode observed is 22 433 Hz, which is slightly above the minimum 20 kHz. As a result, the design meets the requirement provided the bands are at least 30 μm thick.

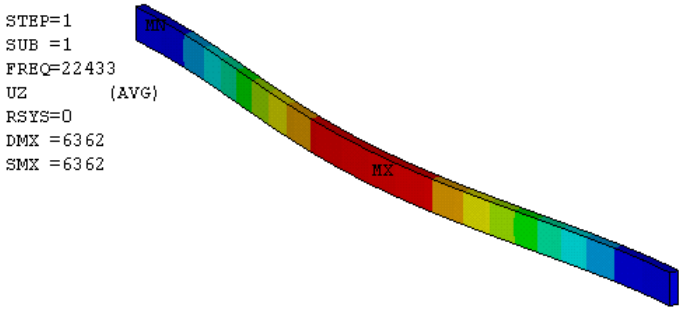

Figure 31: First Natural Vibration Mode of One of the Bands of the Modulating Grid

3.2.1.2 Natural Frequencies of the Sensor Assembly

Figure 32 depicts the finite element axisymetric model used to determine the natural resonant frequencies of the sensor assembly. The model used is identical to the one used in the thermal analysis assembly and the properties of Kovar at 450°C are used. The first resonant mode appears at 18.52 kHz and is illustrated in Figure 32b. Figure 32c illustrates that thickening the base of sensor would raise the first natural frequency above the 20 kHz mark. Finally, Figure 32d shows the second resonance of the sensor.

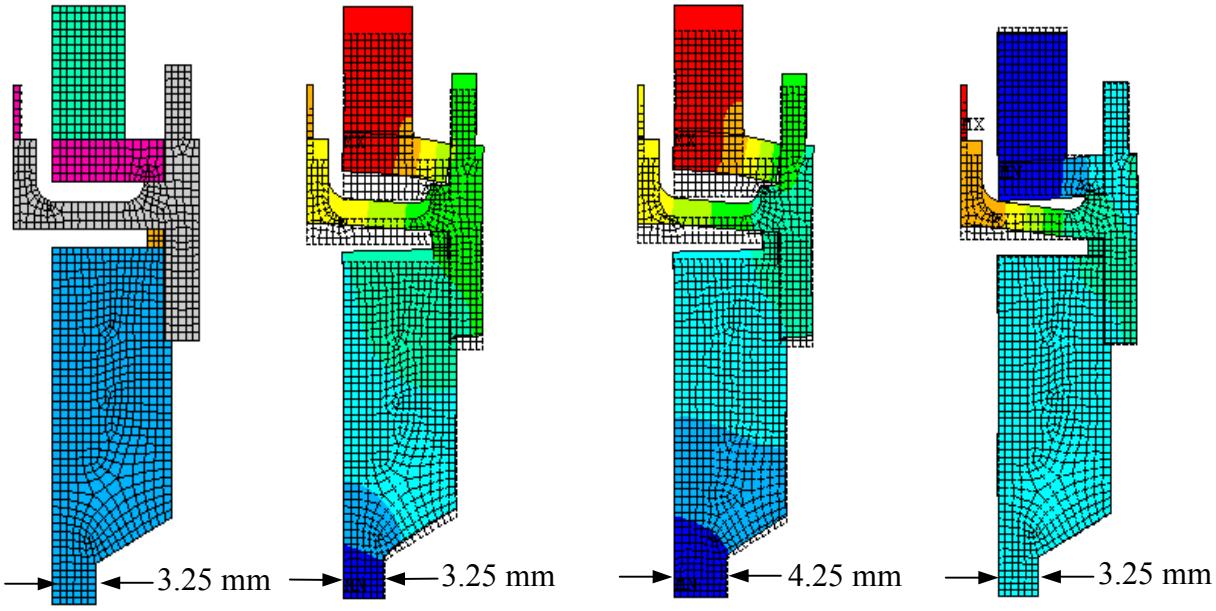

Figure 32: Natural Frequencies of the Sensor

3.3 Manufacturing and Assembly

3.3.1 Manufacturing

With the exception of optical components and grids, all components are manufactured by machining.

3.3.2 Assembly

The base of the sensor is tightened against the sensor head. As per the detailed calculations shown in Appendix D, the applied torque should be about 90 to 120 N-m in order to generate an initial pressure 25 000 N on the washer.

The optical base is welded around the entire periphery of the sensor head by partial penetration weld. Lastly, the grids – pre-aligned and assembled in their respective holders – are spot-welded to the pinion and the optical base.

3.4 Design Limitations and Proposed Modifications

Two problems were identified during the thermal simulations. First, the large difference between the coefficients of thermal expansion of the Kovar and Inconel results in fatigue levels slightly higher than the general design limits at the welded joint between the base and the optical head. A potential solution would involve the replacement of Inconel by a high-strength steel material. This steel should have a flow stress of at least 950 MPa at 450°C and a coefficient of thermal expansion comparable to stainless steel. A 17% Cr-5% Ni steel with precipitation treatment would be a fine candidate.

The second problem encountered is related to the frequency of the first resonance mode of the sensor. To circumvent that problem, it is suggested that the thickness of the base be increased from the current design value of 3.25 mm to 4.25 mm.

4 ASSEMBLY AND FABRICATION CONSIDERATIONS

In order to get an idea of the sensor's economic viability, quotations were obtained from Usinage Scientifique Démo (U.S.D.). This supplier has carried out work for TDC and is used to work on small, tight tolerance parts. Moreover, U.S.D. does subcontract for the portion of the work for which it lacks in-house capabilities. Out of the dozen or so subcontractors contacted by U.S.D., only three provided a quotation.

Note that the *sensor base* and *sensor head* parts, originally intended to be manufactured out of SS 637 material, were finally quoted with Inconel 718 due to the material availability. This material has excellent mechanical properties at high temperature and offers good resistance to corrosion. It is widely used in aeronautics, notably for turbo engine fins. This material exhibits excellent welding properties, but its compatibility in this respect with Kovar is unknown and difficult to anticipate based on the material's other properties. It is consequently recommended that a Kovar to Inconel welding test be conducted before costly machining is undertaken.

Micro-machining of the grids was left to the customer. A number of solutions were envisaged, including electro-chemical deposition (notably chromium, which can be etched away with a laser abrasion system such at the table-top Acculaze™), electrochemical abrasion, laser machining, etc.

4.1 Manufacturing Costs

According to a quotation obtained from U.S.D., machining and assembly for a first prototype is estimated at CAD $7100. This price is exclusive of taxes and optical components. For a 20-unit quantity, prices drop to CAD $1024 per unit. It is believed that this could drop by another 30% for a 2000-unit run, to bring total machining and assembly cost to CAD $710. Quotations for machined components are presented in Appendix C.

Further, no supplier was ready to provide a firm quotation for a 2000-unit quantity. Nonetheless, one could reasonably expect a further 30% reduction of the unit price to bring the cost of mechanical components to CAD $710 per unit.

Labour-related costs are more difficult to assess and are somewhat of lesser importance in view of a very limited production. Indeed, at this stage of product development, the tools required to automate the production process have usually not been fully developed, the process itself is not completely characterized and the assembly line personnel not familiar with the product.

Nonetheless, it is believed that a sensor could be assembled within two to four hours by relatively untrained personnel in a limited-run production environment.

4.2 Other Considerations

This estimate includes spot-welding operations, splicing and cabling, and assumes that critical operations can be completed without rework (high yield). There are a few operations in the manufacturing process that can affect the overall yield.

Table 7: Preliminary Bill of Material (small production run)

Description	P/N or suggested manufacturer	Unit (CAD)	Qty	Total (CAD)	Comments
Optics	Pricing for small quantities				
LED	OPF342A	29.80	1	29.80	19.87 USD (Pioneer)
Si PIN Photodiode	OPF472A	22.89	2	45.78	15.26 USD (Pioneer)
Sapphire lenses	Doric Lenses	15.00	4	60.00	Incl. mat'l and machining in volume
1x2 coupler	FIS	75.00	1	75.00	49.00 USD
100/140 μm gold-coated fibre	Silica Physics or Fiberguide	24.00	2	48.00	Per metre unit cost
100/140 μm polyimide-coated fibre	CeramOptec or equivalent	2.25	8	18.00	Per metre unit cost
FO connectors	FIS ST F1-0067	5.98	3	17.94	3.95 USD
Subtotal				**294.52**	
Electronics	Pricing for small quantities				
Dual Op Amp	AD822	6.83	1	5.15	4.55 USD (Pioneer)
Dual Op Amp	AD8612	9.22	1	9.22	6.15 USD (Pioneer)
Op Amp	AD620	8.88	1	8.88	5.92 USD (Pioneer)
Resistors	1% metal-film	0.05	20	1.00	
Potentiometers	Bourns 3352 Series	1.78	2	3.56	Cermet type
Transistor	2N4400	0.12	1	0.12	
Capacitors	Ceramic/electrolytic	0.20	15	3.00	
ADC	AD7895	14.10	1	14.10	9.40 USD;12-its
Micro-controller & peripherals	—		1	15.00	Estimate
Electrical connectors	—	—	—	4.00	Estimate
Pwr reg. ass'y	—	—	1	4.00	Estimate
Bare board	—	—	1	5.00	Estimate
Miscellaneous	—	—	—	5.00	
Subtotal				**77.03**	
Machined Parts	Pricing based on 20-units purchase from U.S.D.				
Optical base	OPS-OB-01	168.81	1	168.81	
Sealing washer	OPS-SW-01	17.17	1	17.17	
Modulator grid holder	OPS-MG-01	129.55	1	129.55	
Reference grid holder	OPS-RG-01	138.37	1	138.37	
Sensor head	OPS-SH-01	155.90	1	155.90	
Sensor base	OPS-SB-01	185.92	1	185.92	
Emitter lens cap	OPS-ELC-01	52.84	1	52.84	
Ferrule holder	OPS-FH-01	53.37	4	213.48	
Receiver lens cap	OPS-RLC-01	130.94	1	130.94	
Modulator grids	No quote obtained				
Subtotal				**1024.34**	
Miscellaneous					
Electronics encl.	—	—	1	8.00	Estimate
Cable sheath	—	2.00/m	2.5 m	5.00	Estimate; per metre
Misc. H/W (grommets, screws, posts)	—	—	—	5.00	Estimate
Subtotal				**18.00**	
Total				**1413.89**	

Gold-coated to polyamide-coated fibre fusion splice is one such operation but the risks associated with this operation can be mitigated by testing the splices prior to assembly. Assembly and alignment of the grids to their holders is another one that can also be mitigated with proper tooling and trained personnel.

The third area concerns the initial relative alignment of the grids with respect to each other. This step cannot be mitigated before the final assembly operations and relies solely on manufacturing tolerances. While not detrimental in itself, misalignment results in a shift of the operating point of the sensor. As was shown in section 2.3.1, the linearity of the sensor is degraded in the operating regions where the grids are perfectly aligned or perfectly out of phase. Consequently, there is a preferred no-load alignment that optimizes the sensor linearity over the pressure range. Given the sensor construction, this alignment is only a function of the manufacturing tolerances. Further, the alignment can only be verified once the sensor is fully assembled. Thus, manufacturing tolerances and final assembly affect the sensor's linearity and consequently, the yield.

The grids themselves constitute yet another area of concern. At the time of writing, the exact grid fabrication method had not been definitively selected by the customer. As such, grid manufacturing yield is unknown and constitutes a major risk factor.

4.3 Cost Reduction Opportunities

Considering material costs only, the per-unit cost for small production run is about CAD $1400.00, exclusive of the grids themselves, which exceeds the targeted selling price. Machined parts alone represent more than 70% of that amount, without even taking into account the cost of the grids themselves or the assembly. Cost reductions are possible though, even for low volumes. Examples of cost reduction areas include replacing the coupler, minimizing use of Au-coated fibre, better selection of source and detectors, better electronics components selection, general design optimization, etc.

5 DEVELOPMENT SCHEDULE

The development schedule until product release for manufacturing is provided in Figure 33. The schedule is divided into three main phases: concept validation, prototyping and pre-production. Formal design reviews, such as DDR and CDR, are interspersed in the schedule as required.

The complete development cycle, from concept validation to production release, spans over close to one year, owing mostly to design iterations, components procurement and machining lead times. The level of effort is estimated at about CAD $200 K to $250 K, including labour, equipment and a first production run.

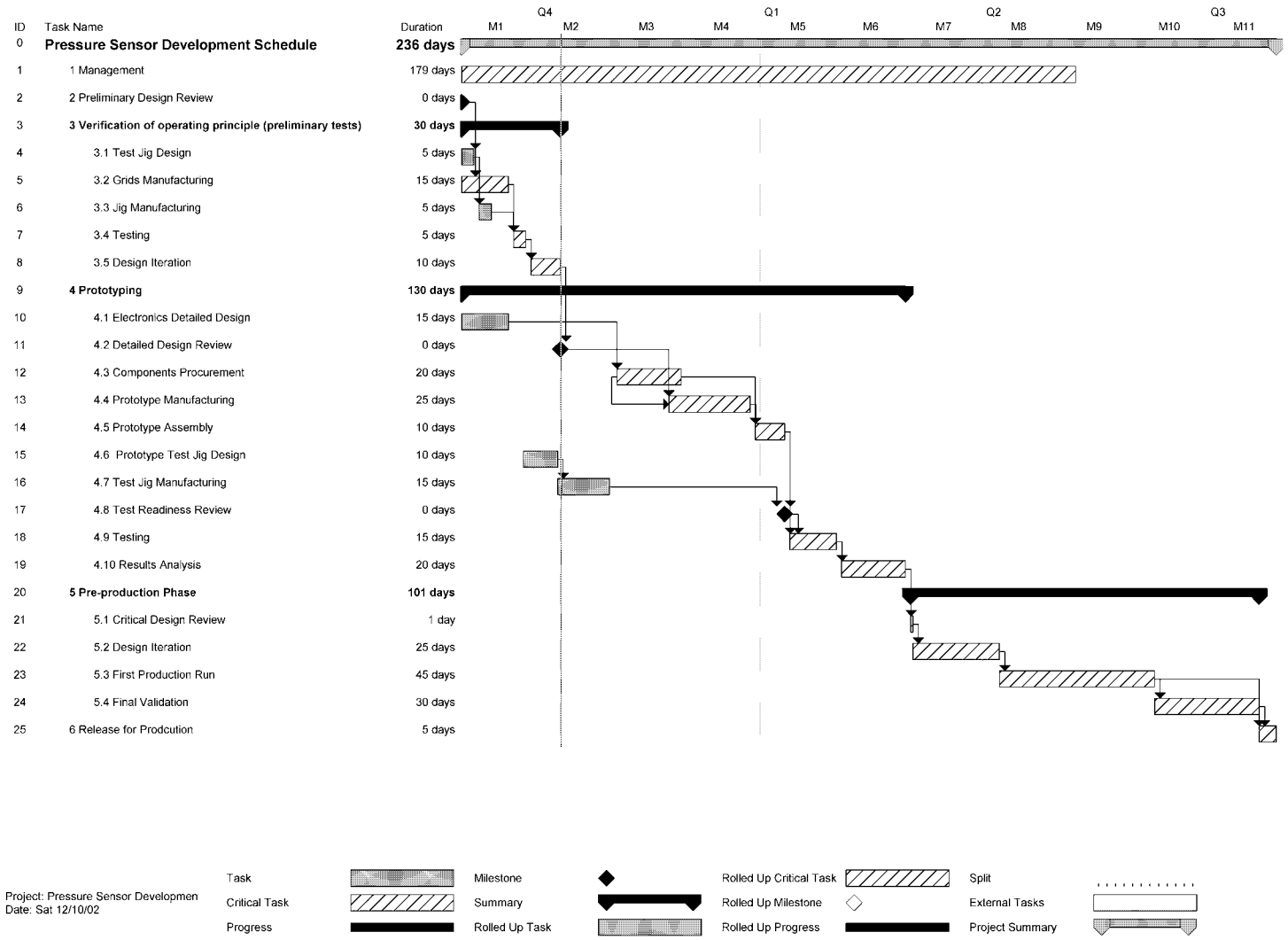

Figure 33: Proposed Sensor Development Schedule

6 CONCLUSIONS AND RECOMMENDATIONS

As stated in chapter 1, the first objective of this project was to assess the technical and economical viability of a fibre-optic pressure sensor concept developed by the Transportation Development Centre that was initiated to answer the unique needs of diesel engine in-line combustion efficiency monitoring. The second objective was to improve on the original design to meet the accuracy, longevity, cost and performance objectives.

The design was analyzed with a specific focus on manufacturability and performance issues. The analysis of the proposed design revealed a number of concerns, including the moving grid mechanism, fibre routing and, from a more general point of view, the mechanical design complexity.

The cantilevered beam design originally imagined as a folded metal sheet was deemed too difficult to manufacture in light of the tolerances demanded by the application. Finite element analysis performed on this component also revealed that there were many resonant modes lower than the minimum 20 kHz frequency.

The tight bends of the optical fibres were also found to be an important limiting factor of the design as the manufacturers' quoted fibre minimum bend radii exceeded the allowable space. The required heat-tolerant protective coating further exacerbated this fact. Accommodating the two fibre bends required that the fibre exit the sensor perpendicular to its main axis. Unfortunately, this solution leads to an unacceptable sensor footprint.

The method envisaged to attach and maintain the optical fibres in place was also scrutinized and found ineffective in view of the long lifetime required. However, the compensation scheme for optical losses, optical source instabilities and drift was deemed useful yet perfectible as second-order effects could not be totally eliminated. More generally, the mechanical design was found complex in terms of component fabrication, sensor assembly, and cost, and required accurate welding in tight spaces.

The revised implementation, retaining the valuable ideas from the original design, addresses most of these concerns. With the new design, the natural frequencies are now very close to the required values, the optical fibres are held in place in a simple way, and they are routed without bends. The number of mechanical components has also been significantly reduced. Finally, the cantilevered beam design has been replaced by a simpler mechanism.

While the design of the modulating grids was substantially improved over the course of this project, this issue nonetheless stands as the most serious to be overcome to make this sensor a reality and the most susceptible of influencing the feasibility of this sensor. Aside from this issue, and given the extreme conditions under which the sensor must operate, the revised design is considered satisfactory from mechanical and thermal standpoints, since only minor modifications are required to make it fully compliant.

The per-unit cost for a small production run is about CAD $1400.00, which exceeds the targeted price. Machined parts alone represent more than 70% of that amount, without even taking into account the cost of the grids themselves or the assembly. Cost reductions are still possible in a number of areas. Coupler replacement, minimizing the use of gold-coated fibre, selection of cheaper source and detectors (w/o FO connectorization), better electronics component selection, and use of a single +5V supply for electronics, are all among the cost-reduction opportunities to explore.

The lens geometry and lens attachment components still represent a significant contributor to the overall design cost. Further, the machining costs are, to a large extent, driven by the high tolerances required. A thorough mechanical redesign exercise could therefore lead to significant cost savings.

Even more significant cost reductions could be achieved by eliminating the differential approach altogether, as the fibre, lens and detector costs could be halved. Mechanically and electronically, the design would also become simpler and more compact. On the other hand, this simplification implies that the compensation scheme for externally induced optical losses is abandoned. A low-cost internal compensation scheme could nonetheless be devised to compensate solely for source intensity variation.

The above simplification could more realistically be achieved in light of a reduction of the expected sensor resolution and accuracy. This would contribute to further reduce the costs and technical problems associated with machining and alignment tolerances.

REFERENCES

RD1 Gautier, C*., A Modulating Grid Optical Pressure Sensor*, Transportation Development Centre, Montreal, 2000.

RD2 *Optical Sensor Evaluation*, Public Works and Government Services Canada, contract T8200-01-0546.

RD3 Young, M., *Optics and Lasers*, 5th Edition, Springer, Berlin, 2000, ISBN 3-540-65741-X.

APPENDIX A

LightPipes Addon Matlab Code

```
% Propagation of collimated light beam through two identical gratings,
% one of which moves with respect to the other
% André Morin 2001-02-09
% version 3-5 : added support for multi wavelength
% version 6: improved total energy computation over version 5
%(adding intensities after conversion of field rather than
% adding fields and then computing total intensity
% version 7 is an incremental improvement over version 6 about
% intensity computation. The CircCAperture is now applied before
% OriginalEnergy is computed
% version 10-12 an increasingly streamlined structured
% version 13: 2001-03-03 by AM: added automated scan of InterGrating distance,
z1 and Dv
clear all;

%************** DEFINES' EQUATES AND PARAMETERS INITIALIZATION
****************
% Units definition
m  = 1;
cm = 0.01*m;
mm = 0.001*m;
um = 1e-6*m;
nm = 1e-9*m;

% Normalization types & misc types
NormBitmapStyle = 2;
NormNoNormStyle = 0;
NormNormStyle   = 1;
YES = 1;
NO = 0;

% State Variables
PlotRequired = NO;
FirstTime = YES;

% Define Variables
% Depending on beam propagation method selected
% must be careful to define field size much greater than aperture
% as per LightPipes warnings
% Equate for real-world dimensioning of beams and fields
OrigFOV         = 2000*um;
Ng              = 1280;       % size of grid

GlassThickness = 1*mm;

% Parameters to apply aperture of output of fibre or of Grin Lens
Ri  = 750*um;   % Initial lens aperture::Warning: this is RADIUS, NOT DIAMETER
Rf  = 750*um;  % exit lens aperture
xs  = 0*um;
ys  = 0*um;

% Parameters for fixed grating; assuming square size
Hf = 2000*um;   % full width
Af = 100*um;    % Grating slits height
```

```
% Derive number of slits

% This is the displacement due to diaphragm
Dv = 0*um;      % displacement Dv

% Moving grating
Hm = 2000*um;
Am = 100*um;    % Grating slits height
% Derive number of slits


% Wavelength distribution of light source:
% assume a uniform distribution for now
LambdaSamples   = 1;
LambdaRange     = 64*nm;
LambdaCenter    = 800*nm
k               = [1:LambdaSamples];
DeltaLambda     = (LambdaRange/LambdaSamples)
Lambda(k)       = LambdaCenter - (LambdaRange/2) - (DeltaLambda/2) +
(k*DeltaLambda);   % Wavelength vector

% Intensity array init
%Intensity       = 0.0 * ones(Ng);


%************** MAIN PROCESSING ***************
F2 = LPBegin(OrigFOV, Lambda(1), Ng);

Field = LPCircAperture(Ri,xs,ys,F2);

Nsf = fix(Hf/(2*Af));
% Deriving Dyf (spacing between centre of slits), assuming 50% duty cycle
% the last term -(1*um) is required to make everything symmetrical: REASON
UNKNOWN
Dyf = (-1*(Nsf-1)*Af)-(1*um)

% **********insert here code for glass window
%Field = LPSteps(GlassThickness, GlassThickness/(25*um), ones(Ng,
Ng)*complex(1.5, 1e-9), Field);  % use 40 steps over 1 mm : every 25 microns)

F1 = LPRectAperture(Hf, Af, 0, Dyf, 0, Field);
for(i = 1:Nsf-1)
    F2 = LPRectAperture(Hf, Af, 0, Dyf+(2*Af*i), 0, Field);
    F1 = LPBeamMix(F2, F1);
end;
%AfterFirstGratingCellField = F1;
clear F2;
clear Field;

AvailableEnergy = sum(sum(LPIntensity(NormNoNormStyle, F1)));
'done first grating'
InterGratingDistance = 200*um;
BeforeSecondGratingCellField = LPFresnel(InterGratingDistance, F1);
'done intergrating'
```

```
z1 = 700*um;
z2 = 700*um;
FirstTime = YES;
for(Dv = 0*um:3.125*um:100*um)
    % no of slits in moving grid
    Nsm = fix(Hm/(2*Am));

    % Derive dy (spacing between centres of slits): assume 50% duty cycle
    Dym = (-1*(Nsm-1)*Am)+Dv-(1*um)

      % Moving grating; must be larger in as it must still fill up all FOV
while moving

    F1 = LPRectAperture(Hm, Am, 0, Dym, 0, BeforeSecondGratingCellField);
    for(i = 1:Nsm-1)
        F2 = LPRectAperture(Hm, Am, 0, Dym+(2*Am*i), 0, BeforeSecondGrating-
CellField);
        F1 = LPBeamMix(F2, F1);
    end;
    clear F2;
    'done second grating'

    % **********Insert here code for glass window n = 1.5
    %GlassIndex = ones(Ng, Ng) * complex(1.5, 1e-9);
    %F1 = LPSteps(GlassThickness, GlassThickness/(25*um), ones(Ng,
Ng)*complex(1.5, 1e-9), F1);  % use 25 microns steps
    %F1 = LPSteps(z2, z2/(25*um), ones(Ng, Ng)*complex(1.0, 1e-9), F1);  % use
25 microns steps
    %clear GlassIndex;
    NLayerGlass = complex(1.5, 1e-9);
    DLayerGlass = [25*um];
    NLayerAir = complex(1, 1e-9);
    DLayerAir = [25*um];
    %for(xx = 0:1:40)    % 1 mm by steps of 25 um
    %    F1 = LPSteps(25*um, 1, ones(Ng,Ng)*NLayerGlass, F1);
    %end

      % Propagate field over distance to receiver (fibre or lens)
    %Field = LPFresnel(z1, F1);
    %F1 = LPSteps(z2, z2/(25*um), ones(Ng, Ng)*NLayerAir, F1);
    %for(xx = 0:1:z2/(25*um))    % 1 mm by steps of 25 um
    %    F1 = LPSteps(25*um, 1, ones(Ng,Ng)*NLayerAir, F1);
    %end
    for(w=0:1:(1000*um)/(25*um))
        z1 = (25*um*w)
        F1 = LPSteps(25*um, 1, ones(Ng, Ng)*NLayerAir, F1);
        %F1 = LPFresnel(200*um, F1);

        'done final propagation'
        Field = F1;
        FinalEnergy = sum(sum(LPIntensity(NormNoNormStyle, Field)));

        % and now the final aperture (fibre or lens aperture)
        Field = LPCircAperture(Rf,xs,ys,F1);
        'done final aperture'
```

```
        FinalEnergy10 = sum(sum(LPIntensity(NormNoNormStyle, Field)));

        Field = LPCircAperture(Rf*1.1,xs,ys,F1);
        FinalEnergy11 = sum(sum(LPIntensity(NormNoNormStyle, Field)));

        Field = LPCircAperture(Rf*1.2,xs,ys,F1);
        FinalEnergy12 = sum(sum(LPIntensity(NormNoNormStyle, Field)));

            % Compute ratio to original intensity
            EnrgyRatio = FinalEnergy/AvailableEnergy;
            EnrgyRatio10 = FinalEnergy10/AvailableEnergy;
            EnrgyRatio11 = FinalEnergy11/AvailableEnergy;
            EnrgyRatio12 = FinalEnergy12/AvailableEnergy;
        'done energy ratio'
        % Ratio of incoming energy to useable energy
            %Display ratio of slits
            SlitRatio = Dv/Af;

        if(FirstTime == YES)
            fid = fopen('c:\\test.csv','a');
            fprintf(fid, 'Slit Ratio,InterGrating,z1 [mm],Enrgy Ratio,Enrgy
Ratio10,Enrgy Ratio11,Enrgy Ratio12\n');
            FirstTime = NO;
            fclose(fid);
        end;
        fopen('c:\\test.csv','a');
        fprintf(fid, '%1.8f,%2.8f,%2.8f,%1.8f,%1.8f,%1.8f,%1.8f\n', SlitRatio,
InterGratingDistance*1000, z1*1000, EnrgyRatio, EnrgyRatio10, EnrgyRatio11,
EnrgyRatio12);
        fclose(fid);
    end
end;
```

APPENDIX B

Detailed Drawings

Drawing 1: Sensor head
Drawing 2: Sensor base
Drawing 3: Emitter lens cap
Drawing 4: Ferrule holder
Drawing 5: Half sphere
Drawing 6: Modulator grid
Drawing 7: Optical base
Drawing 8: Receiver lens cap
Drawing 9: Reference grid
Drawing 10: Sealing washer
Drawing 11: Sensor assembly
Drawing 12: Sensor assembly (exploded view)

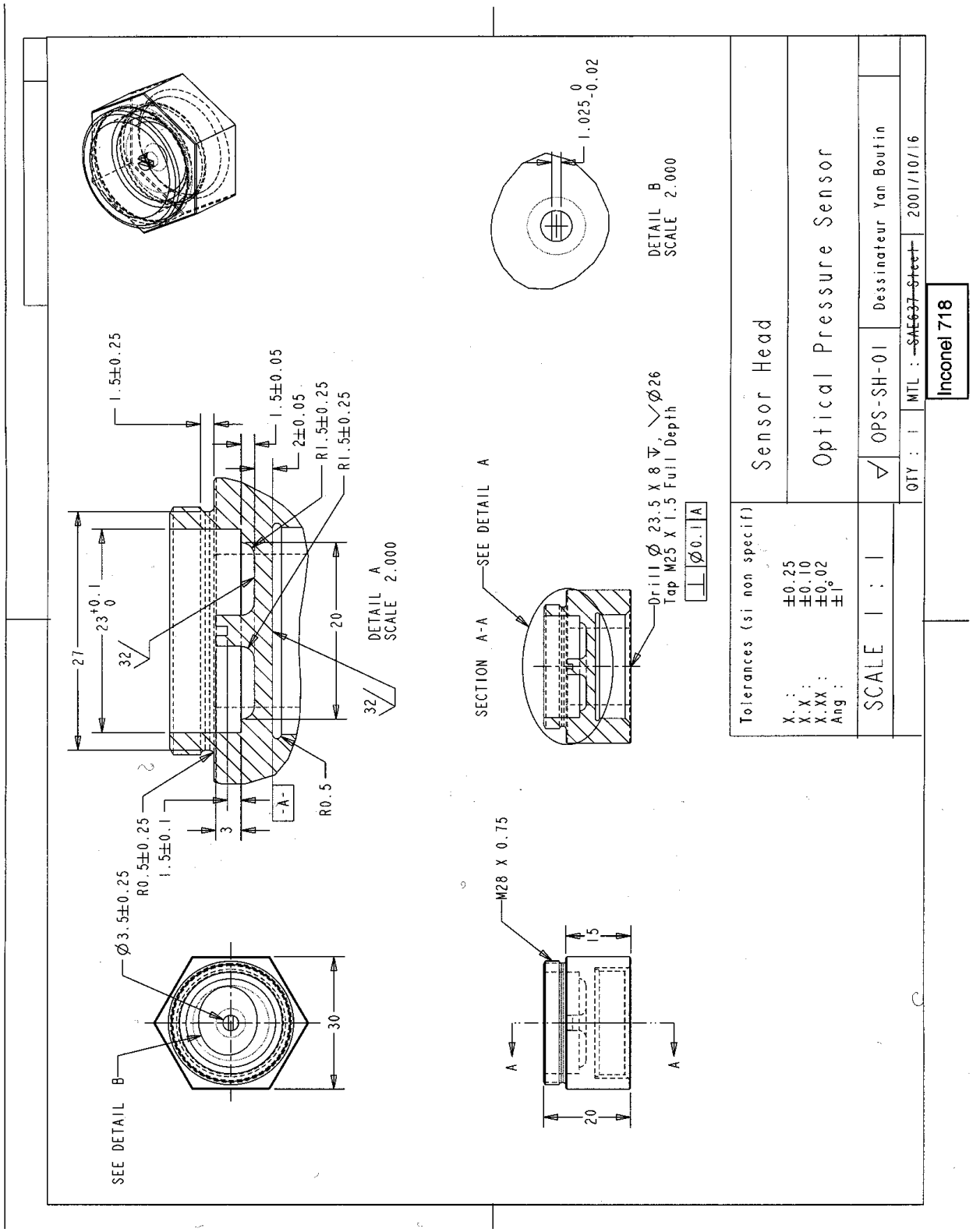
Sensor Head
Optical Pressure Sensor
OPS-SH-01
Dessinateur Yan Boutin
2001/10/16
MTL : SAE637 Steel
Inconel 718
SCALE 1 : 1
Tolerances (si non specif)
X. : ±0.25
X.X : ±0.10
X.XX : ±0.02
Ang : ±1°
DETAIL A SCALE 2.000
DETAIL B SCALE 2.000
SECTION A-A
SEE DETAIL A
SEE DETAIL B
Drill Ø 23.5 X 8 ↧, ⌵Ø26
Tap M25 X 1.5 Full Depth
M28 X 0.75

Sensor Head

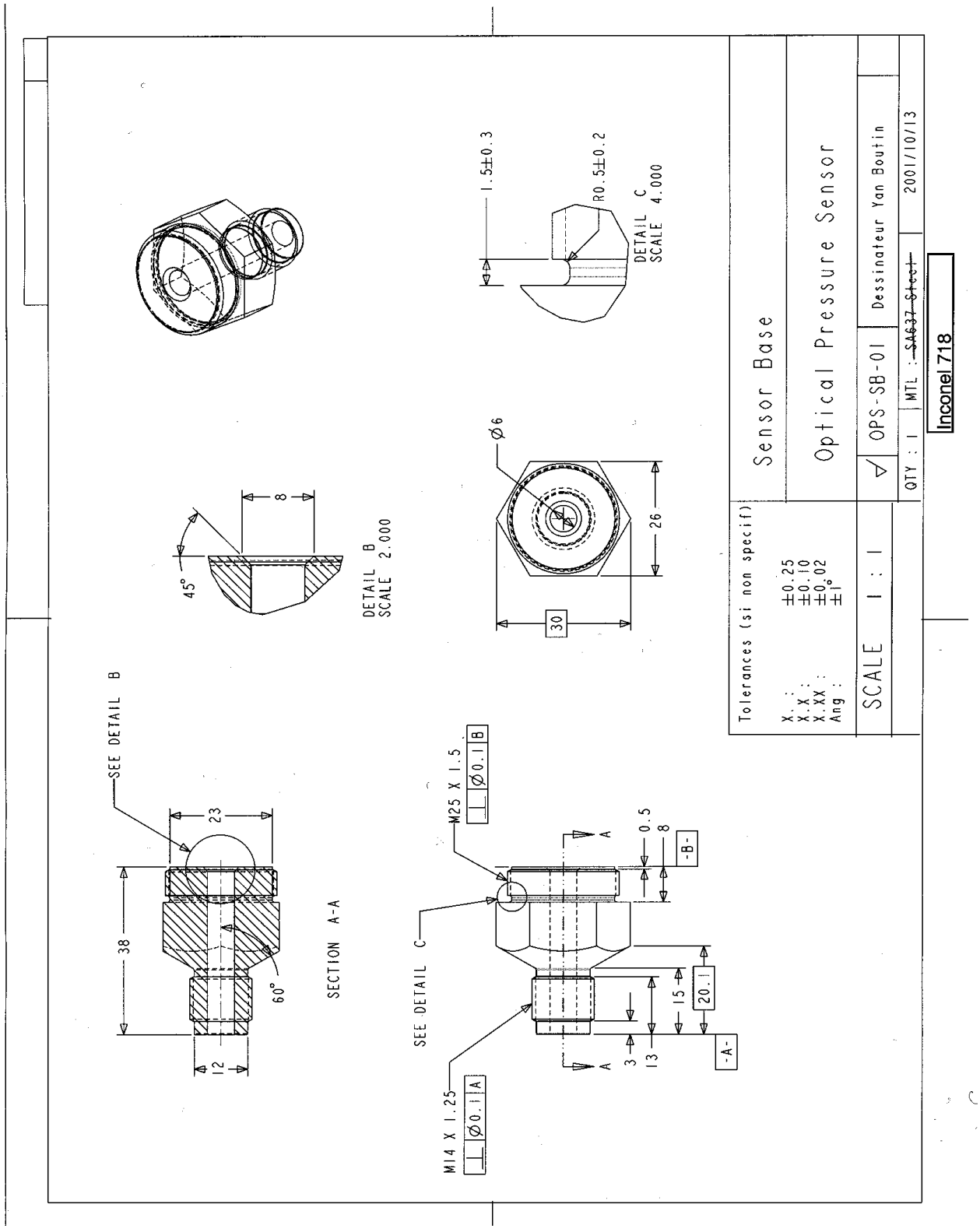
Sensor Base
Optical Pressure Sensor
OPS-SB-01
Dessinateur Yan Boutin
2001/10/13
QTY : 1
MTL : SAE37 Steel
Inconel 718
Tolerances (si non specif)
X . . : ±0.25
X.X : ±0.10
X.XX : ±0.02
Ang : ±1°
SCALE 1 : 1
DETAIL C
SCALE 4.000
1.5±0.3
R0.5±0.2
DETAIL B
SCALE 2.000
8
45°
Ø6
26
30
SEE DETAIL B
23
38
12
60°
SECTION A-A
M25 X 1.5
⊥ Ø0.1 B
SEE DETAIL C
M14 X 1.25
⊥ Ø0.1 A
0.5
8
-B-
15
20.1
-A-
3
13

Sensor Base

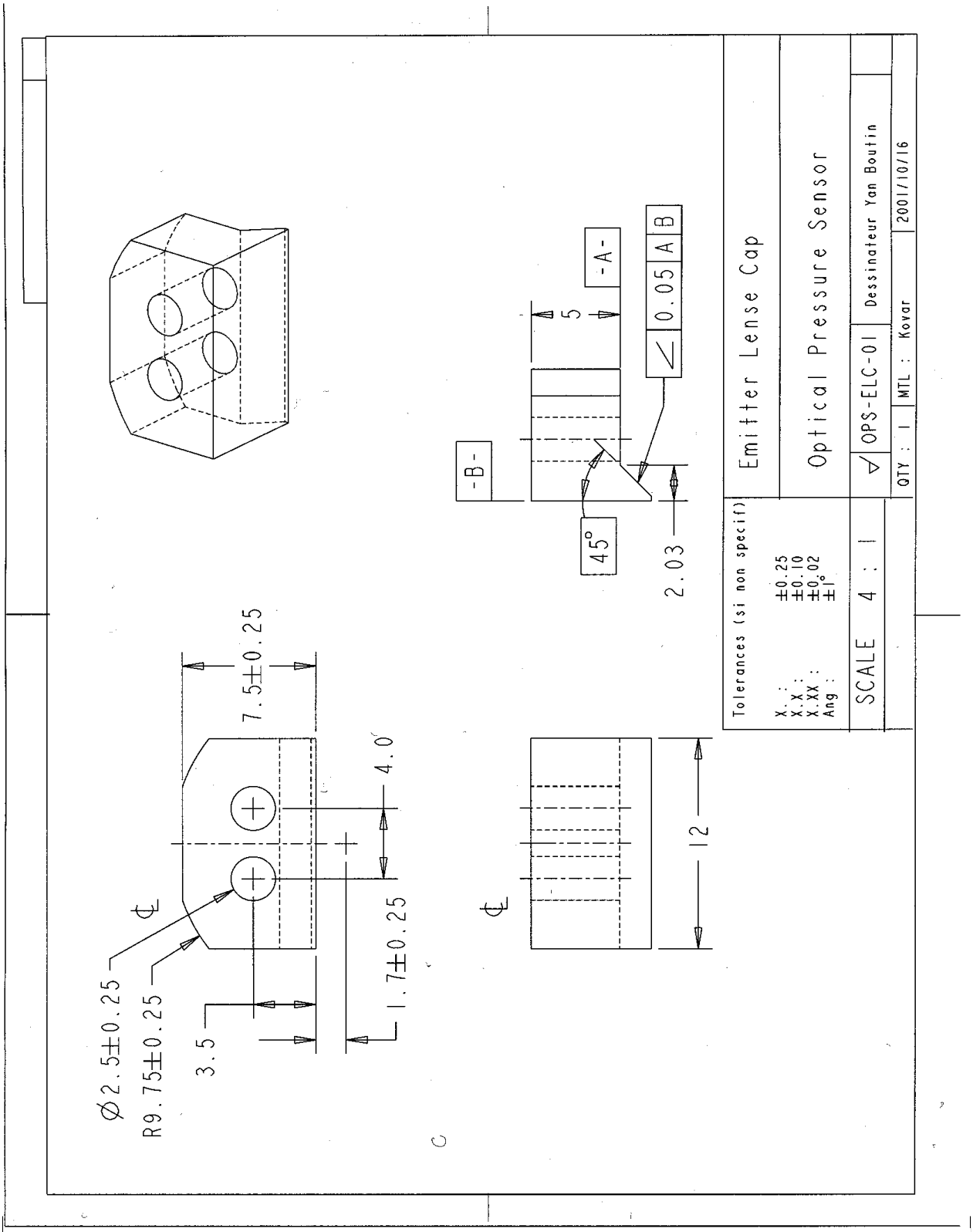

Figure 34

Emitter Lens Cap

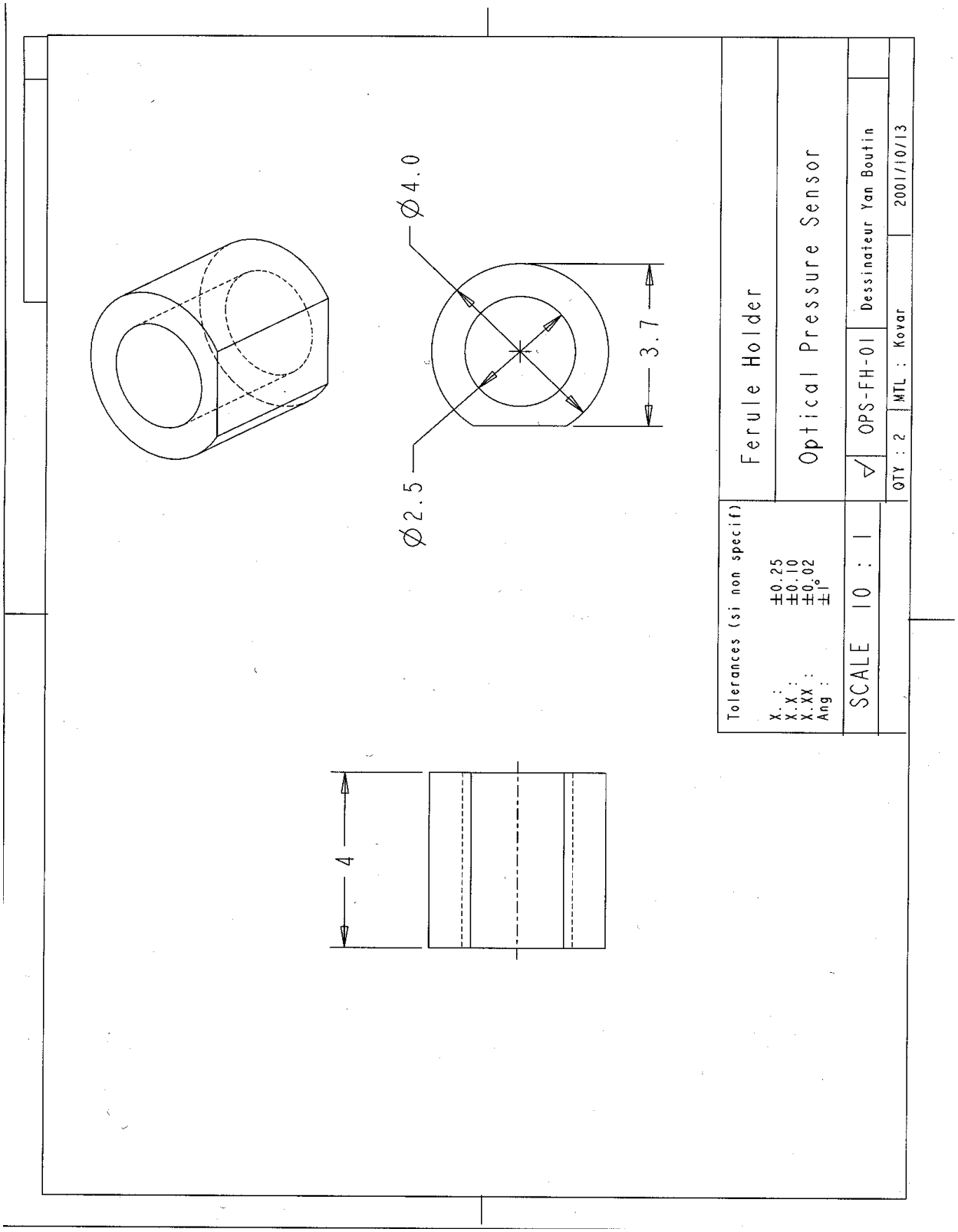

Ferrule Holder

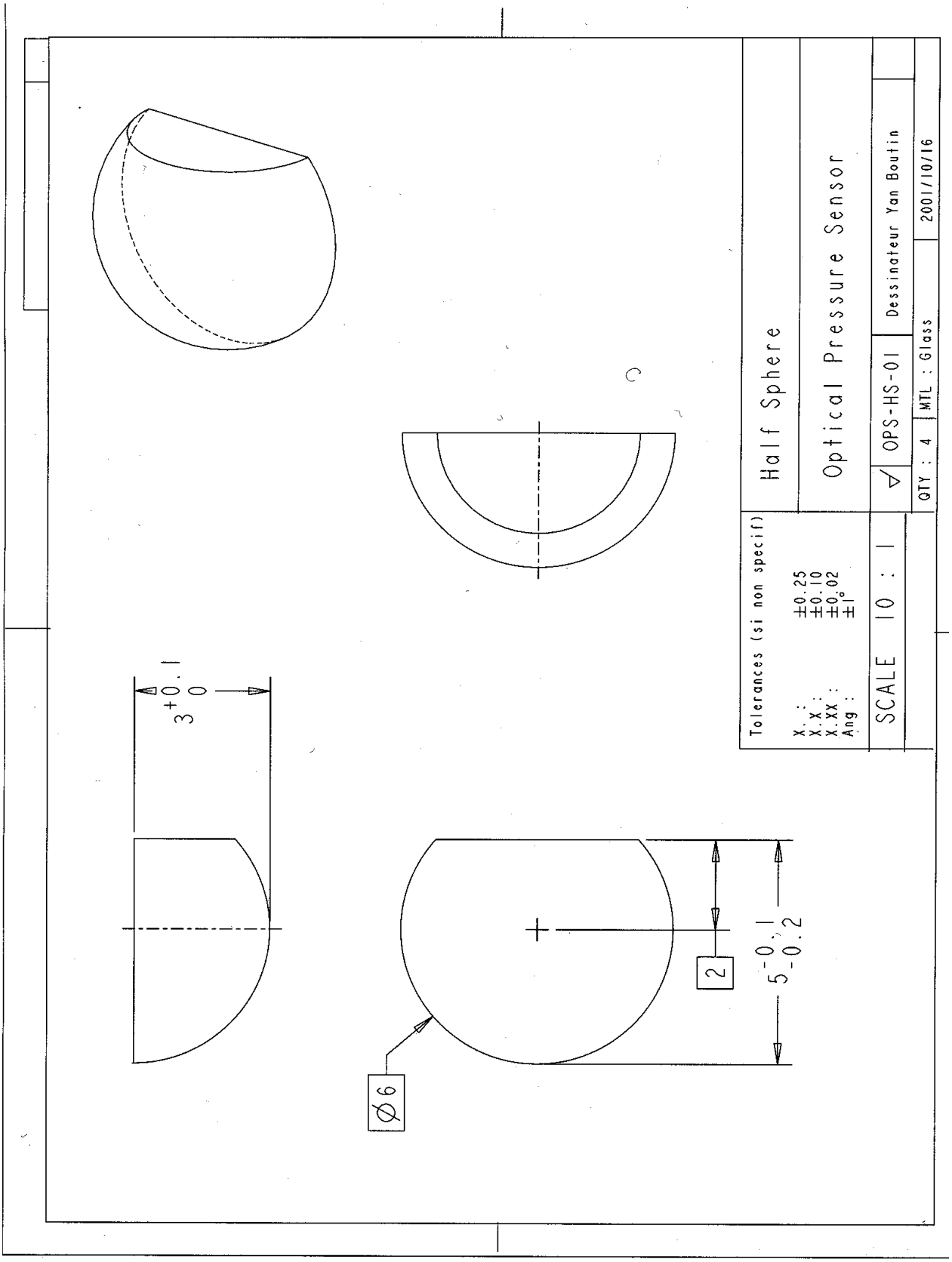

Half-Sphere (Lens)

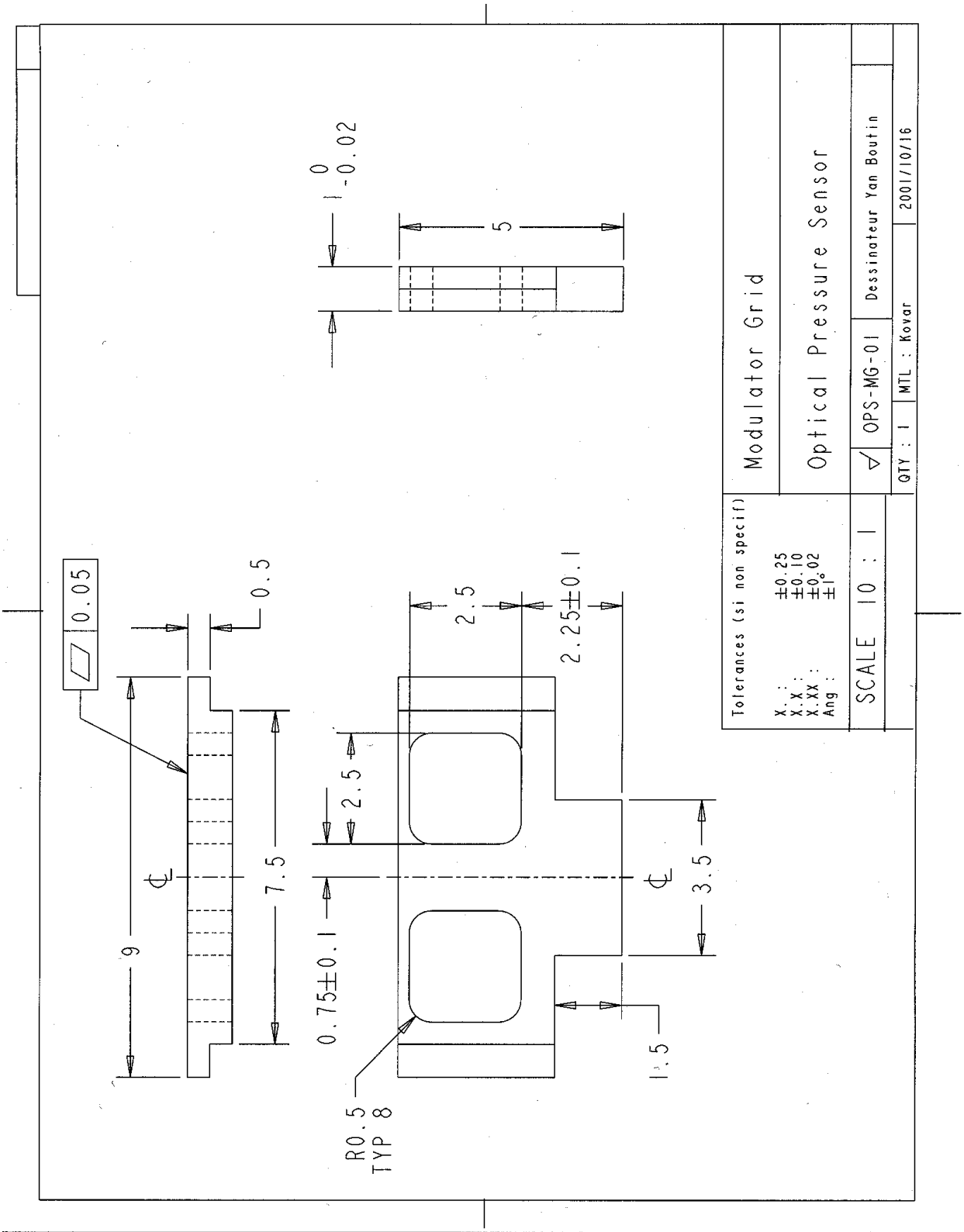

Modulating Grid

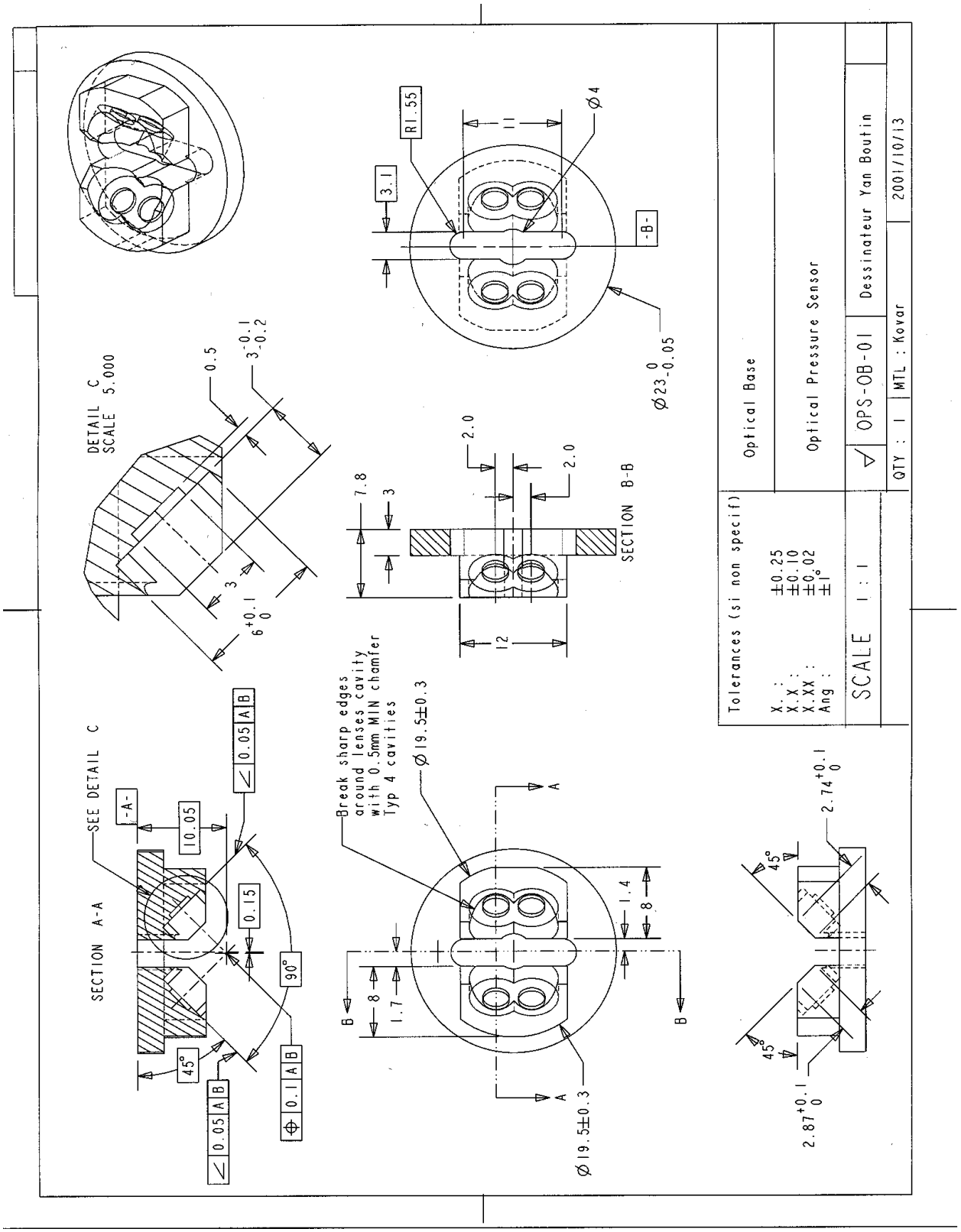

Optical Base

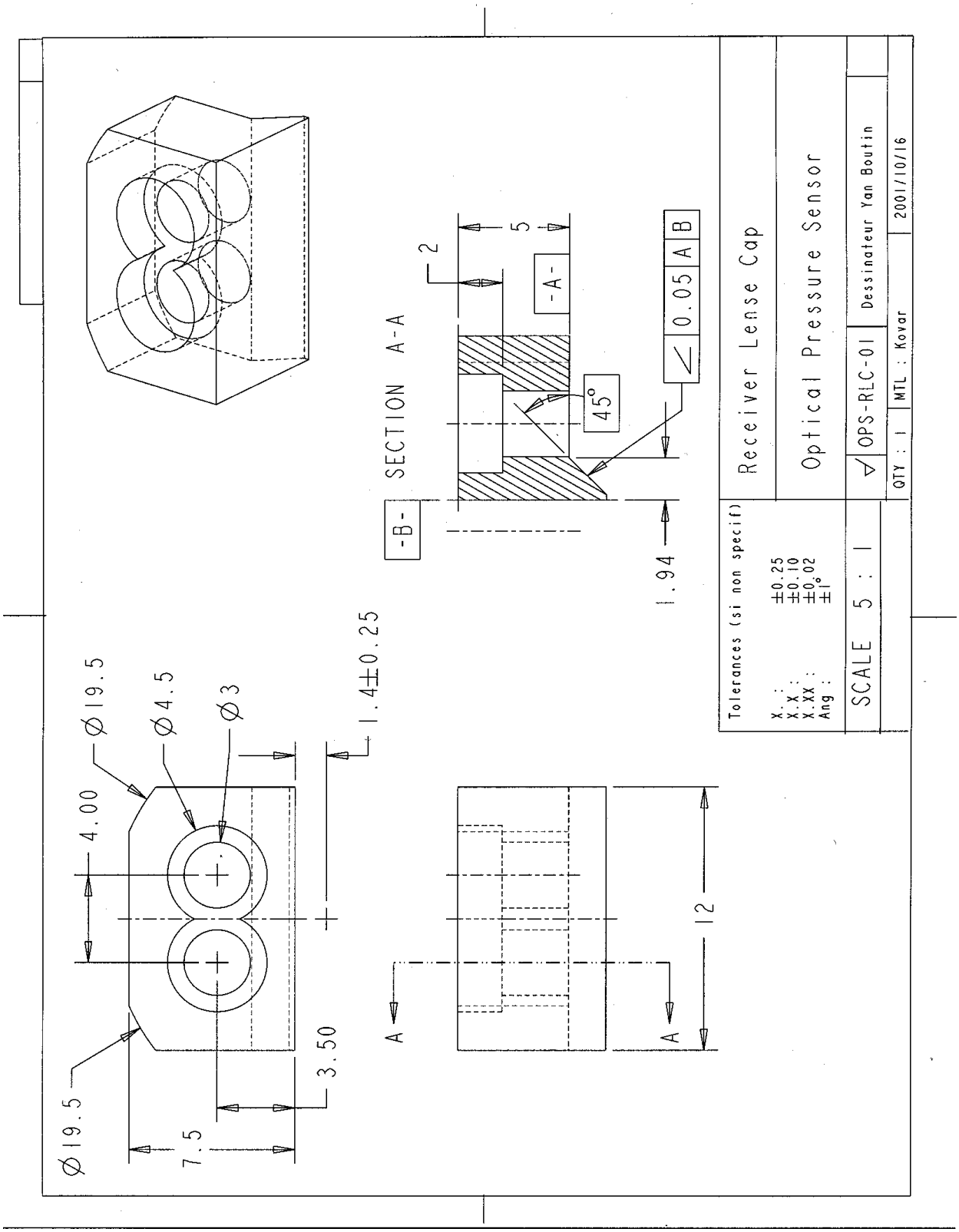

Receiver Lens Cap

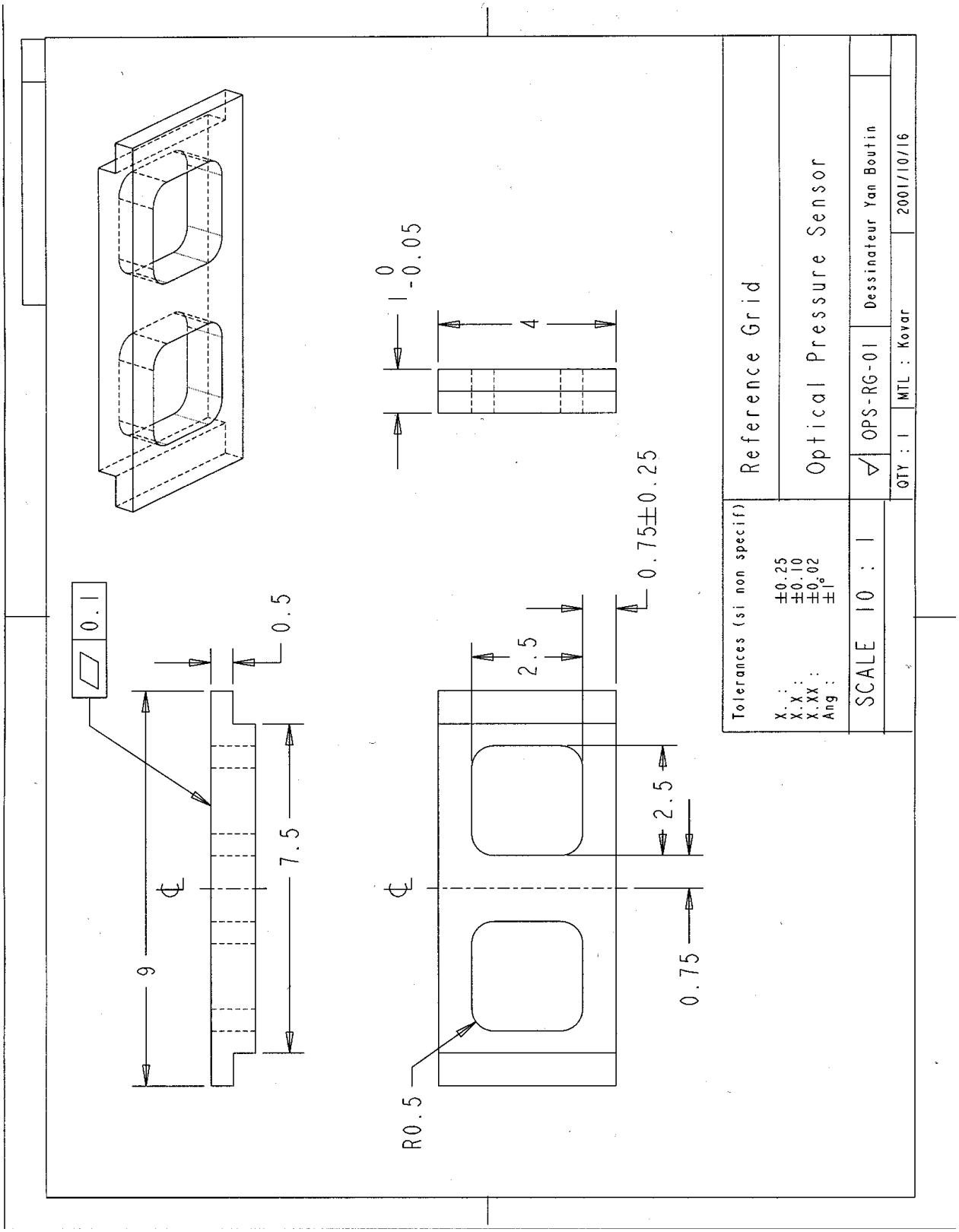

Reference Grid

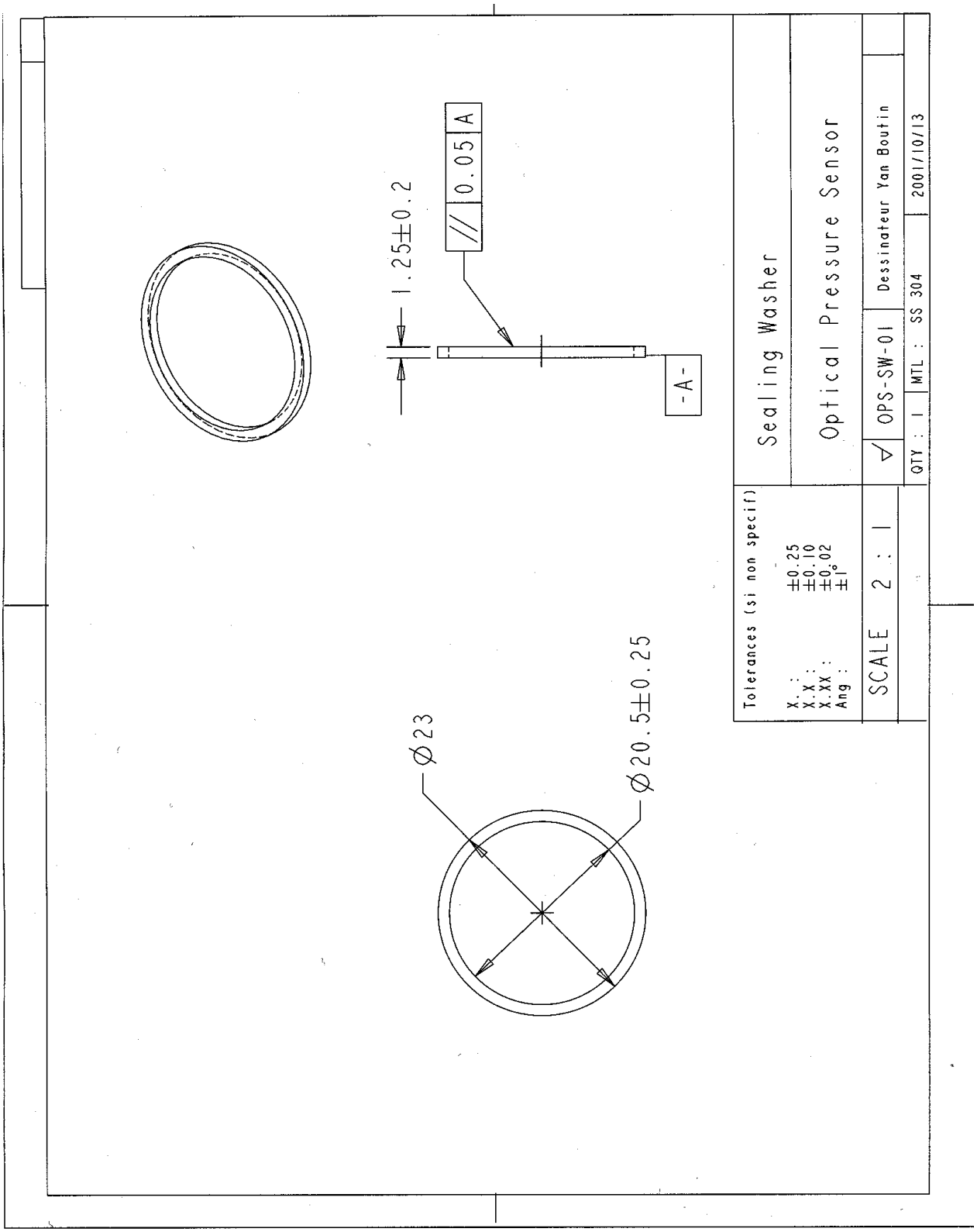

Sealing Washer

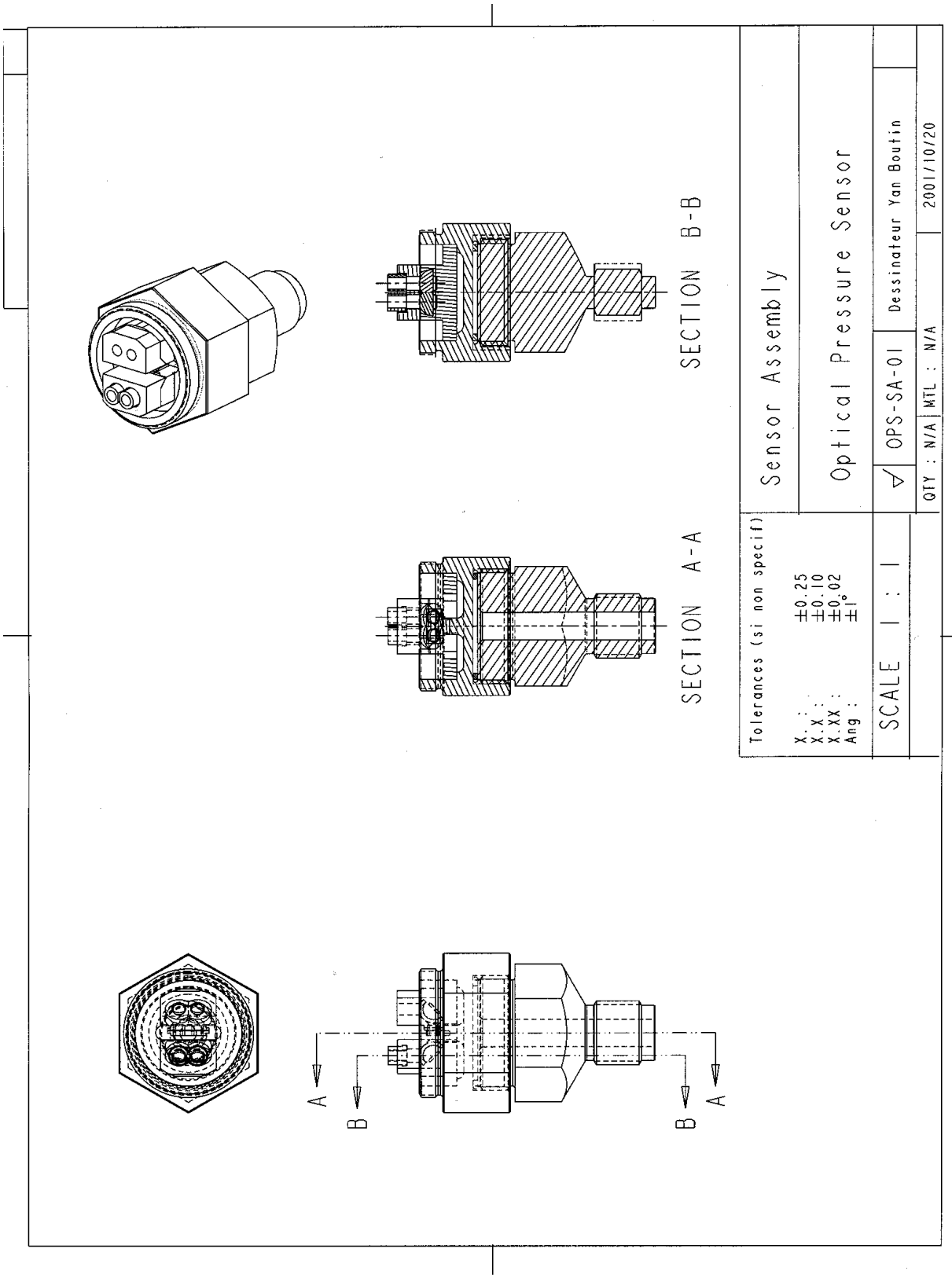

Sensor Assembly

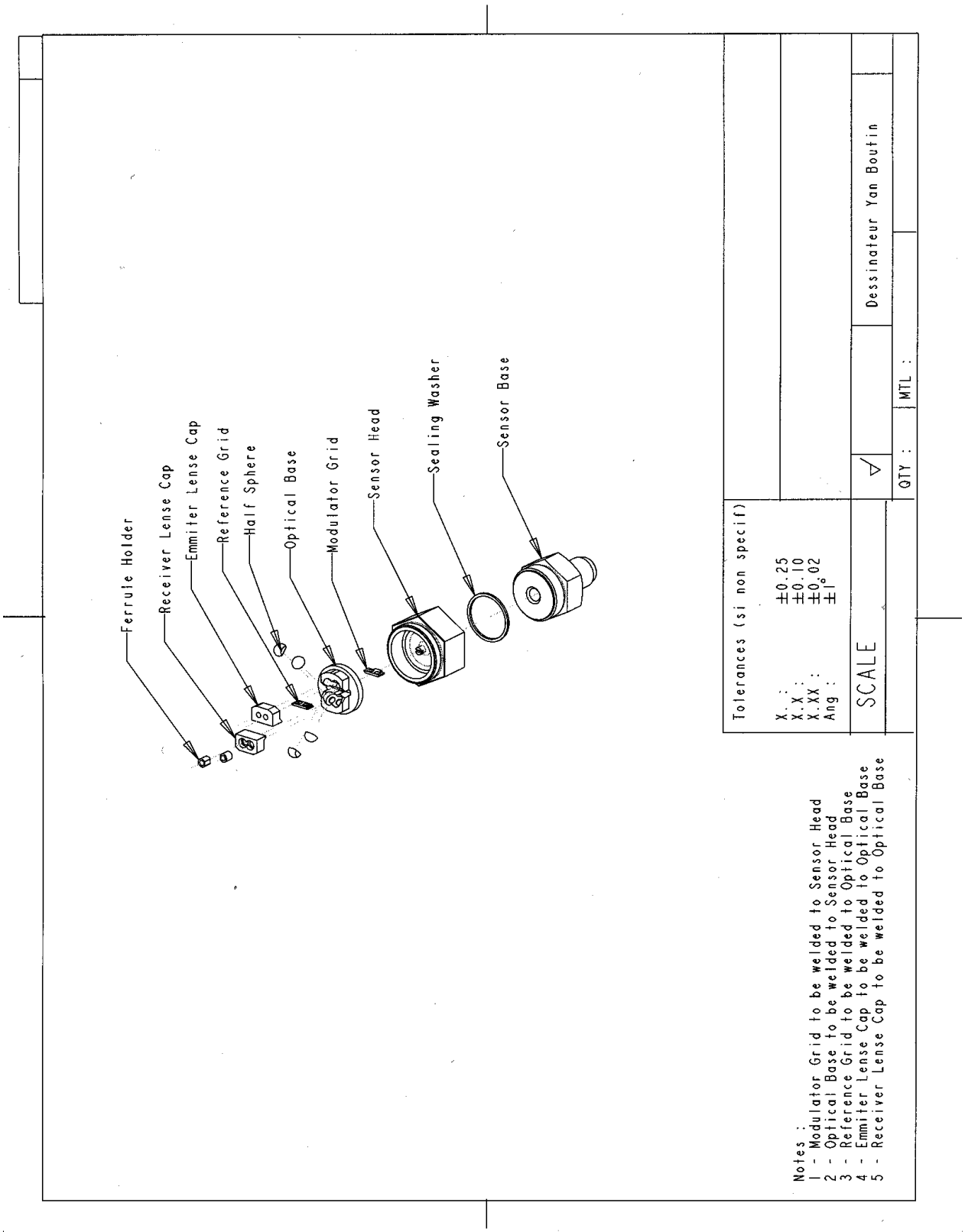

Figure 35 **Sensor Assembly**

APPENDIX C

Quotations

12/06/2001 10:58 4504494228 USI SCIF DEMO INC PAGE 01

31, chemin du Tremblay, local 101
BOUCHERVILLE (Québec)
J4B 7L6

Téléphone : (450) 449-4945
Télécopieur : (450) 449-4228

E-mail : usinage@e-scape.net

Date : 6 décembre 2001

Destinataire : **M. J.F. Chatelain**

N° de télécopieur : (514) 396-8530

Expéditeur : M. Carol Morissette

Nombre de page incluant celle-ci : 3

OBJET : Soumission

Tel que demandé ___X___ Donner suite _____

Pour votre information _____ Tel que convenu _____

Original suivra par la poste _____ Pour vos commentaires _____

COMMENTAIRES :

Si vous n'avez pas reçu toutes les pages, veuillez nous rappeler aussitôt que possible au numéro mentionné ci-haut.

2001 10:58 4504494228 USI SCIF DEMO INC PAGE 02

P. 1/2

USINAGE SCIENTIFIQUE DEMO inc.

31, chemin du Tremblay, local 101
BOUCHERVILLE (Québec) J4B 7L6

Téléphone : (450) 449-4945
Télécopieur : (450) 449-4228

E-mail : usinage@c-scape.net

Soumission

Numéro de soumission :	02249
Date de soumission:	6 décembre 2001
Date de livraison :	1 février 2002
Notre numéro de référence :	DM-3520
Votre numéro de référence :	

Client : M. J.-F. Chatelain

École de Technologie Supérieure (Université du Québe
1100, rue Notre-Dame Ouest
Montréal (Québec) H3C 1K3

Article	Description	Quantité	Prix unitaire	Montant
	Usinage et assemblage de 1 et 20 prototypes de OPICAL PRESSURE SENSOR, selon Dessins suivants :			
01	OPS-ELC-01 en Kovar	1	674.70 $	674.70
		20	52.84 $	1,056.80
02	OPS-FH-01 en Kovar	1	532.57 $	532.57
		20	53.37 $	1,067.40
03	OPS-MG-01 en Kovar	1	932.62 $	932.62
		20	129.55 $	2,591.00
04	OPS-OB-01 en Kovar	1	997.60 $	997.60
		20	168.61 $	3,372.20
05	OPS-RLC-01 en Kovar	1	718.94 $	718.94
		20	130.94 $	2,618.80
	F.O.B. Notre Usine, Expédier via votre camion			

T.P.S. et/ou T.V.Q. en sus Terme : net 30 jours **TOTAL**

Cette soumission est basée sur les détails fournis sur les plans, soit les quantités et le matériel requis. Toutes modifications des plans pourront entrainer une modification des prix. Notre entreprise s'engage à respecter la confidentialité des travaux exécutés par nos employés. Une clause de confidentialité et de non-concurrence est prévue dans les contrats d'embauche de nos employés et ceux-ci pourrons être poursuivi en justice dans l'éventualité de non respect de ce contrat.

Cette soumission n'est valide que pour une période de 45 jours

Signature : Carol Morin

2001 10:58 4504494228 USI SCIF DEMO INC PAGE 03

P. 2/2

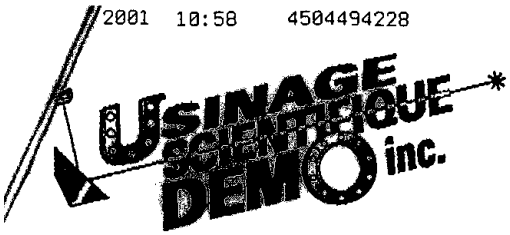

Soumission

31, chemin du Tremblay, local 101
BOUCHERVILLE (Québec) J4B 7L6

Téléphone : (450) 449-4945
Télécopieur : (450) 449-4228

E-mail : usinage@e-scape.net

Numéro de soumission :	02249
Date de soumission:	6 décembre 2001
Date de livraison :	1 février 2002
Notre numéro de référence :	DM-3520
Votre numéro de référence :	

Client M. J.-F. Chatelain

École de Technologie Supérieure (Université du Québe
1100, rue Notre-Dame Ouest
Montréal (Québec) H3C 1K3

Article	Description	Quantité	Prix unitaire	Montant
06	OPS-RG-01 en Kovar	1	932.62 $	932.62
		20	136.37 $	2,727.40
07	OPS-SW-01 en SS304	1	182.87 $	182.87
		20	17.17 $	343.40
08	OPS-SH-01 en Inconel 718	1	922.52 $	922.52
		20	155.90 $	3,118.00
09	OPS-SB-01 en Inconel 718	1	1,208.78 $	1,208.78
		20	185.92 $	3,718.40
Note	- Ces prix incluent le Kovar, l'Inconel 718 et l'Assemblage par soudure par fusion au (T.I.G.). - Nous serons en mesure de vous fournir un prix pour 2000 unités assemblées, que lorsque nous aurons exécuté les 20 prototypes. - Une avance de fond de 10% soit $ 2000.00 seras requis pour couvrir l'achat des matériaux Kovar et Inconel 718. F.O.B. Notre Usine, Expédier via votre camion			

T.P.S. et/ou T.V.Q. en sus Terme : net 30 jours TOTAL

Cette soumission est basée sur les détails fournis sur les plans, soit les quantités et le matériel requis. Toutes modifications des plans pourront entrainer une modification des prix. Notre entreprise s'engage à respectar la confidentialité des travaux exécutés pur nos employés. Une clause de confidentialité et de non-concurrence est prévue dans les contrats d'embauche de nos employés et ceux-ci pourrons être poursuivi en justice dans l'éventualité de non respect de ce contrat.

Cette soumission n'est valide que pour une période de 45 jours

Signature : Carol Morin

APPENDIX D

Initial Tightening Force

This appendix presents the detailed calculations used to size the sensor's bolt assembly. As per the figure, the dimensions are *Ri* = 10.25 mm and *N* = 1.25 mm. Hence, the effective gasket contact width is *b* = *N/2* = 0.625 mm. The internal pressure is P = 20 MPa. Assuming a stainless steel gasket, the seating yield stress *Y* = 180 MPa. According to ASME, the sealing factor *m* is 6.5.

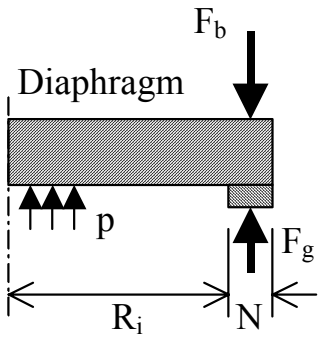

The required seating bolt load is given by

$$F_{b0} \geq 2\pi(R_i + b) \cdot b \cdot Y = 8690 \text{ N} \tag{D.1}$$

The required sealing bolt load F_s is given by

$$F_g \geq 2\pi(Ri + b) \cdot (b \cdot m \cdot P) \tag{D.2}$$

Hence,

$$F_{bS} > 2\pi(R_i + b)(b \cdot m \cdot P) + (\pi R_i^2 \cdot P) = 12\ 150 \text{ N} \tag{D.3}$$

Thus, F_{bolt} must be larger than the greater of the above bolt load values 12 150 N. For an additional safety factor, we choose F_{bolt} = 20 000 to 25 000 N. This value gives a safety factor of 1.6 to 2.0 that should cover the upset pressures.

The required tightening torque is calculated with

$$\begin{aligned} T &= 0.2 \times 2(R_i + N) \\ &= 93 \text{ to } 120 \text{ N} \cdot \text{m} \end{aligned} \tag{D.4}$$

APPENDIX E

Film Coefficient Calculations

The volume of gas in contact with the walls of the sensor is as follows:

r_1 = 3.00 mm ;
r_2 = 0.25 mm ;
Y_1 = 18.00 mm ;
Y_2 = 1.25 mm

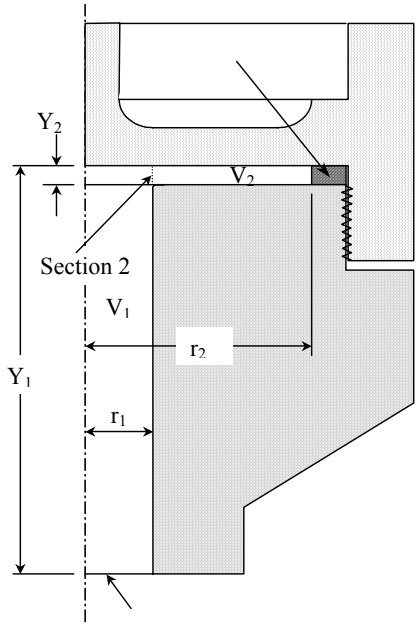

The gas within the enclosure is treated as air at 723 K (450°C) and the following properties are used:

Gas constant R = 287 N-m/kg-K
Specific heat C_p = 1010 N-m/kg-K,
Absolute viscosity μ = 33×10^{-6} N-s/m^2,
Thermal conductivity k = 0.05 N/s-K
Prandtl number P_r = 0.72

The volume of gas in the cavity enclosed by the sensor is

$$V_1 = \pi(r_2^2 - r_1^2)Y_2 = 377\text{mm}^3$$
$$V_2 = V_1 + \pi R_1^2 Y_1 = 810.73\text{mm}^3 \quad \text{(E.1)}$$

The mass of gas in these volumes at pressure P = 15 MPa and T = 723 K (450°C) is given by

$$m_i = P \cdot V_i / R \cdot T \quad \text{(E.2)}$$

with m_1 = 58.6 mg and m_2 = 21.82 mg. With a ratio of pressure of about 150, almost 99.3% of the gas mass flows out of sections 1 and 2 when the pressure drops to atmospheric (0.1 MPa).

We now compute the average gas mass velocity across sections 1 and 2. Since the compression time for a 4-cycle engine is ¼ of the engine cycle, we obtain a compression time of 36 milliseconds for 7-cycles/second engine.

The cross-section areas for sections 1 and 2 are A_1 = 28.27 mm^2 and A_2 = 18.85 mm^2. Using

$$G_i = M_i / (\Delta t \cdot A_i), \quad \text{(E.3)}$$

we obtain G_1 = 57.59 kg-m^2-s^{-1} and G_2 = 20. kg-m^2-s^{-1}.

The hydraulic diameters are defined as the outside diameter less the inner diameter. Treating section 2 as an annulus with a gap Y_2, we therefore have $D_{h1} = 2r_1$ and $D_{h2} = 2Y_2$.

We now calculate the gas flow Reynolds numbers at sections 1 and 2. We know that

$$R_{Ei} = D_i G_i / \mu \tag{E.4}$$

We obtain RE_1 = 10 470 and RE_2 = 1234. Hence the flow is turbulent in region 1 and laminar in region 2 since the flow is considered turbulent when RE > 2300.

Finally, we compute the film coefficients at sections 1 and 2, conservatively assuming that the above conditions apply continuously over time.

For turbulent and laminar flows in tubes, the coefficient h is respectively given by

$$\begin{aligned} h &= (k / D_h) \cdot (0.023\,\mathrm{R_e}^{0.8} \cdot \mathrm{P_r}^{0.33}) \\ h &= (k / D_h) \cdot (1.86\,\mathrm{R_e}^{0.33} \cdot \mathrm{P_r}^{0.33}) \cdot (D_h / L)^{0.33} \end{aligned} \tag{E.5}$$

When applied, to sections 1 and 2, equation E.5 gives

h_1 = 282.8 W/m^2-ºC and
h_2 = 285.7 W/m^2-ºC

APPENDIX F

LED and Detectors Datasheets

Product Bulletin OPF342
August 1996

Fiber Optic GaAlAs High Speed LED in ST* Receptacle
Types OPF342A, OPF342B, OPF342C, OPF342D

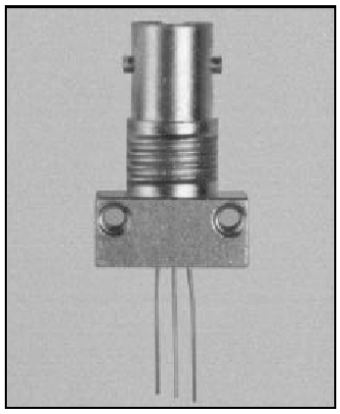

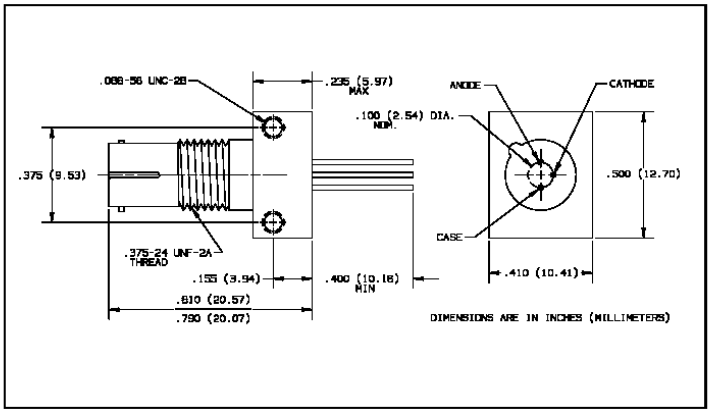

Features

- Component pre-mounted and ready to use
- Pre-tested with fiber to assure performance
- Popular ST* style receptacle
- High Speed
- Electrically isolated from case

Description

The OPF342 series LED consists of a hermetic LED, pre-mounted and aligned in an ST* receptacle. This configuration is designed for PC board or panel mounting. Includes lock washer and jam nut, two 2-56 screws, and a dust cap.

The LED's are designed to interface with multimode optical fibers from 50/125 to 200/300 microns.

*ST is a registered trademark of AT&T.

Absolute Maximum Ratings (T_A = 25° C unless otherwise noted)

Reverse Voltage . . . . . 1.0 V
Continuous Forward Current . . . . . 100 mA(4)
Storage Temperature Range . . . . . -55° C to +150° C
Operating Temperature Range . . . . . -40° C to +125° C
Lead Soldering Temperature [1/16 inch (1.6 mm) from case for 5 sec. with soldering iron] . . . . . 240° C(1)

Notes:
(1) RMA flux is recommended. Duration can be extended to 10 sec. max when flow soldering.
(2) Graded index fiber, 50 µm core, N.A. = 0.20.
(3) To convert radiant power output to dBm, use the following expression dBm = 10 log (µW/1000).
(4) Derate linearly @ 1.0 mA/° C above 25° C.
(5) Prebias @ 5 mA current.

LED Burn-in

All LED's are subject to 100% burn-in testing. Test conditions are 96 hours at 100 mA continuous current in 25° C ambient.

TYPICAL COUPLED POWER into OPTICAL FIBER

Typical Coupled Power I_F = 100 mA @ 25° C						
Fiber	**Refractive Index**	**N.A.**	**OPF342D**	**OPF342C**	**OPF342B**	**OPF342A**
50/125 µm	Graded	0.20	7.5 µW	12.5 µW	18 µW	25 µW
62.5/125 µm	Graded	0.28	14 µW	22 µW	34 µW	45 µW
100/140 µm	Graded	0.29	38 µW	62 µW	95 µW	125 µW
200/300 µm*	Step	0.41	140 µW	235 µW	340 µW	475 µW

*PCS - Plastic Clad Silica

Types OPF342A, OPF342B, OPF342C, OPF342D

Electrical Characteristics (T_A = 25° C unless otherwise noted)

SYMBOL	PARAMETER		MIN	TYP	MAX	UNITS	TEST CONDITIONS
P_O	Radiant Power Output	OPF342D OPF342C OPF342B OPF342A	5.0 10.0 15.0 20.0	7.5 12.5 18.0 25.0		µW	I_F = 100 mA(2)
V_F	Forward Voltage			1.8	2.0	V	I_F = 100 mA
λp	Peak Output Wavelength		830	850	870	nm	I_F = 50 mA
B	Spectral Bandwidth Between Half Power Points			35		nm	I_F = 50 mA
t_r	Output Rise Time			4.5	6.0	ns	I_F = 100 mA, 10%-90%(5)
t_f	Output Fall Time			4.5	6.0	ns	I_F = 100 mA, 90%-10%(5)

Typical Performance Curves

Relative Coupled Power vs. Forward Current

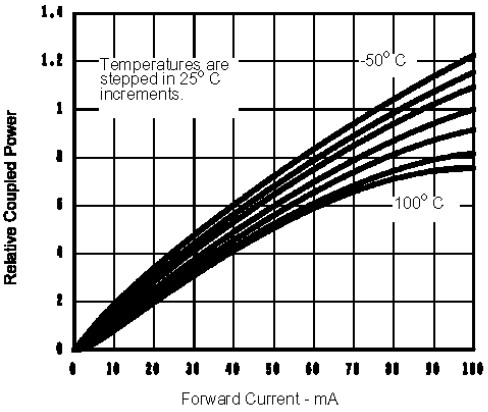

Forward Voltage vs. Forward Current

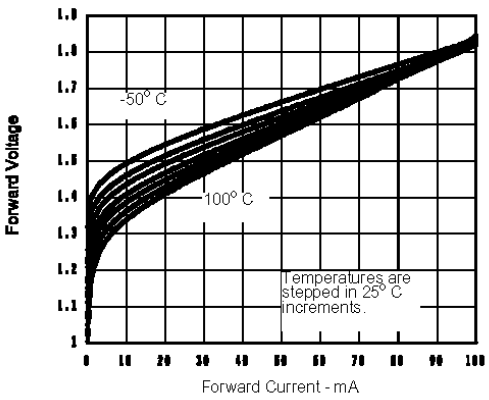

FIBER OPTIC COMPONENTS

OPTEK

Product Bulletin OPF472
August 1996

Fiber Optic PIN Photodiode in ST* Receptacle Type OPF472

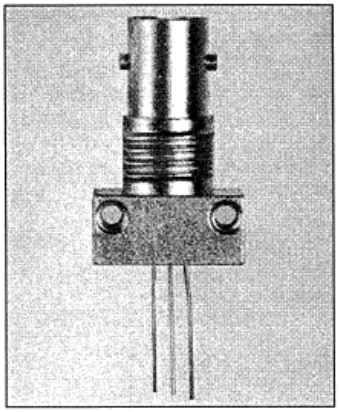

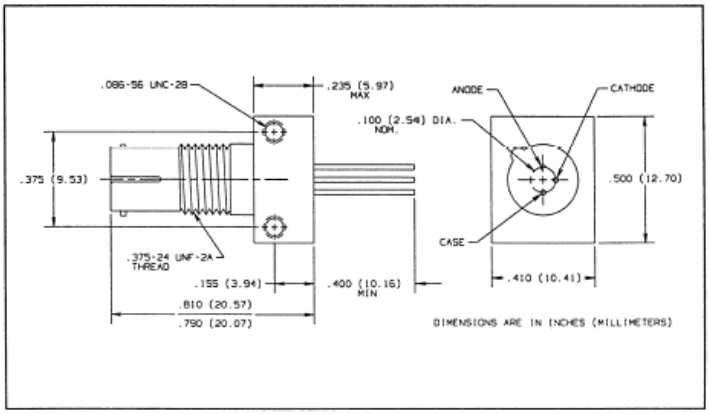

Features

- Component pre-mounted and ready to use
- Pre-tested with fiber to assure performance
- Popular ST style receptacle

Description

The OPF472 consists of a low cost plastic cap PIN photodiode pre-mounted and aligned in an ST receptacle. This configuration is designed for PC board or panel mounting. Includes lock washer and jam nut, two 2-56 screws, and dust cap.

The PIN Photodiodes are designed to interface with multimode optical fibers from 50/125 to 200/300 microns.

*ST is a registered tardemark of AT&T.

Absolute Maximum Ratings (T_A = 25° C unless otherwise noted)

Reverse Voltage	100 VDC
Continuous Power Dissipation	200 mW(1)
Storage Temperature Range	-55° C to +100° C
Operating Temperature Range	-40° C to +85° C
Lead Soldering Temperature [1/16 inch (1.6 mm) from case for 5 sec. with soldering iron]	240° C(2)

Notes:
(1) Derate linearly @ 2.0 mW/° C above 25° C.
(2) RMA flux is recommended. Duration can be extended to 10 sec. max when flow soldering.
(3) Test @ V_R = 5 V with 50/125 micron, 0.20 N.A. fiber, @ 10 µm optical power @ 850 nm. Responsivity levels apply to 50 µm, 62.5 µm and 100 µm core optical fibers.
(4) R_L = 50 Ω, 10% -90%.

Typical Performance Curves

Relative Spectral Response

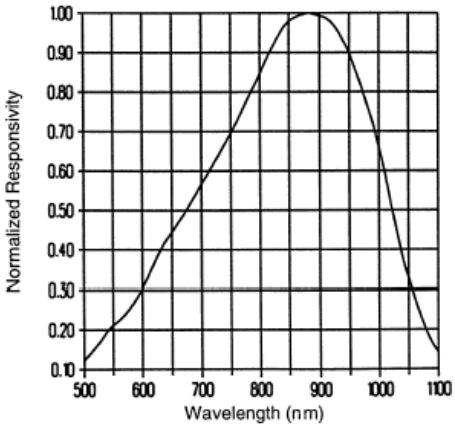

Optek Technology, Inc. 1215 W. Crosby Road Carrollton, Texas 75006 (972) 323-2200 Fax (972) 323-2396

Type OPF472

Electrical Characteristics (T_A = 25° C unless outherwise noted)

SYMBOL	PARAMETER	MIN	TYP	MAX	UNITS	TEST CONDITIONS
R	Flux Responsivity	0.45	0.55		A/W	V_R = 5.0 V(3)
I_D	Dark Current		0.1	5.0	nA	V_R = 5.0 V
λp	Peak Response Wavelength		880		nm	
t_r	Output Rise Time		6.0		ns	V_R = 15 V(4)
C_T	Total Capacitance		3.0		pF	V_R = 20 V

TYPICAL PERFORMANCE CURVES

DARK CURRENT vs. AMBIENT TEMPERATURE

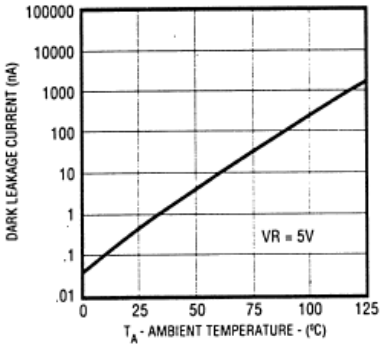

RISE TIME vs. REVERSE VOLTAGE

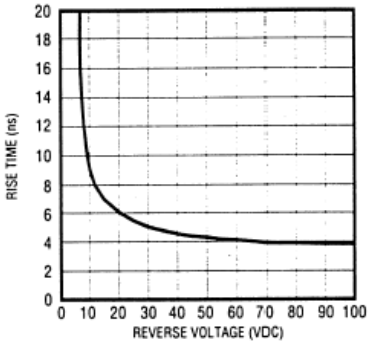

DARK CURRENT vs. REVERSE VOLTAGE

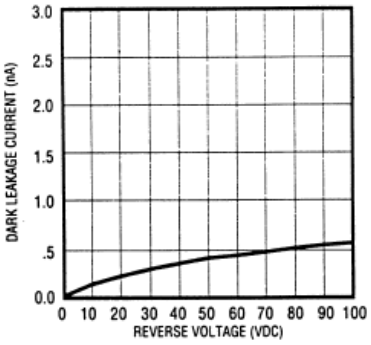

TYPICAL CAPACITANCE vs. REVERSE VOLTAGE

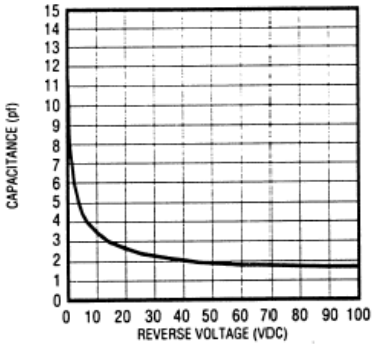

FIBER OPTIC COMPONENTS